UNIVERSITY OF SOUTHAMPTON

Faculty of Engineering and Physical Sciences
School of Physics and Astronomy

Utilising Long Term Radio Observations of Auroral Kilometric Radiation to Explore Magnetosphere-Ionosphere Coupling

by

James Edwin Waters

MPhys

ORCiD: 0000-0001-8164-5414

A thesis for the degree of
Doctor of Philosophy

December 2022

University of Southampton

Abstract

Faculty of Engineering and Physical Sciences
School of Physics and Astronomy

Doctor of Philosophy

Utilising Long Term Radio Observations of Auroral Kilometric Radiation to Explore Magnetosphere-Ionosphere Coupling

by James Edwin Waters

Auroral Kilometric Radiation (AKR) is Earth's most powerful, naturally-emitted radio emission. It is a direct result of the dynamics of energetic electrons along high latitude magnetic field lines in the magnetosphere-ionosphere coupling region, and is useful for inference of the spatial morphology and activation of the auroral acceleration region. In this thesis, a novel technique is developed to retrieve calibrated AKR observations from the Wind spacecraft, without the presence of solar and other contaminating radio emissions. Wind houses a remote-sensing radio observatory and has been active since 1995, providing the longest dataset of AKR from many viewing positions around the Earth. For AKR, which is anisotropically beamed, this breadth of data allows the effect of the observer position to be characterised. Subsequently, the data are used to explore AKR dynamics and corresponding changes in the auroral acceleration region during substorms and other disturbed periods. Firstly, the AKR selection is applied to a 30 day period during the Earth flyby of the Cassini spacecraft for a multipoint observation. Comparing the temporal modulation of the AKR power from both spacecraft during this period, it is shown that a diurnal modulation is likely due to the geometrical effect of the rotating magnetic dipole, but also sees intrinsic source modulation common to both hemispheres. Secondly, the selection is applied to 10 years of observations that overlap with published lists of substorm onsets. After accounting for viewing, the average AKR power in low and high frequency bands was examined during the substorm timeline. This demonstrated that higher altitude AKR sources provide a greater contribution during substorm onset on average, and that this relative contribution scales with the level of disturbance. Finally, dayside observations of AKR were used during the arrival of a coronal mass ejection (CME) at Earth. While showing that Wind's dayside observations can be used as a metric for magnetospheric activity, coincident observations of the UV aurora were used to constrain the auroral origin, namely intense, dayside auroral dynamics related to an ongoing substorm.

Contents

List of Figures

List of Tables

Declaration of Authorship

I declare that this thesis and the work presented in it is my own and has been generated by me as the result of my own original research.

I confirm that:

1. This work was done wholly or mainly while in candidature for a research degree at this University;
2. Where any part of this thesis has previously been submitted for a degree or any other qualification at this University or any other institution, this has been clearly stated;
3. Where I have consulted the published work of others, this is always clearly attributed;
4. Where I have quoted from the work of others, the source is always given. With the exception of such quotations, this thesis is entirely my own work;
5. I have acknowledged all main sources of help;
6. Where the thesis is based on work done by myself jointly with others, I have made clear exactly what was done by others and what I have contributed myself;
7. Parts of this work have been published as: J. E. Waters, C. M. Jackman, L. Lamy, B. Cecconi, D. K. Whiter, X. Bonnin, K. Issautier, and A. R. Fogg. Empirical Selection of Auroral Kilometric Radiation During a Multipoint Remote Observation With Wind and Cassini. *Journal of Geophysical Research: Space Physics*, 126(10), oct 2021a. ISSN 2169-9380. . URL https://onlinelibrary.wiley.com/doi/10.1029/2021JA029425
J E Waters, C M Jackman, D K Whiter, C Forsyth, A R Fogg, and L Lamy. A Perspective on Substorm Dynamics Using 10 Years of Auroral Kilometric Radiation Observations From Wind Journal of Geophysical Research : Space Physics. 2022.

Signed:..... Date:.....

Acknowledgements

I am eternally grateful to both my supervisors, Caitriona and Dan, who have been an unending source of motivation, encouragement, positivity and general support and understanding throughout this process. I couldn't have asked for better supervisors, who have given me incredibly useful insight to the requirements of science and academia from the mundane to the taxing and complex. I have no doubt that I would not have been able to complete this work were it not for your scientific expertise, as well as your patience and time spent listening to my oten inane questions. Particularly to Caitriona, I acknowledge the effort required to accommodate my, "somewhat" less organised, working style! Your aid in overcoming various technical and pastoral issues has certainly not been overlooked, and I will always be thankful to you both for this.

I would like to thank my collaborators, particularly Laurent, Baptiste and Xavier, for acclimatising me to the wonders of radio instrumentation, spending many hours guiding me through the challenges of utilisng the Wind AKR observations and helping me navigate the Meudon lunch queue etiquette.

Thanks to all of the Space Environment Physics group at Southampton for providing a wonderfully friendly office environment, plenty of inspiration and for paddleboard adventures when the Sun was out! Thanks also to the brilliant Magnetospheres group at DIAS for all your interesting science and for being so accommodating whenever I've visited Dublin.

I am completely grateful to my family, who have supplied endless love, support and reassurance of my capability to pursue and complete this work. I am incredibly lucky to have such encouraging, kind and caring parents, and cannot thank them enough for providing such an environment throughout my life.

Last, but not least, thanks to my friends both from home and those at Southampton, who have on countless occasions provided a welcome reprieve from the PhD headspace. This extends again to Dan, who normalised the idea of climbing outside on rocks for me, and to those in the Southampton University Mountaineering Club for helping me build this passion, without which the PhD would have been much more difficult.

Chapter 1

Introductory Space Plasma Physics

1.1 Introduction

The research in this thesis concerns radio emission from sources found along high latitude magnetic field lines in the auroral zone of Earth, using remote sensing observations made by the Wind/Waves instrument. The first chapter will present the fundamental space plasma physics on which this work relies, such as particle motion in magnetic and electric fields, the frozen in approximation and magnetic reconnection. Chapter 2 will apply these concepts to the terrestrial magnetosphere and its interaction with the solar plasma and magnetic field, discussing the dynamics and energy pathways of the system. Chapter 3 will describe the spacecraft and instrumentation used in this thesis. Chapters 4 to 6 present the scientific investigations that comprise the primary work of this thesis. These science chapters are presented in chronological order, following the publication date of the associated papers. Chapter 4 presents the details and first application of the data processing procedure developed to select the Auroral Kilometric Radiation (AKR). Chapter 5 demonstrates the use of this data selection in a statistical analysis with magnetospheric substorms, while chapter 6 sees it applied in a case study observation during the arrival of a coronal mass ejection at Earth. The thesis is then concluded in chapter 7 with a summary and a discussion of future scientific exploration that could arise.

1.2 Basic Plasma Definition

Plasma is one of the four fundamental states in which matter can exist in the universe. It is characterised by a hot, ionised gas of particles that can be considered as quasineutral in a bulk context, given equal numbers of positive and negative charge carriers from the components of dissociated atoms. The presence of charge carriers in a plasma dictates both their own behaviour and the behaviour of the plasma as a whole when under the effect of electric or magnetic fields; this motion and the subsequent effects are the subject of this chapter.

1.3 Maxwell's Equations

At distances greater than 100 km above the Earth's atmosphere, the matter must be considered as a plasma. As the Earth is a magnetised planet, at the very least the motion of the plasma and its constituents must also consider the effect of this magnetic field. Often, electric fields are also present. The equations that govern the variability of electric and magnetic fields in space and time, and therefore the fundamental behaviour of the plasma, are known as the Maxwell equations, and are given in the following (e.g. Baumjohann and Treumann, 2012).

$$\nabla \cdot \mathbf{E} = \frac{\rho}{\epsilon_0} \tag{1.1}$$

$$\nabla \cdot \mathbf{B} = 0 \tag{1.2}$$

$$\nabla \times \mathbf{E} = -\frac{\partial \mathbf{B}}{\partial t} \tag{1.3}$$

$$\nabla \times \mathbf{B} = \mu_0 \mathbf{j} + \epsilon_0 \mu_0 \frac{\partial \mathbf{E}}{\partial t} \tag{1.4}$$

Equations 1.1 and 1.2 describe the generation of electromagnetic fields. The first is Gauss' law, or the Poisson law of electrodynamics which relates the divergence of the electric field E through a closed surface that surrounds a charge density ρ. ϵ_0 is the permittivity of free space, a constant. This holds for both static charges and those in motion; these instances will generate an electric field. The second is a description of the fact that magnetic monopoles do not exist in nature, as the imposed null of the divergence of a magnetic field B suggests that such a field can only exist in closed loops and cannot support point sources.

The second two of Maxwell's equations (equations 1.3 and 1.4) describe the fundamental relationship between time-varying electric and magnetic fields and how they correspond to spatial variations in the opposite fields. Faraday's law (equation 1.3) describes both a theoretical and experimental postulation of the relationship, with

a changing magnetic field generating an electric field. The orientation of the induced electric field can be derived experimentally with Lenz's rule, and is described by the minus sign, and is inherently related to the change in magnetic field regardless of its rapidity. Equation 1.4 gives the Ampere-Maxwell law. μ_0 describes another constant, the permeability of free space, and in this case dictates the magnitude of the current induced by the magnetic field, described by j. The latter term on the right hand side of equation 1.4 describes the displacement current; given that the factor $\mu_0\epsilon_0 = 1/c^2 \ll 1$, any fluctuations in the electric field must be rapid for there to be a significant contribution. This is rarely the case when considering electromagnetism in space plasmas so is often ignored, reducing the fourth Maxwell equation to Ampere's law:

$$\nabla \times \mathbf{B} = \mu_0 \mathbf{j} \tag{1.5}$$

1.4 Kinetic Plasma Motion in Magnetic and Electric Fields

The phenomena studied in this thesis are fundamentally related to the bulk motion of plasma in the near-Earth space environment. The temporal and spatial variation of the plasma can be described in multiple ways including a kinetic approach, where the behaviour of individual particles is considered, and a fluid approach, where the behaviour of the collective plasma is considered. As the constituent particles of the plasma are charged, they can couple with electric and magnetic fields and are thus governed by their spatial and temporal variation. The primary equation of motion of a charged particle in the presence of both electric and magnetic fields is given by the following:

$$m\frac{d\boldsymbol{v}}{dt} = q(\boldsymbol{E} + \boldsymbol{v} \times \boldsymbol{B}) \tag{1.6}$$

where m, $\boldsymbol{v}$ and $\boldsymbol{q}$ are the mass, velocity, and charge of the particle respectively, and $\boldsymbol{E}$ and $\boldsymbol{B}$ are the external electric and magnetic fields. The right hand side of equation 1.6 is given by the sum of the Coulomb force ($q\boldsymbol{E}$) and the Lorentz force ($q\boldsymbol{v} \times \boldsymbol{B}$). This equation of motion can be used to derive the behaviour of charged particles in a range of electromagnetic fields and subsequently the global patterns of plasma motion about the Earth on a variety of scales.

1.4.1 Gyromotion in a Non-Zero, Static Magnetic Field

In this section, the motion of a single charged particle under the influence of a uniform, static magnetic field is examined. Without an external electric field, equation 1.6 reads:

$$m\frac{dv}{dt} = qv \times \boldsymbol{B} \tag{1.7}$$

In this case, it can be shown that the magnitude of the velocity, and thus the kinetic energy of the particle, is unchanged in the presence of such a magnetic field. This is true regardless of the spatial extent of the field which, in the dipolar-like geomagnetic field of Earth, results in a predictable motion of the particle along a given field line (Baumjohann and Treumann, 2012). This motion, and the subsequent consequences for the trajectory of the particle, are explored here.

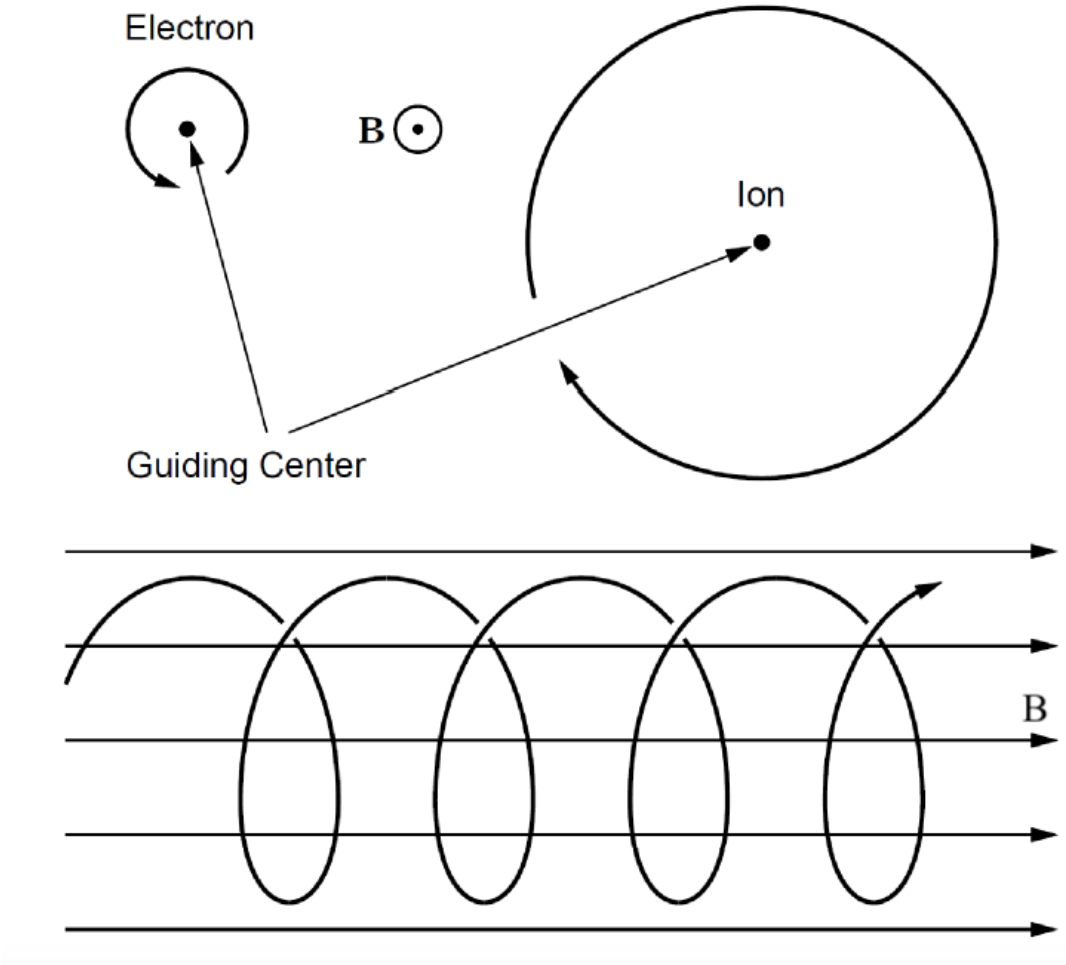

FIGURE 1.1: Schematic illustration of the helical motion of electrons and ions about a static magnetic field B. Adapted from Baumjohann and Treumann (2012).

Equation 1.7 can be manipulated to show that charged particles follow harmonic motion in a plane transverse to the magnetic field B, and as such the particle velocity describes circular motion about the field with a characteristic gyrofrequency Ω and gyroradius r_g given by

$$\Omega = \frac{qB}{m} \tag{1.8}$$

$$r_g = \frac{v_\perp}{|\Omega|} = \frac{v_\perp m}{|q|B} \tag{1.9}$$

where q and m are as previously defined. $v_\perp = \sqrt{v_x^2 + v_y^2}$ is the constant speed of the particle in the plane transverse to the magnetic field. Equation 1.8 is dependent on the sign of the charge of the particle and thus the sense of rotation about the field is opposite for negatively charged electrons and positively charged ions. This sense of rotation and the motion of the particle itself generates a magnetic field, a so-called diamagnetic field, that opposes the external magnetic field. The gyrofrequency presented in equation 1.8 shows that electrons will circle the magnetic field at a higher rotation frequency than ions, which are much heavier in even the simplest cases. Following from this, equation 1.9 shows that ions will also traverse a much larger gyroradius. In most cases, there will be a non-zero component of the velocity in a direction parallel to the magnetic field, and thus the charged particle will follow a three-dimensional helical motion along the magnetic field. This helical trajectory is shown schematically in figure 1.1; the field line about which the charged particle gyrates and its direction is known as the guiding center of the particle trajectory.

The combination of the transverse ($v_\perp$) and parallel ($v_\parallel$) velocities in the helical particle motion can be conveniently defined by the pitch angle:

$$\alpha = \tan^{-1} \frac{v_\perp}{v_\parallel} \tag{1.10}$$

which can also be thought of as the angle between the velocity vector of the particle and the magnetic field, and has consequences for not only fundamental particle motion in a magnetic field, but also the contribution of particle energy to the magnetosphere-ionosphere coupling region and the generation of Auroral Kilometric Radiation (AKR), as explored in sections 2.6 and 2.7.

1.4.2 Magnetic Mirroring

It is unreasonable to assume that the magnetic fields that a particle traverses in the space plasma environment are completely uniform and static. The approximations in earlier sections that consider this circumstance are sufficient enough to describe the basic motion, but towards the poles of the Earth the magnetic field lines converge and become much stronger, which has an influence on the particle motion. Although there are components of the particle energy that are both parallel and perpendicular to the

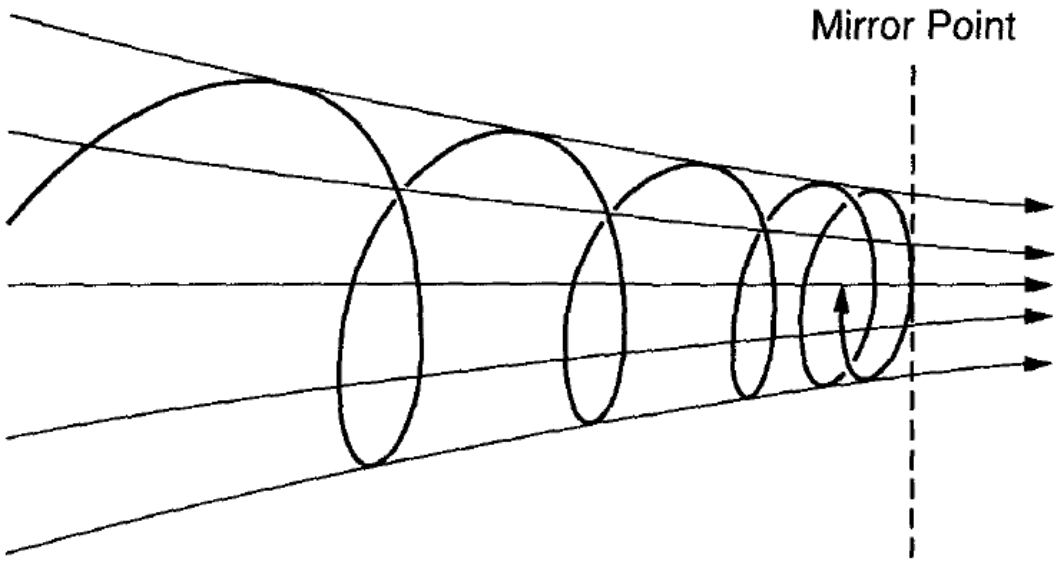

FIGURE 1.2: Schematic figure of a charged particle trajectory as it enters a region of converging magnetic field, with the pitch angle increasing as it reaches the mirror point and is reflected. From Baumjohann and Treumann (2012).

magnetic field, the total energy of the particle is conserved when under no influence from external forces. In cases where the scale of the particle gyration and motion about the field is most significant the magnetic moment is conserved. While not an absolute constant in all cases, under temporal plasma variations with frequencies less than that of the gyromotion it can be approximated as such; the magnetic moment is the first of a set of quantities known as the adiabatic invariants are seen in the following equation 1.11:

$$\mu_m = \frac{m v_\perp^2}{2B} \tag{1.11}$$

where m is the particle mass, $v_\perp$ is the component of the particle speed perpendicular to the magnetic field and B is the external magnetic field itself (Baumjohann and Treumann, 2012).

From its definition in equation 1.10, and considering conservation of kinetic energy, the pitch angle changes as the magnetic field strength increases or decreases. Equation 1.11 can be written in terms of the pitch angle α to give:

$$\mu_m = \frac{m v^2 \sin^2 \alpha}{2B} \tag{1.12}$$

A particular consequence of these combined unchanging quantities is that the pitch angle increases with increasing field strength, and the speed of the particle in the direction of the guiding centre will decrease as the motion of the particle changes in

lieu of the above conservation laws. If the pitch angle of the particle is completely perpendicular to the magnetic field, it cannot penetrate any further and is reflected at what is known as the mirror point. This is shown schematically in Figure 1.2. At this point, the pitch angle is 90°, and so a particle with pitch angle α in a position where the magnetic field has a static value B will mirror at the position where the magnetic field strength is:

$$B_m = \frac{B}{\sin^2 \alpha} \tag{1.13}$$

Equation 1.13 implies that particles with a smaller, more field-aligned pitch angle will require a higher magnetic field strength in order for them to mirror and reflect. In the terrestrial magnetosphere, as discussed in detail in chapter 2, the magnetic field is dipolar and so converges symmetrically in nature in both polar regions of the Northern and Southern hemispheres. Thus the typical value for a reference magnetic field strength in Equation 1.13 is that at the equator, B_{eq}, where the field strength is a minimum, and the corresponding equatorial pitch angle α_{eq}. In many cases, a particle may continuously mirror between the maximum magnetic field at the two poles and become trapped. This forms the second of the adiabatic invariants that corresponds to such a bounce motion and is known as the longitudinal invariant; this is not described in detail here, however.

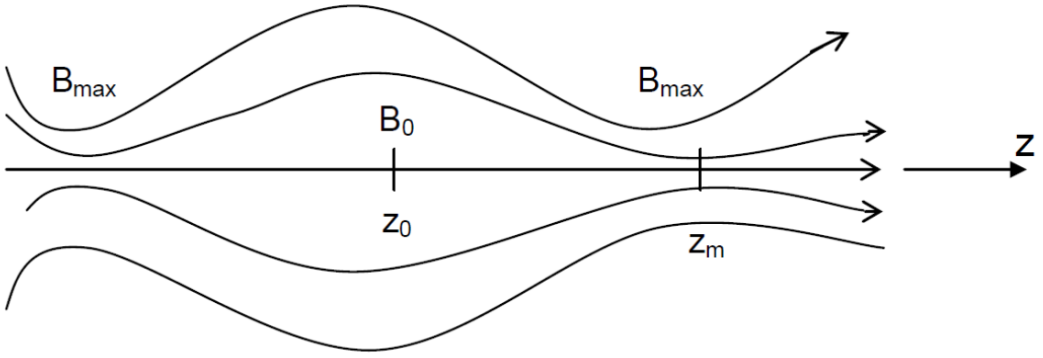

FIGURE 1.3: Schematic diagram of a magnetic bottle, with regions of minimum and maximum magnetic field given by B_{max} at position z_m and B_0 at position z_0. *[Credit D. Whiter, Space Plasma Physics course notes, University of Southampton.]*

It is useful to consider a magnetic field structure called a magnetic bottle, shown schematically in Figure 1.3. Such a structure can be seen as analogous to the dipole magnetic field of the Earth, where a minimum magnetic field B_0 is surrounded by two regions of stronger, maximal magnetic fields of B_{max}. If a particle has an initial pitch angle α_0 at z_0 then, as discussed, the particle will reflect at the point at which the magnetic field strength has increased such that the pitch angle α has increased to 90°. Again, equation 1.13 shows that a smaller initial pitch angle α_0 will require a higher

magnetic field in order to mirror the particle; so the maximum field strength B_{max} of the magnetic bottle structure defines the minimum value of pitch angle that is required for trapping the particle:

$$\sin \alpha_0 > \sqrt{\frac{B_0}{B_{max}}} \tag{1.14}$$

If a particle has a pitch angle $\alpha \leq \alpha_0$ at z_0 in the magnetic bottle, it will escape; any isotropic distribution of particles at z_0 will see some of the population lost if they do not satisfy this condition. The region of solid angle that does not satisfy this condition is known as the loss-cone, a name also given to the "missing" region in the particle distribution. At Earth, particles with a high enough energy parallel to the magnetic field are lost to collisions in the atmosphere as they travel into a region of stronger magnetic field. The loss-cone distribution of electrons in the terrestrial magnetic field is an important factor for magnetosphere-ionosphere coupling and the generation of AKR itself, as discussed in chapter 2.

1.4.3 Non-Zero Electric Fields

The motion of charged particles in a uniform magnetic field has been considered, but the fundamental relationship between electric and magnetic fields has also been elucidated in the description of Maxwell's equations (section 1.3: equations 1.1 to 1.4). Both electric and magnetic fields can be generated by the movement of charged particles and the often opposed drift motion of positively and negatively charged particles. While charge separation in space plasmas can give rise to large-scale electric fields, here we consider the presence of external electric fields at differing orientations to a uniform magnetic field and the effect that this has on single particles.

In the first instance, it is instructive to consider an external electric field that is perpendicular to the previously considered uniform magnetic field. If the magnetic field is aligned such that $\boldsymbol{B} = B\hat{z}$, and the electric field is transversely aligned such that $\boldsymbol{E} = E\hat{x}$, then a proton that is initially at rest will be accelerated towards $\hat{x}$ due to the electric field. Once the proton has a non-zero kinetic energy, the effect of the magnetic field will then accelerate it in $\hat{y}$ due to the Lorentz force as discussed in 1.4.1. The combined effects of these electric and magnetic fields thus produce the same gyromotion about the magnetic field, now with an extra velocity component given by $\frac{E_x}{B}$. This velocity component is perpendicular to both the external electric field and the guiding centre motion along the magnetic field, causing a superimposed drift of the gyromotion in the $-y$ direction. This drift is known as $\boldsymbol{E} \times \boldsymbol{B}$ drift and has the following form (Baumjohann and Treumann, 2012):

$$v_E = \frac{\boldsymbol{E} \times \boldsymbol{B}}{B^2} \tag{1.15}$$

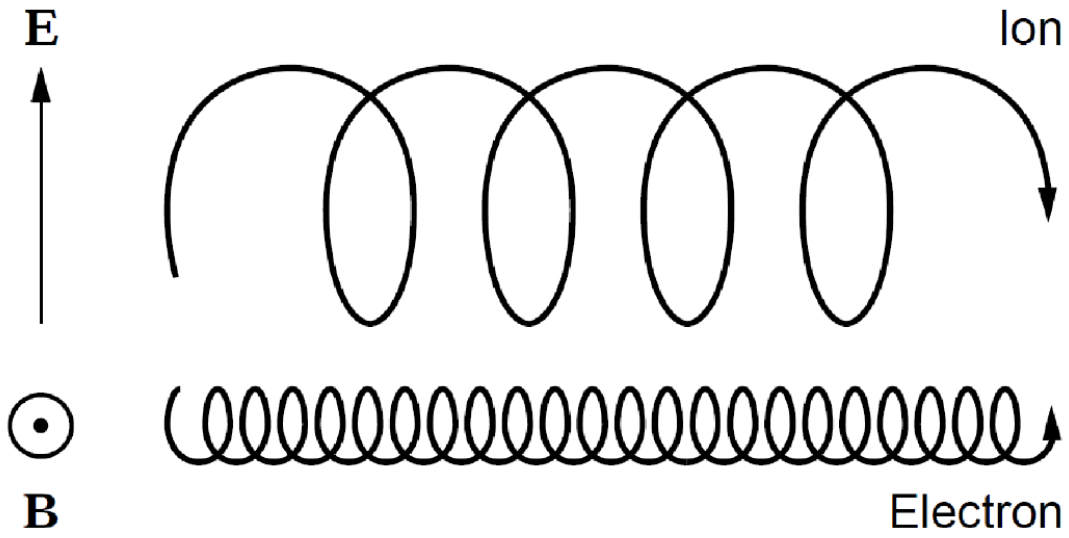

FIGURE 1.4: Schematic illustration of the effect of $\boldsymbol{E} \times \boldsymbol{B}$ drift on the gyroradius of ions and electrons. From Baumjohann and Treumann (2012).

An important feature of this drift motion is that the velocity is independent of the mass, charge, gyration speed and initial conditions of the particle; electrons and protons drift in the same direction as a consequence of the perpendicular electric field. As the electric field also fundamentally affects the direction of motion of charged particles, the gyroradius of ions and electrons are in turn perturbed by its presence. In particular, both electrons and protons undergo acceleration during one half of a single gyration, elongating the trajectory, followed by deceleration which has the opposite effect and shortens the gyroradius (Baumjohann and Treumann, 2012). This is shown schematically in Figure 1.4. The presence of such an electric field is intrinsically dependant on the frame of reference, unlike the magnetic field; non-relativistic flow of plasma in some frame of reference is equivalent to the presence of electric field in that frame, described by $-\boldsymbol{V} \times \boldsymbol{B}$ (Baumjohann and Treumann, 2012). In a space plasma physics context, within the terrestrial system, this equivalence is important for the existence of such an electric field that crosses the polar regions as a consequence of the global convective motion of plasma from the dayside to the nightside of the planet, as seen in section 2.3.

Now considering an electric field with a non-zero component in only the direction parallel to the magnetic field, denoted by $E_{\|}$, electrons and ions will be accelerated along the magnetic field in opposite directions. Thus, in the applied, uniform case, the subsequent charge seperation itself generates an electric field that opposes the original parallel electric field and destroys it. However, in some cases, quasi-static and small-scale parallel electric fields exist and are an important mechanism for particle

acceleration in the high latitude geomagnetic field, as covered in section 2.6. These typically occur in the presence of strong upward magnetic field-aligned currents that are carried by energetic electrons travelling towards Earth, and lead to significant decreases in the electric potential in the field direction, accompanied by an upward-directed electric field (Kivelson and Russell, 1995). The presence of these field-aligned electric potential drops, otherwise known as electric double layers, and the strong currents with which they are associated is difficult to reconcile theoretically; although they are localized and clearly sustained for long enough to effect plasma dynamics (creating some of the brightest and energetic auroral displays, discussed further in section 2.4), observations of these electric field structures suggest a deviance from the suggested models of acceleration due to parallel electric fields (Frank and Ackerson, 1971; Ergun et al., 2001; Treumann, 2006). Analysis of both *in-situ* observations and simulations of the electric field structures and are conducted and still proposed at present to continue to develop our understanding further (e.g. Forsyth et al., 2012; Dunlop et al., 2015; Gunell et al., 2015; Sadeghi and Emami, 2017, 2018, 2019).

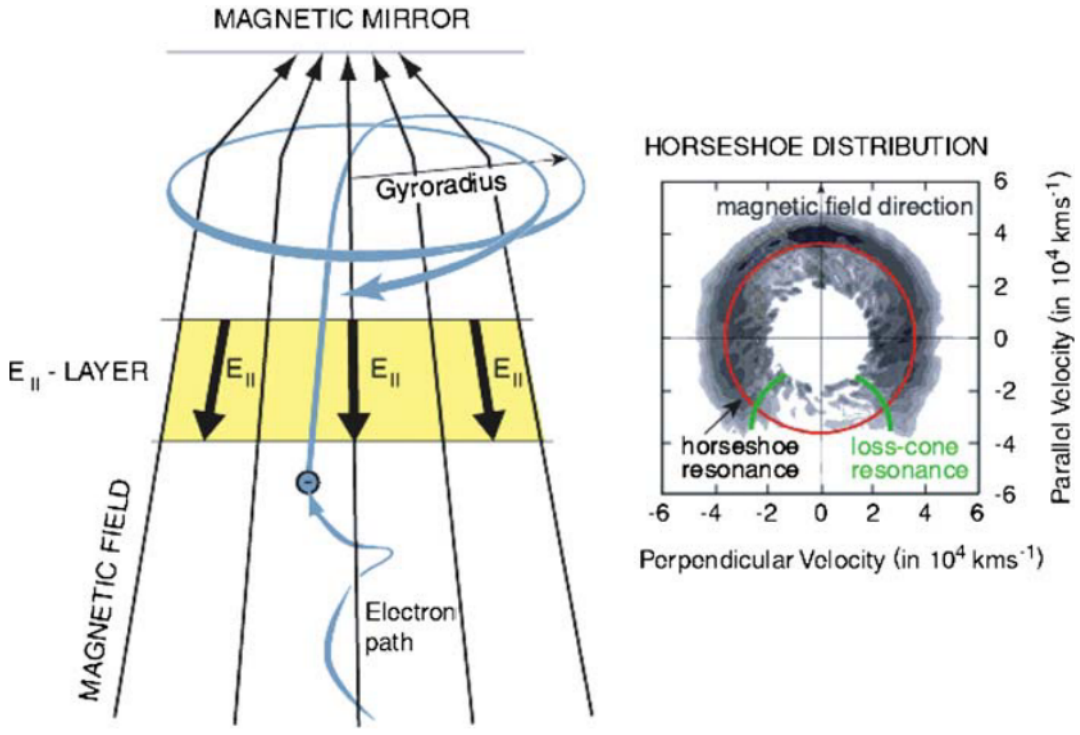

FIGURE 1.5: The left figure shows a schematic of the parallel electric field structure that can exist in the presence of strong current, carried by energetic electrons. The figure on the right shows a "Horseshoe" electron distribution function created by the combination of a parallel electric field creating a ring-like structure, with no low energy electrons at the origin of the plot, and a loss-cone distribution from electrons with a low pitch angle overcoming the mirror force or being lost to collisions in the ionosphere (see Equation 1.14). The red and green lines denote the resonant conditions of each feature, which are not discussed in this thesis. From Treumann (2006).

Such discrepancies are observed in the electron distribution function, as measured by *in-situ* spacecraft that traverse the parallel electric field structures. Section 1.4.1 discussed the effect of the loss-cone on the electron distribution function, which is only a single component of the total distribution function observed in these regions. The distribution function often takes the form of a "horseshoe", where low energy electrons are not observed after being accelerated by such parallel electric fields, but high energy electrons still gain an increased pitch angle while mirroring or contributing to the loss-cone part of the distribution function after being lost to the ionosphere (Treumann, 2006). A schematic diagram of the upward-directed electric field in the context of a converging magnetic field and a magnetic mirror process is seen in Figure 1.5, as well as an example of the horseshoe distribution function. This electron distribution is central to the coupling of the outer magnetosphere and the ionosphere and particularly to the generation of AKR as discussed in section 2.7.

1.5 Magnetohydrodynamics

In section 1.4 we saw how the treatment of single charged particles under the effect of electric and magnetic fields led to an understanding of their motion that leads to several fundamental characteristics of plasma dynamics, which themselves provide insight into important space plasma processes on multiple scales. Another treatment of plasma is that of magnetohydrodynamics (MHD), where the constituents of the plasma are thought of collectively as a fluid. In most situations, it is impossible to consider the motion of every individual particle in the plasma; MHD allows the study of macroscopic properties such as the density, velocity and temperature of a space plasma at large (Baumjohann and Treumann, 2012). This section describes the MHD treatment, where relevant to this thesis.

The induction equation is a useful tool for the discussion of MHD and the interpretation of its various regimes and the regions often found in space plasmas. It describes the temporal change of a magnetic field at a given point in the plasma and is given by:

$$\frac{\partial \boldsymbol{B}}{\partial t} = \nabla \times (\boldsymbol{V} \times \boldsymbol{B}) + \frac{\nabla^2 \boldsymbol{B}}{\mu_0 \sigma} \tag{1.16}$$

where $\boldsymbol{B}$ is the magnetic field, $\boldsymbol{V}$ is the plasma flow velocity, μ_0 is the permeability of free space and σ is the plasma conductivity, itself given by:

$$\sigma = \frac{n_e e^2}{m_e \nu_c} \tag{1.17}$$

where n_e is the number density of electrons, e is the elementary electron charge, m_e is the electron mass and ν_c is the frequency of collisions between plasma constituents, in cases where both collision partners are charged (Coulomb collision) or where one is a

neutral species. The right hand side of the induction equation (1.16) has two terms that describe the subsequent motion of the magnetic field due to the motion of the plasma itself (first term) and diffusion of the magnetic field lines (second term). While the magnetic field motion can see contributions from both effects, often one or the other of the so called convective or diffusive terms is most significant (Baumjohann and Treumann, 2012).

A common way to quantify the significance of each term when describing the plasma via MHD is the Magnetic Reynolds number R_m, a dimensionless quantity given by the ratio of the convective and diffusive terms:

$$R_m = \frac{|\nabla \times (\boldsymbol{V} \times \boldsymbol{B})|}{|\nabla^2 \boldsymbol{B}/\mu_0 \sigma|} \tag{1.18}$$

which can be simplified for a plasma of characteristic magnetic field B_c, characteristic velocity V_c and characteristic length scale L_c to give:

$$R_m \sim \mu_0 \sigma V_c L_c \tag{1.19}$$

The following sections will discuss the regimes in which each of these terms dominate, and some important consequences for the behaviour of space plasmas when considered as an MHD fluid.

1.5.1 Convective Limit and the Frozen-in Theorem

When the Magnetic Reynolds number is such that $R_m \gg 1$, the first term of the induction equation dominates. Considering the case where the plasma conductivity ω is infinitely high, or equivalently that the plasma is completely collisonless, equation 1.16 becomes:

$$\frac{\partial \boldsymbol{B}}{\partial t} = \nabla \times (\boldsymbol{V} \times \boldsymbol{B}) \tag{1.20}$$

Using Faraday's law, given by equation 1.3, it is possible to recover the intrinsic electric field due to the convection of plasma given by $-\boldsymbol{V} \times \boldsymbol{B}$, as discussed in section 1.4.3. Thus the above condition is known as the convective limit, and describes the motion of magnetic field lines with the plasma velocity and the motion of "elements" of the plasma (as opposed to individual constituents). This can be thought of conceptually as a flux tube, a generalised cylindrical surface bounded by closed loops that encircle magnetic field lines such that a fixed amount of magnetic flux is enclosed. The convective limit can also be equivalently described by:

$$\boldsymbol{E} + \boldsymbol{V} \times \boldsymbol{B} = 0 \tag{1.21}$$

which shows that there are no electric fields in the inertial frame that moves with the plasma, and that in a completely collisonless plasma there exist no electric field

components parallel to the magnetic field (Baumjohann and Treumann, 2012). The above is also known as the frozen-in flux theorem, shown graphically by Figure 1.6, and is of consequence for many plasma environments in the solar system and terrestrial magnetosphere.

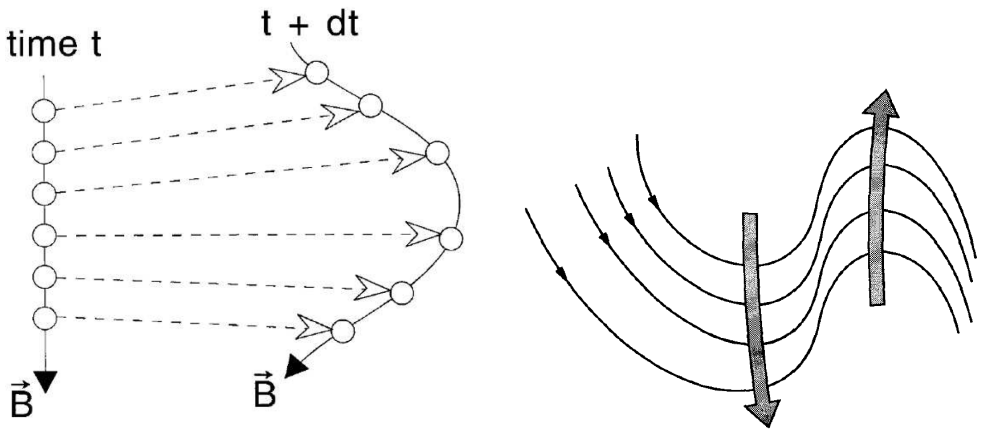

(A) (B)

FIGURE 1.6: Schematic representations of the convective limit or theory of frozen-in flux. A) Individual plasma elements along a field line at two successive times, illustrating the potential consequence in magnetic field line topology as plasma elements move with different velocities *[Credit D. Whiter, Space Plasma Physics course notes, University of Southampton.]*. B) Extension of the schematic concept to the bulk motion of plasma along magnetic field lines. Taken from Baumjohann and Treumann (2012)

As the frozen-in flux theorem is represented by a large Magnetic Reynolds number, equation 1.19 shows that these conditions can also be achieved by large characteristic velocities and length scales of the plasma, for example in the lobes of the magnetosphere or the regions of higher altitude in the terrestrial ionosphere (both discussed further in section 2.1).

The frozen-in theorem has distinct consequences in space plasma environments, which vary depending on the dominant form of energy density or pressure present. The plasma not only has a pressure in the typical sense, related to its bulk flow and given by $n\langle m_i \rangle V^2$ where n is the plasma number density, $\langle m_i \rangle$ is the average mass of ions and V is the plasma velocity, but also pressures due to both the thermal motion of the plasma constituents and the magnetic field itself. The thermal pressure is given by nk_bT, where n is again the number density, k_b is Boltzmann's constant and T is the plasma temperature. The magnetic pressure is given by $\frac{B^2}{2\mu_0}$, and acts in a transverse direction to the magnetic field; it can be thought of as a force that acts to return equilibrium to the field when it is distorted and field lines converge. In an ideal case, where the plasma is quasineutral, isotropic, and exists in equilbrium, the plasma beta can be defined as the ratio of the thermal to magnetic pressures:

$$\beta = \frac{2\mu_0 n k_b T}{B^2} \tag{1.22}$$

The value of the plasma beta dictates whether the flow of the plasma dominates the magnetic field under frozen-in conditions, such that for $\beta > 1$ the magnetic field follows the motion of the plasma. This is also the case when the plasma velocity is high enough that the dynamic pressure of the plasma is dominant (which also leads to a high value of the magnetic Reynolds number as shown in equation 1.19). In the case that $\beta < 1$ the magnetic field lines constrain the plasma, which can then only move if they themselves undergo motion (as in the case of global convective motion of field lines in the Dungey cycle, explained in section 2.3).

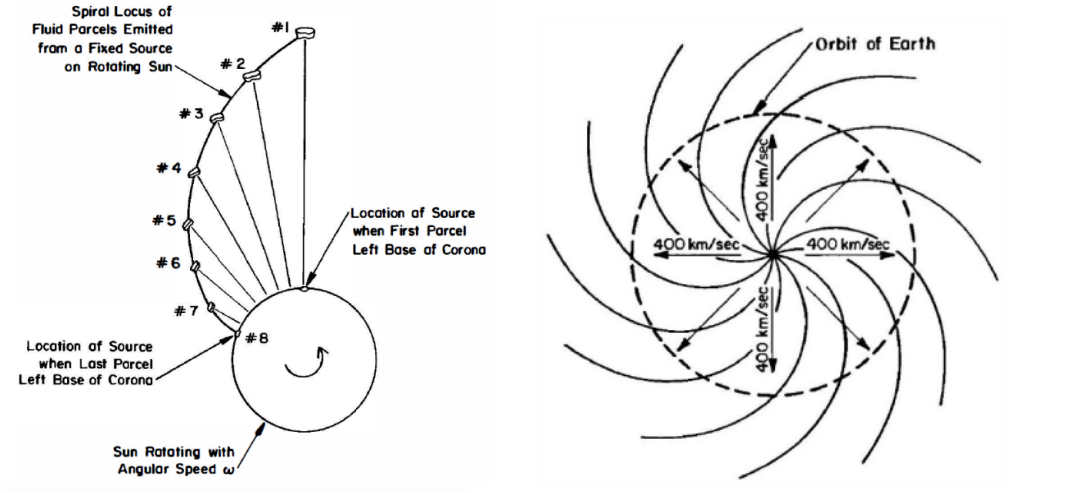

(A) (B)

FIGURE 1.7: A) Schematic illustration of "packets" of solar wind plasma emitted radially from the surface of the rotating Sun and being dragged into a spiral shape as they travel, frozen in to the magnetic field. From Kivelson and Russell (1995). B) The overall Parker spiral structure projected in two dimensions. From Baumjohann and Treumann (2012).

A particularly important consequence of the frozen-in theorem is of that in the solar wind. As the Sun rotates, plasma is ejected radially from the surface of the Sun at all times. The Magnetic Reynolds number is high in this region, and the solar wind velocity is high enough such that the field lines follow the motion of the plasma. The plasma elements ejected from the surface at a given time thus have a different direction to those ejected at a previous time, and so the solar wind and subsequently the Sun's magnetic field is dragged into a spiral pattern as it extends into the solar system; this structure is known as the Parker spiral. This concept is illustrated in Figure 1.7. The solar wind plasma and its motion with the magnetic field, known as the interplanetary magnetic field (IMF), sees current sheets form that also follow the spiral shape. These are constrained by the direction of the IMF, depending on it being either towards or away from the Sun; the resulting shape is illustrated in Figure 1.8. The dynamics of Earth's magnetic environment depend on the properties of the solar wind and the IMF when they reach it, particularly the IMF direction, which can

provoke plasma and energy transport via magnetic reconnection when in a variety of configurations. This is discussed further in sections 2.1 and 2.2.

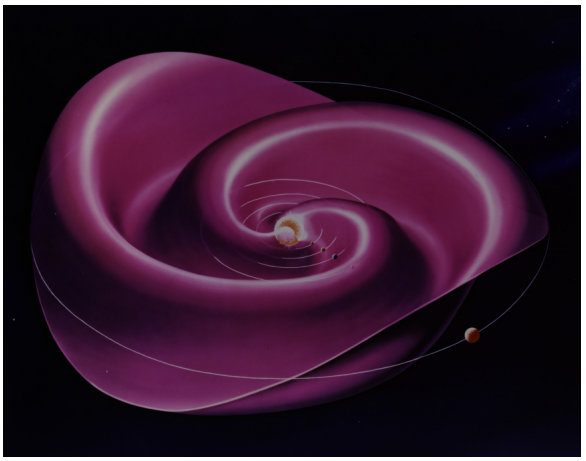

FIGURE 1.8: Artists rendition of the Parker spiral and current sheet geometry resulting from the solar wind plasma, frozen in to the IMF as it flows away from the rotating Sun. Image from NASA.

1.5.2 Magnetic Reconnection

Using the induction equation (1.16) in the case of a collisionless plasma we have seen that it can be treated as a fluid that either carries the magnetic field with it or moves with the magnetic field, dependant on the dominant form of pressure within the plasma. For a plasma at rest, or one with a small characteristic length scale such as a current sheet, or when a finite resistance exists, the magnetic reynolds number $R_m \ll 1$ or at most approaches unity and the induction equation becomes:

$$\frac{\partial \boldsymbol{B}}{\partial t} = \frac{\nabla^2 \boldsymbol{B}}{\mu_0 \sigma} \tag{1.23}$$

This has the form of a diffusion equation in the magnetic field; the diffusion coefficient in this case is given by $(\mu_0 \sigma)^{-1}$, and describes the motion of the magnetic field to tend to decrease in local regions of higher magnitude. Importantly, as this signifies the breakdown of ideal MHD conditions, the plasma is free to move across magnetic field lines and vice versa. In cases where separate magnetic field structures are forced to interact following in regions dominated by diffusion, the larger scale topology of the field can be modified. A specific case of this change in topology in a region characterised by magnetic diffusion, known as magnetic reconnection, is shown in figure 1.9, and the physical process itself has important consequences for the transfer of plasma and energy in general within space plasma environments (Baumjohann and Treumann, 2012).

A boundary can be considered in which two flux tubes with oppositely aligned magnetic field exist close to one another and under frozen-in conditions. It can be the

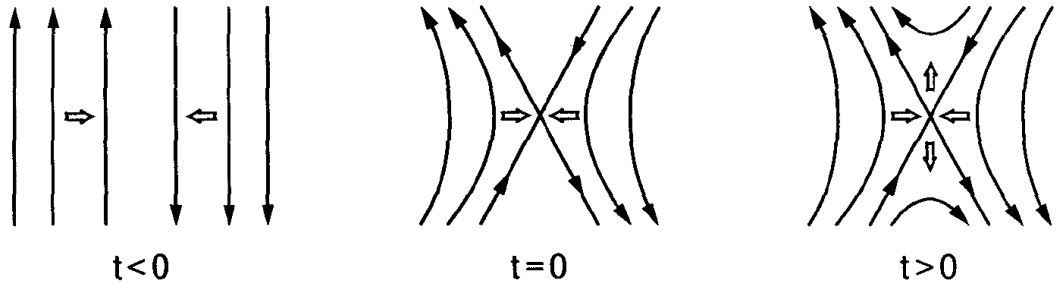

FIGURE 1.9: Schematic illustration of the process of magnetic reconnection. In a small, diffusive region of plasma at $t < 0$, antiparallel field lines are forced together and form a current sheet. At $t = 0$, the magnetic field topology changes within the center of the diffusive region. At $t > 0$ plasma is forced from the center of the diffusive region and is ejected away from the site of reconnection in a direction parallel to the previously existing magnetic configuration. Taken from (Baumjohann and Treumann, 2012).

case that the plasma and thus the magnetic field is relatively stable, and can exist in this configuration for prolonged periods. The layer between the two magnetic fields is often thin and is known as a neutral layer or current sheet; often the two sides of antiparallel magnetic fields move towards the neutral layer, compressing the layer into a thinner structure (as shown on the left at time $t < 0$ in figure 1.9). In these cases, the magnetic diffusion begins to dominate, and the frozen-in approximation of the plasma motion breaks down. As well as the plasma moving freely from the magnetic field lines, the increased resistivity in the small diffusion region (know as the neutral point) allows the magnetic field lines themselves to disassociate from the previous topology and reconfigure within the centre of the neutral layer. This is shown in the centre of figure 1.9 at time $t = 0$, with the closest parts of the previously oppositely opposed field lines joining in the diffusion region (characterised by an "X" in the figure). The plasma from either side of the neutral layer also moves towards the neutral point during this process and is able to mix, given the breakdown of frozen-in conditions. On the rightmost panel of figure 1.9, at $t > 0$, the plasma that has mixed within the diffusion region is ejected in both directions parallel to the original orientation of the magnetic field lines. If there is a consistent pressure that forces the antiparallel field lines together, with the frozen-in plasma that moves with them as is the case at $t < 0$, the process of magnetic reconnection continues (Baumjohann and Treumann, 2012). While the small diffusion region or neutral point, where the original magnetic field topology is reconfigured, is represented as a single point in figure 1.9, the thin neutral layers or current sheets are usually spatially extended. As a result of this, the physical process of reconnection typically occurs along a neutral line instead of a neutral point, such that the X-shaped configuration extends across the layer. As mentioned, the process of reconnection is central to the reconfiguration and transport of energy in the terrestrial magnetosphere; reconnection at the current sheet at the boundary between the Earth's magnetic field and the interplanetary magnetic field facilitates energy input to the otherwise closed terrestrial system, and the current sheet between the

lobes of the magnetotail is often host to reconnection that precedes energetic dynamics and can reconfigure the large-scale structure (e.g. W Hones Jr, 1985; Liou, 2002).

1.6 Summary

Beginning with a description of Maxwell's equations (equations 1.1-1.4) and a simple consideration of the motion of single charged particles under the effect of static electric and magnetic fields (section 1.4), this chapter has introduced the basic concepts of plasma physics relevant to the space environment. While the real physics observed in nature often requires further detail to explain, these approximations hold well enough that they contribute to more complex interactions in the plasma. For example, the gyration of electrons about magnetic field lines and their loss to the upper atmosphere as a consequence of their energy via acceleration is fundamental to the generation of the auroral kilometric radiation (AKR) that is the topic of this thesis (see section 2.7). The large-scale structure of the magnetosphere of Earth (and other magnetised planets, not considered here) can be partly derived with the concepts of convection electric field in equivalence with plasma motion, as described in section 1.4.3. As will be seen in section 2.1, the pressure boundaries that arise from different space plasma environments such as the solar wind and the magnetic field of Earth itself form the global, large-scale structure that dominates any interaction considered here, and has a fundamental impact on the way energy is transported such as in reconnection at the dayside and in the magnetotail (discussed in section 1.5.2 and further in section 2.3). The following chapter applies the concepts developed here to the terrestrial magnetosphere in more detail, and sets the context for the work included in this thesis.

Chapter 2

The Magnetosphere and Coupling with the Ionosphere

With the development of space-borne instrumentation, with in-situ and remote sensing capabilities, and ground-based observatories we have been able to characterise the terrestrial magnetosphere in detail for decades. Via exploration of this magnetic environment we have begun to understand how energy is transported throughout this system; this chapter focuses on our knowledge of the terrestrial magnetosphere, its energy pathways and relevant phenomena, and the auroral radio emissions which are the focus of the later chapters in this thesis.

2.1 Formation of the Terrestrial Magnetosphere

2.1.1 The Solar Wind and Interplanetary Magnetic Field (IMF)

As mentioned in section 1.5.1, the Sun constantly emits plasma from its complex atmosphere and thus transmits energy throughout the heliosphere. Known as the solar wind, this plasma is relatively sparsely populated, with electron densities on the order of $\sim$ 1-10 cm^{-3} (Kivelson and Russell, 1995). The solar wind is frozen in to the Sun's magnetic field, and the plasma parameters such as its density, temperature, speed and magnetic field strength and orientation, as well as their evolution, are important to understand as they have a direct impact on both the global structure and internal dynamics of the Earth's magnetosphere and those of other planetary environments throughout the solar system. The outward expansion of the solar wind is controlled by the pressure imbalance between the hot solar wind and the comparatively cool and tenuous plasma of the interstellar medium, far outside of Earth's orbit at the boundary of the heliosphere at around 160 astronomical units (AU; 1 AU = 1.5×10^{11} m). With observations of the solar wind and plasma via spacecraft

near Earth at 1 AU, the properties of the interplanetary medium are now well understood. The solar wind speed is supersonic with values ranging between 300-1400 km s^{-1}, the interplanetary magnetic field (IMF) has field magnitudes of 5-10 nT, the temperature of the plasma for both electrons and protons is around 10^5 K, and the heavier protons of the plasma carry much of the energy and momentum outwards in a radial direction that is approximately parallel to the ecliptic plane that contains the Earth's orbit (Kivelson and Russell, 1995). The momentum and energy carried by the solar wind is known as its dynamic pressure.

The solar activity dictates the initial speed of the solar wind, with higher temperatures in the upper atmosphere of the Sun corresponding to higher solar wind speeds. Given the large distances over which the solar wind travels, interactions between regions of faster and slower solar wind plasma also causes further variability. While the frozen in conditions of the solar plasma creates the Parker spiral and the general spatial configuration of the IMF, as discussed in section 1.5.1, the local orientation of the IMF measured at Earth also varies based on the movement of large structures in the solar wind (Baumjohann and Treumann, 2012). Energetic phenomena like coronal mass ejections, which see large amounts of plasma ejected from the solar surface, can propagate throughout the solar system to become interplanetary coronal mass ejections (ICMEs) that interact with planetary magnetic environments. As they pass Earth, electron beams and magnetic flux "clouds" are measured, and these can also have an effect on the magnetosphere via the changing state of the solar wind (Gosling et al., 1990; Zurbuchen and Richardson, 2006). The impact of an ICME at Earth is investigated in chapter 6. In the general case of the IMF, the changing orientation can provide more or less ideal conditions with which the solar plasma couples to the Earth's magnetosphere and changes its dynamics, while the relative differences between the plasma properties of the two systems provide the large scale structure of the magnetosphere itself. This latter structure shall be explored in the following section 2.1.2, while the internal dynamics will be detailed in section 2.3.

2.1.2 The Terrestrial Magnetosphere

The terrestrial magnetic field can be approximated as dipolar relatively close to the planet, forming closed loops between the Northern and Southern magnetic hemispheres of the Earth. While plasma can be both introduced and ejected from the magnetosphere via processes such as reconnection (see section 1.5.2), it is also constrained and circulated within the magnetosphere by the frozen-in theorem, the adiabatic invariant properties of the plasma and external forcing from the solar wind. The magnetosphere and the various regions that will be described in this section are host to plasma of typically lower density than the solar wind; thus acting as a

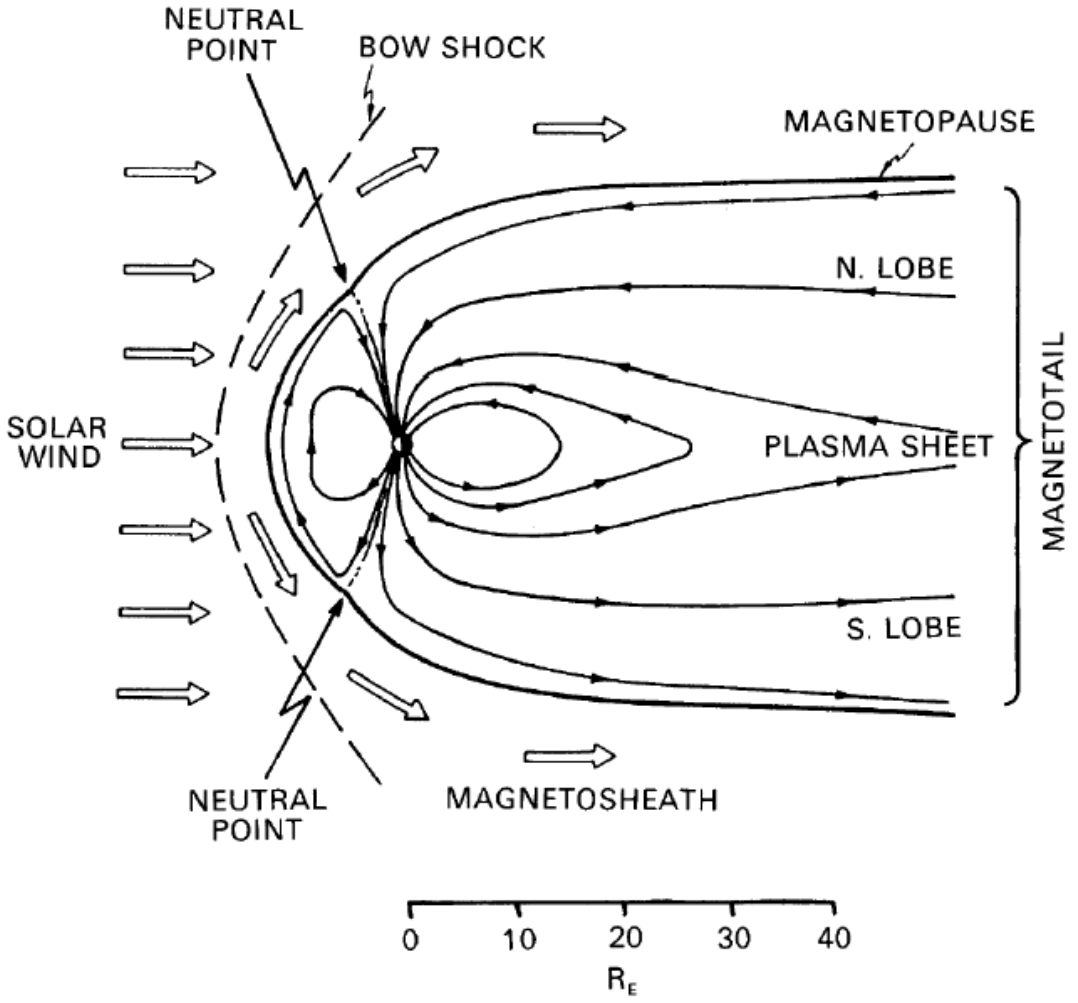

FIGURE 2.1: Schematic diagram of the terrestrial magnetosphere demonstrating the shape of its regions under the effect of the IMF and solar wind. From Hunsucker and Hargreaves (2002).

bubble-like cavity, surrounded by the solar wind plasma and the IMF. A schematic diagram of the magnetosphere is shown in Figure 2.1 with its various regions labelled.

The dayside magnetosphere is the region which experiences the greatest impact from the solar wind as it is met by the fast and dense plasma at the subsolar point; the point at which the Sun is at zenith, projected to the boundary between the terrestrial magnetosphere and the solar wind. The solar wind plasma slows when it meets the magnetic environment of the Earth and creates a shock wave. This deflected boundary, known as the bow shock, extends around the closed dipolar field of the dayside, where the supersonic solar wind plasma slows and thermalises, forming a layer of turbulent plasma known as the magnetosheath behind the bow shock (Baumjohann and Treumann, 2012). Behind the magnetosheath there is a thin boundary of plasma known as the magnetopause, which is created at a point of pressure equilibrium between the solar wind and the magnetosphere. This

equilibrium is determined by the external dynamic pressure of the solar wind and the internal magnetic pressure of the geomagnetic field; the region of space that it occupies is home to the primary coupling process of reconnection that allows solar wind plasma to enter the magnetosphere. The rate of magnetic reconnection that occurs is dictated by properties of the IMF, namely its orientation with respect to the geomagnetic field, as well as the solar wind speed (Baumjohann and Treumann, 2012). This is discussed in more detail in section 2.3.

Due to the compression of the dayside magnetosphere by the solar wind, the combined structure of the bow shock, magnetosheath and magnetopause is approximately conical. The magnetospheric structure on the nightside is much different, however. The high dynamic pressure of the solar wind continues to affect the global structure as it enswathes the magnetosphere and lengthens magnetic field lines to around 10^3 R_E (1 R_E = 6371 km) in an antisunward direction. As denoted in Figure 2.1, the magnetotail consists of the magnetospheric lobes, regions of lower density plasma in both the Northern and Southern magnetic hemispheres, and the plasma sheet that lies across the magnetic equator on the nightside. While the inner magnetosphere on the nightside retains an approximately dipolar field close to the planet, the field is distorted past approximately 10-15 R_E. The neutral current sheet is a layer of dense, hot plasma between the magnetotail lobes, within the plasma sheet. The flow of diamagnetic current in this region is central to dynamics that occur when energy is released in the tail and, like the magnetosphere in general, is subject to fluctuations based on the state and conditions of the solar wind and the IMF. Namely, when the solar wind is more energetic, the current sheet is compressed and becomes thinner with a higher current density (Baumjohann and Treumann, 2012).

The plasma within the magnetosphere is not static but moves on large-scale as well as particle-scale motion, controlled to an extent by the adiabatic invariant properties and the effects of the presence of the magnetic and electric fields (as discussed in section 1.4). This creates regions within the magnetosphere with characteristic plasma properties like density and temperature and can be recognised as such, although variability is also seen when the system is disturbed from solar forcing (Baumjohann and Treumann, 2012). The radiation belt is a region of energetic plasma between 2-6 R_E that encircles the Earth and between this population and the Earth's atmosphere is the plasmasphere, containing much colder and denser plasma. Of particular interest here, however, is the extent of the plasma sheet from the magnetotail to the auroral ionosphere at high-latitudes. This connection is integral to the energetic injection of plasma during space weather events such as substorms, described in detail in section 2.4, but also for dynamic coupling between the outer and inner magnetosphere in general.

The ionosphere is a component of Earth's upper atmosphere that lies above altitudes of 80 km. Due to the much lower rate of recombination in this region, there is a

permanently ionised population of electrons and ions, arising from diurnal solar photoionisation as well as the precipitation of energetic protons and electrons. This precipitation, which gives rise to the auroral emission that characterises the nightside ionosphere at high latitudes, not only transfers energy from the magnetotail but also strengthens current pathways that will be discussed further in section 2.5. As the magnetic field lines connect the high latitude ionosphere to the magnetotail and plasma sheet, observations of the ionospheric currents and plasma processes that occur along these field lines deliver a proxy to behaviour in the outer magnetosphere. Thus the combination of these regions is known as the magnetosphere-ionosphere (MI) coupling region, and is of particular significance to this work. High latitude ionospheric currents in the Westward direction intensify during substorms (discussed further in section 2.4), while more steady plasma circulation processes are indicated by a more symmetrical response in both Westward and Eastward directions near the polar ionosphere (see sections 2.3 and 2.5). The Westward and Eastward electrojets are illustrated in the bottom left panel of Figure 2.4.

2.2 Reconnection in the Magnetosphere

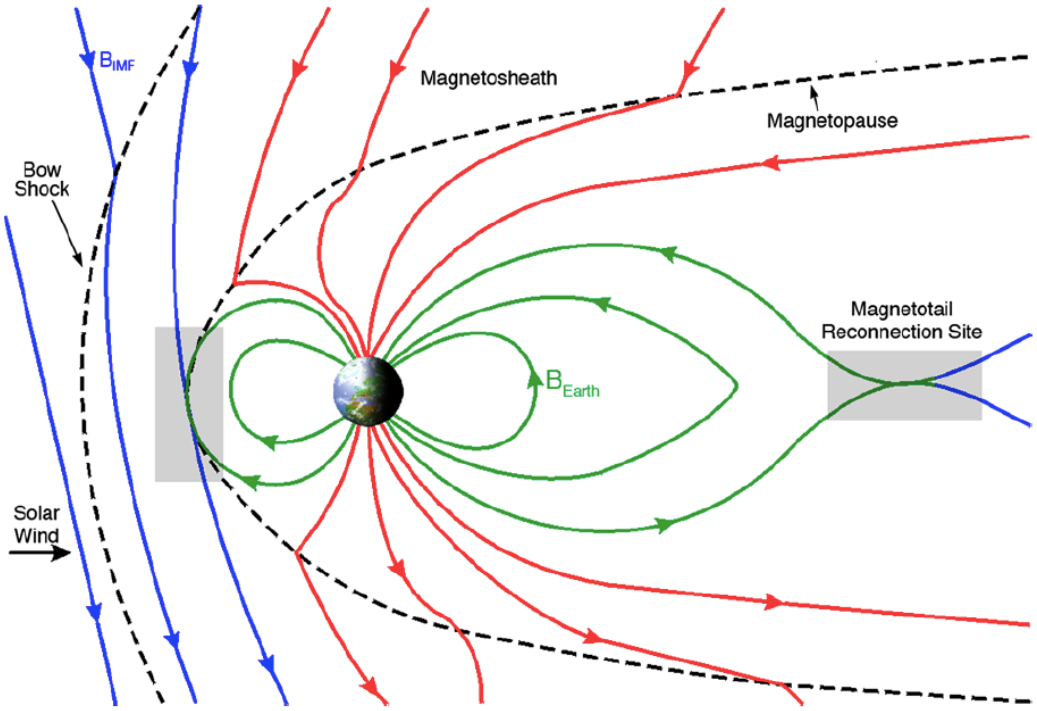

FIGURE 2.2: Schematic of the Earth's magnetosphere with grey shaded regions showing the primary sites of magnetic reconnection for considering magnetospheric dynamics. The IMF is shown in blue, the terrestrial magnetic field is shown in green, and open field lines following reconnection between the closed terrestrial field and the IMF are shown in red. From Fuselier and Lewis (2011).

As discussed in section 1.5.2, the process of magnetic reconnection is vital to the reconfiguration of the magnetosphere that facilitates the transport of energy from the solar wind. Both the day and night sides of the Earth are host to regions in which magnetic field lines can meet with an antiparallel alignment and thus reconnect; across the dayside magnetopause surface and in the plasma sheet, between the two magnetotail lobes. These regions are presented in Figure 2.2, which shows the solar wind arriving at the dayside magnetosphere with the IMF in blue. The closed terrestrial magnetic field is shown in green. On the dayside the Northward facing geomagnetic field can reconnect with the IMF when the latter is in a certain configuration; a Southward facing ($B_z < 0$) component results in reconnection with the dipolar, Northward facing, terrestrial field. Following this, the previously closed terrestrial field lines are now connected from the polar regions of Earth to the external IMF. The rate of reconnection that occurs on the dayside depends on the solar wind speed and the particular configuration of the IMF, which has multiple components in the magnetic frame of the Earth. The reconnection rate can be parameterised by (Milan et al., 2008):

$$\Phi_D = v_x L_{eff} \sqrt{B_y^2 + B_z^2} \sin^2\left(\frac{\theta}{2}\right) \tag{2.1}$$

where v_x is the x-component of the solar wind speed, L_{eff} is the effective length of the reconnection region, B_y and B_z are the y and z-components of the IMF at the magnetopause, where the components follow that of the geocentric solar magnetic coordinate system. θ is the clock angle, or the angle between the IMF and the geomagnetic field at the magnetopause as seen in the xz-plane; thus the dayside reconnection rate Φ_D has a minimum value for field lines that meet at parallel and a maximum for antiparallel field lines. Equation 2.1 is just one of the parameterisations that represent dayside reconnection as the coupling relationship is complex; although using a different expression, the rate of dayside reconnection is used to evidence the timeline of energy transfer into the magnetosphere and the dynamics that follow in a case study in chapter 6.

In the magnetotail, the geomagnetic field lines are dipolar-like within approximately 10 R_E but are stretched into a non-dipolar configuration further away from the planet on the nightside, following the dynamic influence of the solar wind. However, the orientation of the field is retained such that field lines that close in the Northern hemisphere are directed towards Earth and those that close in the Southern hemisphere are directed away from Earth. When the dayside reconnection rate is high, the magnetic flux that is added to the internal magnetosphere compresses the field lines in the magnetotail, bringing the magnetic field in the lobes to a more antiparallel configuration and creating a diffusion region in which reconnection occurs; again shown by the right-most grey shaded region in Figure 2.2. In the

following section 2.3, the consequences of balanced, steady-state rates of reconnection between the dayside and nightside are explained in detail.

2.3 Plasma Convection and Energy Release: The Dungey Cycle

As described in the previous section 2.2, reconnection occurs at both the dayside and nightside of the Earth, and leads to the flow of energy and plasma throughout the magnetosphere. When the rates of reconnection at these sites are roughly balanced, the transport of plasma can be modelled by a process known as the Dungey cycle. Figure 2.3 shows a schematic illustration of the magnetosphere, with both a cut in the XZ plane and the polar and auroral regions, and numerically denotes the position of a given magnetic field line or its footpoint throughout the Dungey cycle.

When dayside reconnection occurs, closed geomagnetic field lines meet the IMF along the equatorial magnetopause (represented by 1 and 1′ respectively in Figure 2.3). Subsequently opened field lines that map to the IMF are labelled 2 and 2′ in Figure 2.3. The opening of magnetic field lines on the dayside combined with the velocity of the solar wind manifests an electric field that traverses the polar cap in a dawn-dusk direction; this is equivalent to the anti-sunward motion of plasma across the polar cap, which carries the newly opened field lines downtail (3 and 3′; 4 and 4′).

The influence of the solar wind drapes the field lines over the magnetosphere and into a tail-like configuration as discussed in section 2.1. As opened field lines from both hemispheres meet in the tail (5 and 5′), a neutral current sheet is formed in the equatorial plane and magnetic flux is loaded into the lobes of the tail; the regions of tenuous plasma above and below the approximately planar plasma sheet. As the region between the opposing field lines diminishes, reconnection occurs in the tail (6 and 6′), forming newly-closed field lines that reach the Earth at high latitudes in either hemisphere (7) as well as an open field line that travels downtail to eventually become the IMF (7′). During substorms (see section 2.4), two sites of reconnection in the tail can create a closed loop of magnetic flux known as a plasmoid, that also travels downtail as the magnetic field Earthward of the reconnection sites dipolarises.

The Earthward-travelling plasma released during reconnection on the nightside influences the newly-closed field lines closest to Earth, recreating the dipolar state of the terrestrial field (8). As seen in the schematic of the magnetic footpoints within the polar cap in Figure 2.3, the closed field lines return to the dayside on both dawn- and dusk-flanks of the magnetosphere (9). This motion of plasma and the magnetic field creates a two-cell convection pattern in the ionosphere that follows equipotential contours of the associated electric fields, and roughly describes the motion of flux

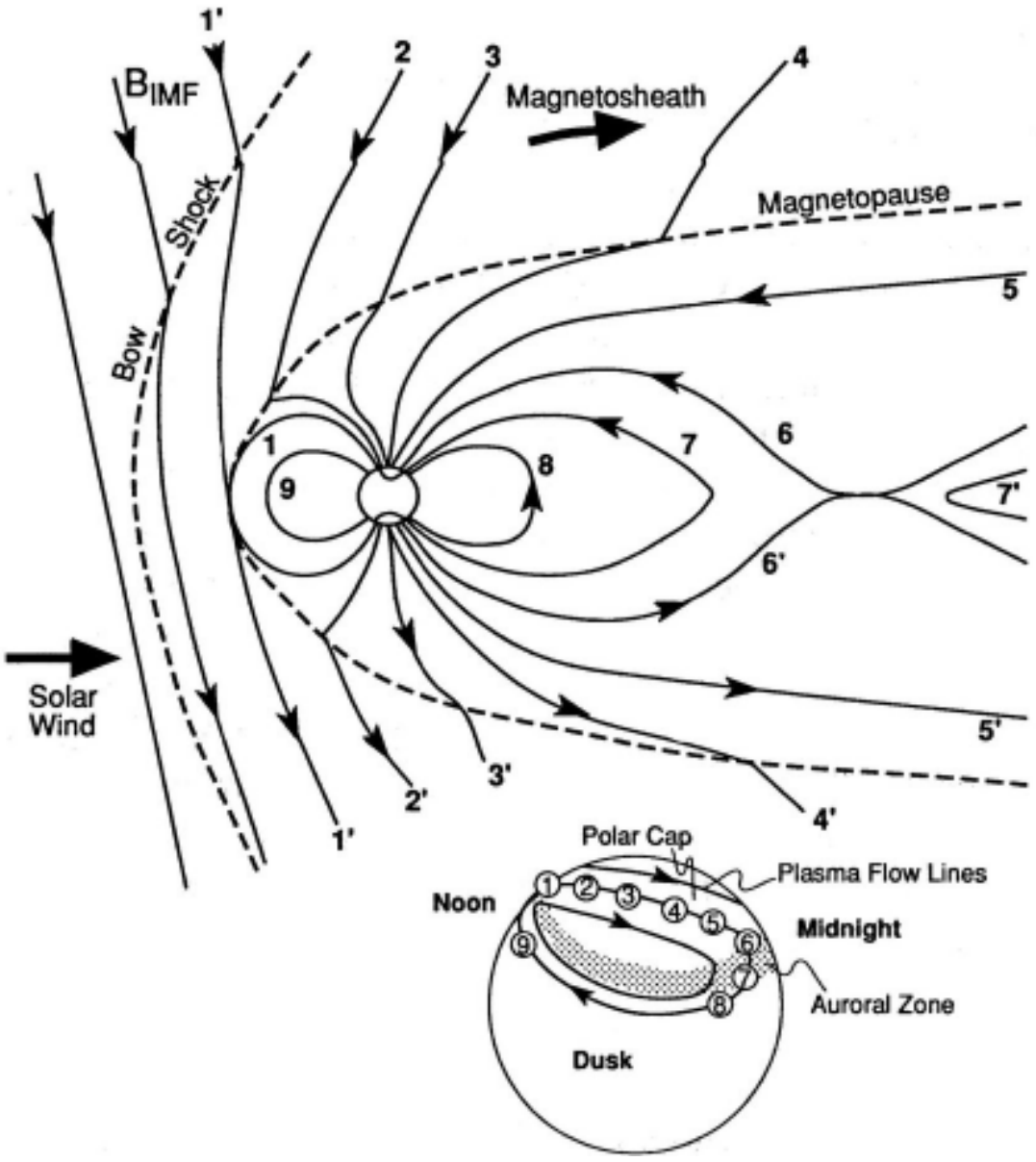

FIGURE 2.3: Schematic diagram of the solar-wind-magnetosphere interaction on the dayside, with numbers indicating stages of plasma convection during the Dungey cycle. Inset figure in the bottom right shows the analogue stages with context of ionospheric plasma motion across the polar cap. Taken from Kivelson and Russell (1995).

tubes in either hemisphere under a steady-state condition. Measurements of correlation timescales between propagation of IMF conditions and the effects on the magnetotail lead to an approximate value of ∼1-4 hours for open field lines to travel across the polar cap and enter the magnetotail, with faster times for a higher dayside reconnection rate under Southward IMF conditions (Milan et al., 2007; Fear and Milan, 2012; Browett et al., 2017). Assuming the same speed of plasma for return flow from the nightside to the dayside, and a circular auroral oval, the flow of the magnetic field lines that comprises the Dungey cycle takes ∼4-16 hours in total.

Whether or not this process occurs in a quasi-steady state or otherwise is dependent

on the temporal variation of the IMF, and can affect the magnitude of the response of the geomagnetic field and high-latitude ionosphere. Discrepancies between the rate of dayside and nightside reconnection can lead to significant loading of magnetic flux and energy into the magnetotail, prior to explosive unloading. These concepts are central to the energetic release of plasma within the magnetosphere and particularly at the most energetic point of the phenomenon that is discussed in the following section 2.4 (Baumjohann and Treumann, 2012).

2.4 Substorms

Substorms are space weather events that are characterised by various plasma dynamics under changing magnetospheric configurations and orientations of the interplanetary magnetic field (IMF). They cause high spatial and temporal variability within the high-latitude, auroral ionosphere and transfer and deposit energy throughout the magnetosphere during events that have been modelled as an archetypal three-phase process. The growth, expansion and recovery phases of a substorm each have distinct, observable features that, whilst occuring over a large spatial region, can be imaged by both ground-based and in-situ instruments. This section characterises the accompanying phenomena of these features.

Throughout the lifetime of a substorm, energy and current is unloaded into the magnetosphere as the system responds to the increased magnetic flux following periods of imbalanced reconnection rates between the terrestrial dayside and nightside; distinct from the steady-state Dungey cycle as described in section 2.3. If the nightside reconnection rate is less than that on the dayside the magnetic flux builds in the magnetotail, causing it to lengthen and the plasma sheet to compress. This comprises the growth phase of the substorm (McPherron, 1970); the auroral oval moves equatorward as the polar cap increases in size with the building magnetic flux (Pulkkinen et al., 1991; Gjerloev et al., 2003).

The nature of the energetic loading of the magnetotail during the growth phase leads to a volatile release of energy over a timescale of the order of tens of minutes (e.g. Forsyth et al., 2014; Partamies et al., 2015). While the exact spatial and temporal timeline of the initiation of this process is still not fully understood, it is thought that a critical state is reached following the development of instabilities between the plasma sheet and high latitude magnetic field lines on the nightside. A detailed discussion of the primarily discussed causal pathways for this process is deferred here, although the reader is referred to the following (e.g. Mende et al., 2011; Kalmoni et al., 2015; Akasofu, 2021). This energetic release, accompanied by relatively localised, intense Westward currents in the ionosphere as well as reconnection in the magnetotail, is known as the expansion phase of the substorm.

During the expansion phase, intense local brightenings at the equatorward boundary of the auroral oval occur for a few minutes, preceding the increase in auroral activity across the extent of the nightside oval. The boundary expands further poleward at about 200 ms^{-1} as intense East-West aligned arcs spread across the longitudinal extent of the auroral zone on the nightside and intricate auroral forms are seen at high latitudes due to the significantly increased conductivity of the auroral oval, typically following an increase in energetic electron precipitation (Akasofu, 2017). These dynamic auroral displays at expansion phase onset have been studied at great length. The development of auroral forms and structure common to the expansion and recovery have been characterised by both auroral all-sky cameras (Akasofu, 1964) and UV global imagers (Frey, 2004). Other work has studied weaker substorm events and associated pseudobreakups of auroral forms (Kullen and Karlsson, 2004) and statistical studies have been carried out to identify the extent of the variation of auroral activity (Nishimura et al., 2010). The extreme auroral changes are coincident with a surge in the westward electrojet (e.g. Weimer et al., 1994), a high latitude current that is driven by the diverted magnetotail current (McPherron et al., 1973; Lui, 2013; Forsyth et al., 2014; Kepko et al., 2015; Forsyth et al., 2018), and which will be discussed in the following section 2.5.3.

As field lines are closed and the energy stored in the tail dissipates, the magnetosphere and the terrestrial ionosphere return to a quiet state under new IMF conditions. Thus, in the recovery phase, the auroral brightness decreases and structures become dispersed as the system either returns to a quiet state in a more stable dipolar configuration (W Hones Jr, 1985) or continues to drive further releases of energy as multiple expansion and recovery phases taking place (Kepko et al., 2015; Akasofu, 2017; Sangha et al., 2020).

Lists of substorm onset events, defined either by the extreme auroral brightening or thresholds on the variation of the geomagnetic field associated with changing currents, have been compiled. Although the former method allows for clear visual identification of events (e.g. Frey, 2004), an automatic process that is less open to subjectivity is more appropriate for a comprehensive list. The continuity of the measurements of the ground magnetometer networks has been utilised by algorithmic approaches, and more recently with an algorithm based on free statistical parameters; resulting lists have been found to agree well with those previously-compiled (Forsyth et al., 2015). The strengthening of this current system is typically used to define onset as it produces a clear signature in the deflection of the Northward component of the terrestrial magnetic field, as measured by ground magnetometer stations; networks of these stations have been used to monitor this characteristic signature (Newell and Gjerloev, 2011), and are discussed further in section 2.5.2. In-situ measurements also allow the phase of the substorm to be inferred, with satellites on the nightside being able to observe dipolarisations in the magnetotail as well as make measurements of

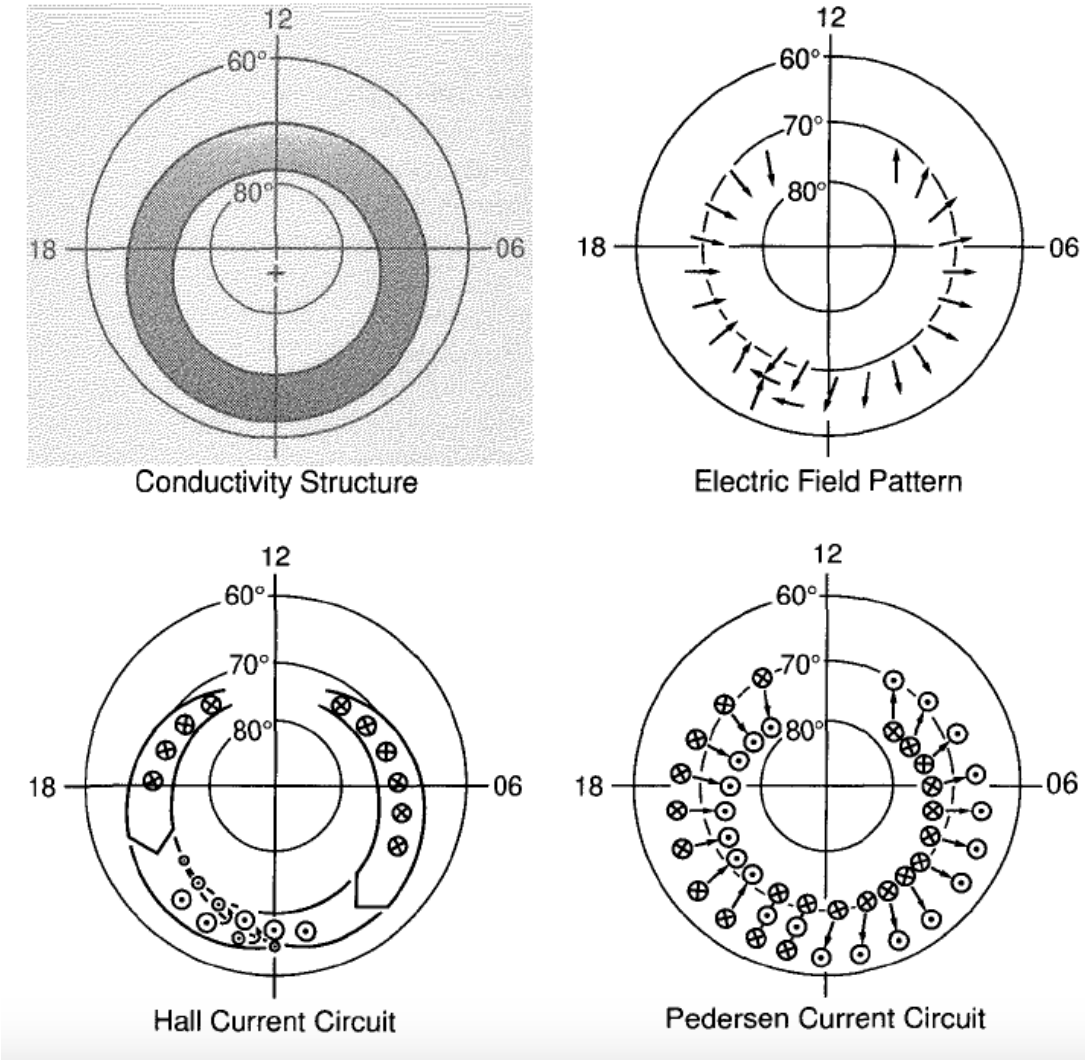

FIGURE 2.4: Magnetic local time (MLT)/latitude plots of the polar cap, showing maps of the ionospheric conductivity with darker shades representing greater charge transport (top left), the direction of electric fields within the auroral oval (top right) and the Hall and Pedersen currents that form the ionospheric current systems (bottom panels). The crosses and dots represent field-aligned currents in the direction towards and away from the page, respectively. After Baumjohann and Treumann (2012).

substorm-associated electron populations (Liou, 2002; Juusola et al., 2011). This combination of observations has allowed us to determine characteristic times of substorm events, in turn allowing examination of other phenomena during the event timeline (Haiducek et al., 2020).

2.5 Magnetospheric Currents

In circumstances in which the motion of electrons and protons in the magnetospheric plasma are opposed, currents that not only dictate the flow of plasma but also disturb the original geomagnetic field are formed. On the largest scale, the reflection of ions

and electrons and their opposed direction creates a surface current on the nose of the magnetopause, and the magnetic field structure in the lobes of the magnetotail create a current circuit between the outer magnetosphere and the plasma sheet far away on the nightside. The two-cell convection pattern of the Dungey cycle sees plasma transported along the contours of electric potential and creates currents in the highly conductive ionosphere; the increased collision rate within the ionosphere as energetic plasma is injected produces a non-zero component to the conductivity tensor in directions orthogonal to the magnetic field at the poles. Hall and Pedersen currents flow as ionizing collisions between neutrals and the charged plasma constituents occur in the ionosphere at high latitudes. These generate various current configurations on a global scale and are integral to the transport of energy, charge, mass and momentum within the MI coupling system. The high conductivity of the high latitude ionosphere thus produces an environment for closure of magnetospheric currents that allow inferences of the state of the outer magnetosphere to be made from ionospheric observations. Figure 2.4 shows a polar view of the ionosphere and displays the various current systems schematically. The top left image shows the general conductivity of the ionosphere, with darker shades representing a higher conductivity. This indicates the typical location of field lines along which electrons and protons precipitate into the ionosphere, and denotes the strongest ionospheric current flow; these currents follow the convection patterns of flux tubes discussed in section 2.3. This section describes the current configurations, particularly those that are most relevant to the aforementioned substorm phenomenon and the generation of AKR.

2.5.1 Field-Aligned Currents

The Hall and Pedersen currents that result from the partially non-ionised state of the ionospheric plasma are fed by currents that are aligned with the magnetic field. These field-aligned currents have the strongest conductivity and not only deliver energy to the ionosphere but serve to close the current loops between the ionosphere and the outer magnetosphere (Baumjohann and Treumann, 2012). As shown in the bottom left and right panels of Figure 2.4, both the Hall and Pedersen currents flow transversely to the magnetic field in the ionosphere as well as to each other. Due to current continuity these flows must be closed, which occurs via field-aligned currents that map to different parts of the outer magnetosphere. These are known as the region 1 and 2 field-aligned currents, that enter and exit the ionosphere towards the poleward and equatorward sides of the auroral oval. These extend into the magnetosphere, joining the neutral current sheet in the far magnetotail as well as the ring current. The field-aligned currents also close the auroral electrojets; ionospheric current structures that flow from the dayside to the nightside of the poles and are the subject of the following section 2.5.2. As the field-aligned currents connect those in the ionosphere with those in the the outer magnetosphere, they facilitate precipitation of the

magnetospheric plasma into the upper atmosphere during times of disturbance and form the base structure through which the most energetic displays of optical and UV aurora are observed (Sergeev et al., 1996; Coxon et al., 2014; Forsyth et al., 2018).

2.5.2 Auroral Electrojets

The auroral electrojets are shown by the Hall current circuit in the bottom left panel of Figure 2.4. Originating on the dayside they flow Eastward on the duskside and Westward on the dawnside of the Earth, and are fed by the two-cell convection pattern and the increased plasma population following magnetopause reconnection. Closed with downward (upward) field-aligned currents on the dayside (nightside), the typical structure of the auroral electrojets are idealised as is the steady-state convection pattern as discussed in section 2.3. Under disturbed conditions, such as when the magnetotail is loaded with magnetic flux during periods of Southward IMF, the release of stored potential can severely disrupt preexisting current systems, such as in the case of the substorm current wedge (discussed in section 2.5.3).

The strengthening of these current systems can be measured via ground magnetometers as mentioned in section 2.4; the presence of an Eastward or Westward current flow in the ionosphere can be measured by an enhancement or decrease, respectively, of the Northward component of the geomagnetic field due to the magnetic field that they themselves induce. Historically, a network of 12 high latitude magnetic observatories in the Northern hemisphere were used to characterise these current systems via the deviations to the geomagnetic field. This was done via the auroral electrojet (AE) index (Davis and Sugiura, 1966; World Data Center for Geomagnetism Kyoto et al., 2015), which is formed via a combination of the maximum positive and negative envelopes of the signatures measured throughout the network. In this way, the strength of both the Westward (with the minimum envelope, known as the AL index) and Eastward (with the maximum envelope, AU index) electrojets can also be measured independently. More recently, the SuperMAG network of magnetometers (Gjerloev, 2012) includes hundreds of magnetometers with much improved spatial coverage to produce a near continuous set of observations of the auroral electrojets. The SuperMAG network has an analogous index to the AE index, named the SME index (and corresponding SMU/L indices) that is vital to producing some of the lists of substorm onsets discussed in chapter 5.

2.5.3 Substorm Current Wedge

As discussed in section 2.4, the rates of dayside and nightside reconnection are seldom balanced to give the steady-state convection described by the Dungey cycle. The auroral electrojets would typically produce comparable currents in either direction in

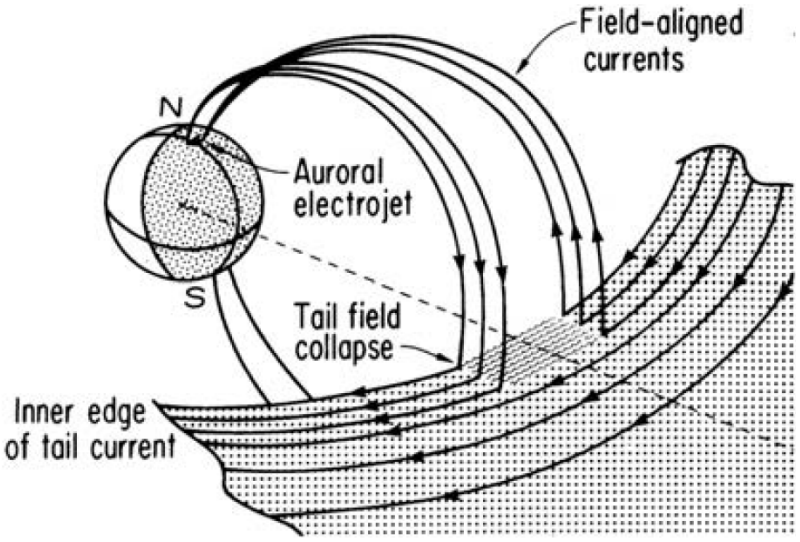

FIGURE 2.5: Diversion of cross-tail current from the magnetotail to the ionosphere during substorm expansion phase. The ionosphere closes the current system, and this portion of the current diversion forms the substorm electrojet. From Clauer and McPherron (1974)

this circumstance. Under the disturbed magnetospheric state that precedes the expansion phase onset of a substorm, significant perturbations are introduced to this current system. With the dipolarisation in the magnetotail as energetic plasma travels towards Earth, some of the dawn-dusk, cross-tail neutral sheet current is diverted into the ionosphere. This temporary current loop is known as the substorm current wedge, and is shown schematically in Figure 2.5. The ionospheric portion of this current is known as the substorm electrojet, and manifests at near midnight magnetic local times (MLTs); this current transport produces a much stronger current in the westward direction, perturbing the typical auroral electrojet signature and producing easily observable signatures in the most extreme cases, as dicussed in section 2.4. Although there are significant open questions regarding the exact sequence of events that lead to this current diversion, as mentioned in section 2.4, it is during this phase of the substorm that the largest amount of energy and plasma arrives at the ionosphere via the high latitude magnetic field lines, which includes the auroral acceleration region.

2.6 Auroral Acceleration Region

The dynamic plasma that enters the ionosphere from the much colder, more tenuous plasma of the magnetosphere follows the conversion of electromagnetic energy in the plasma to the kinetic energy of particles, namely electrons. As we have seen, the high latitude magnetic field lines and the associated currents are integral to this process (see section 2.5.1). This region, bounded by the ionosphere and the magnetosphere, in which the acceleration of charged particles occurs is known as the auroral acceleration

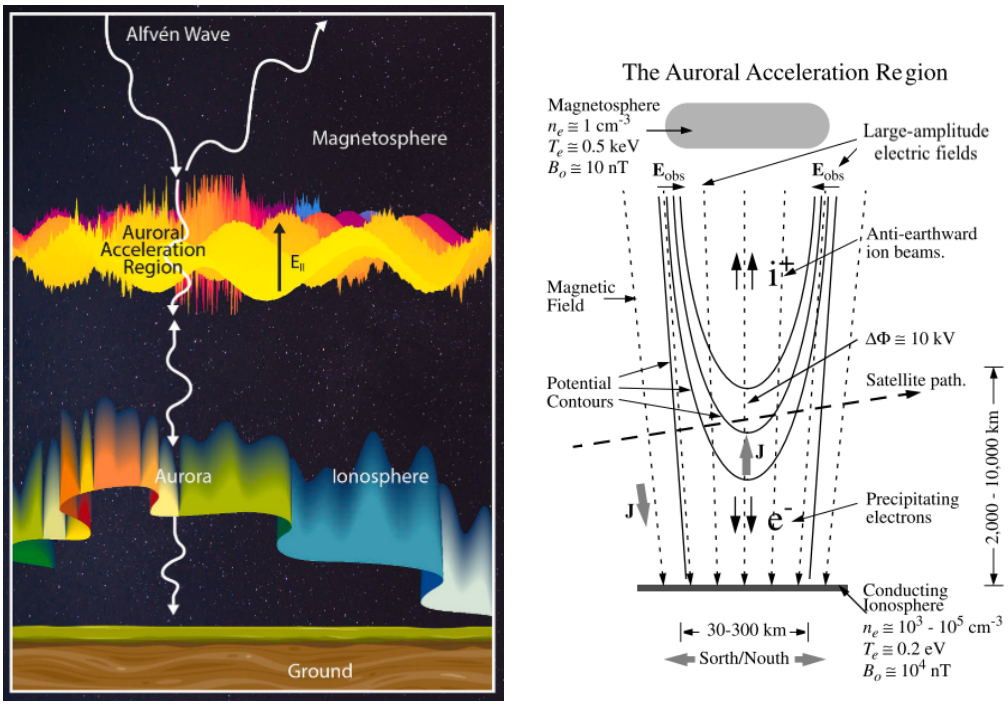

(A) (B)

FIGURE 2.6: A) Illustration of the auroral acceleration region between the magnetosphere and ionosphere; large-scale MHD Alfvén waves from the outer magnetosphere are converted to smaller-scale kinetic Alfvén waves and accompany parallel electric fields, accelerating electrons to mildly relativistic speeds. Adapted from Keiling (2021). B) Schematic diagram of the main electromagnetic components of the auroral acceleration region in the presence of parallel electric fields and an electric double layer (see section 1.4.3), where electric potential contours deviate from the field-aligned direction. From Ergun et al. (2000).

region (AAR) and extends to about 5 R_E; the predominant region of acceleration is thought to exist between 1.5 R_E to 3.5 R_E (Keiling, 2021). In this region Alfvén waves, a form of magnetohydrodynamic wave that propagates along magnetic field lines, are converted from a large spatial and temporal scale phenomenon to a much smaller scale wave that acts on the particles in a kinetic or inertial fashion, and generate a parallel electric field (Mottez, 2014; Keiling, 2021). Electric potential structures such as double layers can also exist with parallel electric fields in the auroral zone, as discussed in section 1.4.3. Both cases produce mildly relativistic electrons in the beam but, in the latter case, large plasma density cavities are also created (Ergun et al., 2000; Song and Lysak, 2006). The AAR is a critical domain in determining the energy input to the ionosphere. Figure 2.6a shows an illustration of the AAR in the context of the magnetosphere and ionosphere, with the upward-directed parallel electric field ($E_{||}$) shown amongst the schematic representation of the short wavelength Alfvén wave structures. Figure 2.6b shows a more complex schematic of quasi-static double layers in the AAR, with the magnetic field and electric potential structures visible. The altitude range of 2000-10000 km on the bottom right of the figure is relative to the level of disturbance in the coupled magnetosphere-ionosphere region which is roughly

analogous to the AAR; the altitudinal extent can be studied by proxy using remote observations of terrestrial radio emissions, discussed in the following section 2.7, and forms the basis of the inference of results presented in chapter 5.

2.7 Auroral Kilometric Radiation

Since the early 1970s, electromagnetic radiation corresponding to wavelengths of a few to tens of kilometres has been observed to be emitted with the Earth as its source. Gurnett (1974) made the first detailed observation of the Auroral Kilometric Radiation (AKR) using radio data collected from the Imp 6 and Imp 8 satellites. Emissions were detected in a frequency range of 50kHz $\leq f \leq$ 500kHz with a total power output of 10^9W at peak intensity. The distribution of the emission regions was also reported; AKR events were found favourably in the local evening sector. In a later study, AKR source regions were derived using the Explorer 2 satellite, as lunar occultations of the Earth were observed (Alexander and Kaiser, 1976). Although they observed some emission in the region of the dayside cusp, nightside observations centred near 22 hours LT and confined to a geomagnetic latitudinal region of $70 - 80^\circ$ were typical.

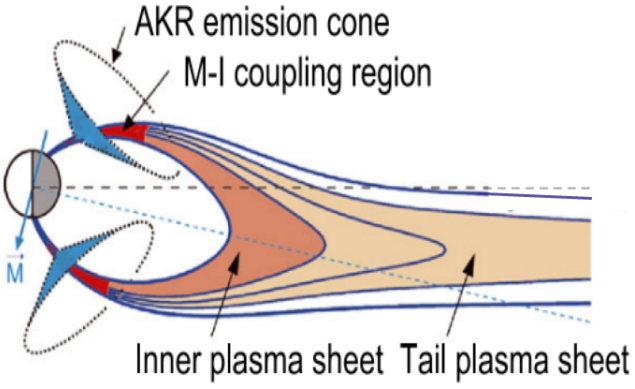

FIGURE 2.7: Schematic of the nightside magnetosphere, showing the magnetotail, plasma sheet, and the magnetosphere-ionosphere coupling region, as well as the conical beams of AKR from example source locations in each hemisphere. Adapted from Morioka et al. (2013).

Further preliminary observations of the emission altitude found that lower-frequency AKR is more likely to have been observed from a source region at a higher altitude. Constraining the geometrical properties of the AKR, Green et al. (1977) studied the angular distribution of the emission. This confirmed the upward-beamed direction of the emission using the Hawkeye 1, Imp 6 and Imp 8 satellites, finding that the emission illuminates a conically-shaped region of decreasing solid angle with decreasing radiation frequency. Figure 2.7 shows a schematic of the magnetotail, extending from high latitude, converging magnetic field lines (magnetosphere-ionosphere (MI) coupling region) into the non-dipolar plasma sheet.

The approximately conical region of space into which AKR is beamed are shown; with multiple AKR source regions at various altitudes and longitudes, it is typical for a remote sensing spacecraft to be illuminated at large distances. As well as the geometrical effects, the polarisation of the emission was found to be exclusively right-handed or left-handed circularly polarised, with this being dependent on the hemisphere of origin of the emission and ultimately related to the gyration of electrons on magnetic field lines at either pole. With these observational constraints, Wu and Lee (1979) postulated an emission mechanism that is known as the electron cyclotron maser instability, whereby energetic electrons are trapped within a low-density cavity and resonate with interior electromagnetic waves. This and other important features of AKR are described in the following chapters.

2.7.1 Generation and Source Region Distribution

The cyclotron maser instability (CMI) is a wave-particle instability which has a resonance condition when the Doppler-shifted angular frequency of the wave (in the frame of the electron) is equal to the relativistic gyration frequency of resonant electrons (Wu, 1985). This dictates that emission is generated very close (typically within 1-2%) to the electron gyrofrequency, which increases with magnetic field strength as converging field lines reach the auroral zone. *In-situ* observations of the AKR source region showed a shell-like distribution function (Ergun et al., 1998). This electron population arises from the fact that they are accelerated along the magnetic field lines, filling the ”shell” within phase space as they gyrate downward, and then lost to the ionosphere in energetic cases where particles are in the loss-cone. The combination of the loss-cone and shell distribution functions creates what is known as a ”horseshoe” distribution; by consequence the emission is initially emitted from the source at directions perpendicular to the magnetic field (Treumann, 2006). The resonance condition of CMI, and its representation in velocity space, is such that only wave modes perpendicular to the magnetic field can be amplified, and not parallel wave modes. This leaves the extraordinary and ordinary wave modes as possible, but only the extraordinary mode is able to be amplified sufficiently as it is trapped by the increasing plasma frequency outside the cavity, where the density is higher (Wu and Lee, 1979). This is due to the depletion of low energy electrons by the parallel electric field, and the subsequent shell-like distribution of the horseshoe, with no electrons present at the origin of velocity space, where the CMI resonance circle is centered for AKR (Treumann, 2006). The existence of the auroral plasma cavity is necessary for the generaton of AKR in this way as it modifies the distribution function, as well as amplifying the wave mode as it is trapped.

The auroral acceleration region between the magnetic mirror point and the upward-directed parallel electric field was found to contain the source of the AKR and

further constrains the altitude of the emission region, given observed AKR data, to be roughly between 2000 km and 9000 km (Lee et al., 1980). The ideas presented in the aforementioned studies were supported by observations made by Calvert (1981) who found that a cavity of low plasma density ($\leq 1\text{cm}^{-3}$), extending from altitudes of $\sim$ 5000 km to 13000 km, occurs at an invariant geomagnetic latitude of 70° during AKR emission. Ergun et al. (1998) used in-situ data, from the FAST satellite, of the coupling region along field lines at high magnetic latitudes, observing strong parallel electric fields. They summarise that the electric fields accelerate downward-going electrons to up to 10^4 times their thermal energy, and showed that the strong quasi-static electric fields necessary for AKR generation exist. Indeed, these strong, parallel electric fields generate the sparsely populated region of plasma above the auroral zone that dictates the energy conversion for AKR in the terrestrial case (Ergun et al., 2000). The horseshoe distribution function that is responsible for the AKR generation at Earth provides quasi-continuous conditions, given the parallel electric field, to produce strong, persistent emission over time; while there is fine temporal structure that is yet to be fully explored, long periods of AKR on the order of hours are often observed.

The CMI and generation of AKR, reliant on mildly relativistic electrons, correlates with other activity in the auroral oval; namely ionospheric auroral emission, with active AKR source regions existing above brightenings in the auroral oval, typically in premidnight local time (LT) sectors (Huff et al., 1988; Panchenko, 2003; Mutel et al., 2004; Schreiber et al., 2017). While the strongest emission and the greatest occurrence of emission is close to midnight, AKR sources have been observed in the afternoon sectors (Mutel et al., 2003, 2004) and analysis of the average source region distribution produced an extended region covering the dusk sector (Green, 2004). From the close relationship to the electron gyrofrequency, the activation of a lower frequency AKR source implies that the source region has extended to higher altitudes along the field line, and so can provide a proxy for the structure of the auroral acceleration region (Ergun et al., 1998; Morioka et al., 2012).

2.7.2 Factors Effecting the AKR Intensity

Various influences can affect the intensity of AKR observations, which can occur at both the scale of the CMI iteself or on a larger scale due to the remote observation of a wide distribution of single AKR sources. For the CMI itself, the growth rate, or the rate of amplification of the wave, affects the intensity directly. If the growth rate is too low, the wave will not be amplified sufficiently. The growth rate is directly related to the distribution function and the resonance condition of the CMI; at Earth, the free perpendicular energy of electrons as they gyrate and contribute to the shell distribution function of the horseshoe as discussed in section 2.7.1, satisfying the resonance condition and increasing the growth rate (Treumann, 2006). Emission

saturation at the CMI source could also affect the intensity. While various saturation methods are described, it is unclear at present which are applicable to AKR at Earth. Quasilinear saturation in particular relates to the trapping of waves and could affect the AKR intensity; for a larger source the intensity is expected to be more intense. Whether, or how exactly this applies to the AKR generation at Earth is in question, however (Le Quéau and Roux, 1987).

As the energetic electrons that reach Earth via high latitude magnetic field lines and the auroral acceleration region create the conditions for AKR generation, it is natural to question the effect that they have on the intensity directly. While accelerated auroral electrons themselves are not the source population for the CMI, an increase in precipitating energy is likely to increase the growth rate of an AKR source as the electrons will increase the free energy available, as well as carrying the current that sustains the parallel electric field. In the case of an increase in precipitating electron flux, however, the growth rate of the CMI could be reduced if the parallel electric field is not sustained and the electrons fill the auroral plasma cavity; the exact relationship between the energy and flux of precipitating electrons and the intensity of AKR sources is still uncertain.

For remote observations made by an instrument such as Wind/Waves, it is likely that many different elementary AKR sources will be observed simultaneously. The AKR intensity observed by Wind for example, could be due to the increase in intensity of a single source, but is more likely due to the expansion of the auroral plasma cavity and the subsequent increase in spatial distribution of AKR sources and their accompanying growth rates. As well as this, the observed AKR intensity is greatly affected by the position of the spacecraft, due to both the predominant localisation of the plasma cavity and AKR sources on the nightside and the anisotropic beaming pattern that is described in section 2.7.3.

2.7.3 Observed Beaming Pattern

The generation mechanism and the plasma environment in which the AKR is produced has important consequences to consider for remote observations of AKR. In particular, the generation of emission in the extraordinary mode, with propagation initially perpendicular to the magnetic field, then sees refraction occurring at the much higher density walls of the cavity; a distinction must be made between the initial, CMI-induced beaming and the final beaming pattern once this propagation has occurred. This process is illustrated in figure 2.8. The emission is converted to the right-extraordinary mode which has propagation blocked both below the source region due to the increasing magnetic field, and at the walls of the cavity due to the increased density. The density structures at the walls of the cavity, which are generally inhomogenous, scatter the emission to an upward (relative to the planetary surface)

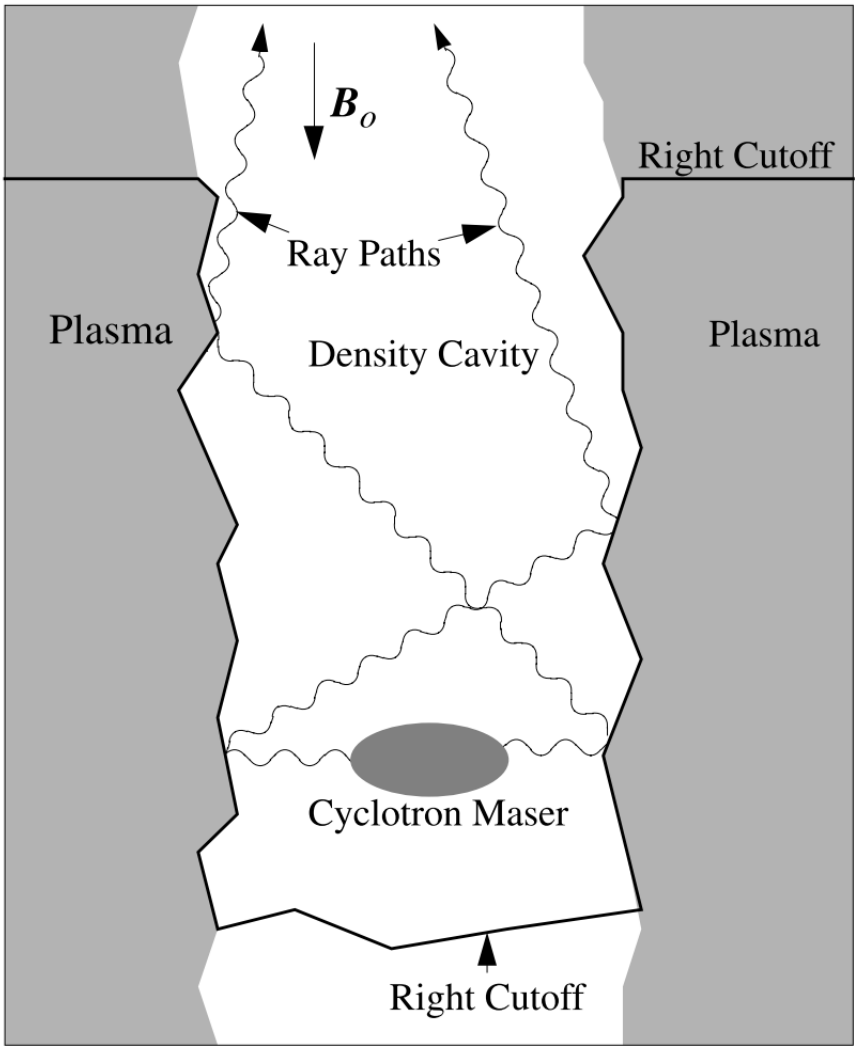

FIGURE 2.8: Schematic showing the plasma density cavity that guides the propagation of AKR rays from the source region within the parallel electric field of the auroral acceleration region. From Ergun et al. (2000).

propagation direction. Upon reaching a weaker magnetic field after further scattering within the cavity, the emission escapes into the surrounding plasma and subsequently into space (Ergun et al., 2000).

Figure 2.9 shows a schematic of the ultimate beaming pattern which, globally, produces the typical AKR observations for a remote observer (Mutel et al., 2008). The figure shows a single magnetic field line in black, with a red cross indicating the position of an AKR source. The orthogonal axes in yellow represent a coordinate system such that the x-direction is tangential to the magnetic field at the position of the source, the z-direction is aligned Northward, and the y-direction follows a line of constant magnetic latitude and completes the orthogonal set. The green lines represent the ultimate beaming of the emission from the single source after the initial rays, perpendicular to the magnetic field, are scattered to be relatively closely aligned

with the magnetic field. While previous beaming models envisaged a conical beaming structure, the more recent models constrain the latitudinal opening angle of the beaming structure, as shown by the shorter extension of the emission in the z-direction in Figure 2.9. The blue structure represents the plasma cavity, here extended in the longitudinal direction again at a constant magnetic latitude. While only a single source is shown here, one can imagine the superposition of the beaming pattern of multiple AKR source regions; the latitudinal angle of the beaming varies for AKR sources at different altitudes along the field line, and AKR sources can exist along a wide longitudinal range of magnetic field lines. Generally, the emission is beamed outwards from the planet but is constrained to illuminate only a certain region of space; a remote radio observer at a given position will only record a fraction of the active AKR source regions in the auroral acceleration region.

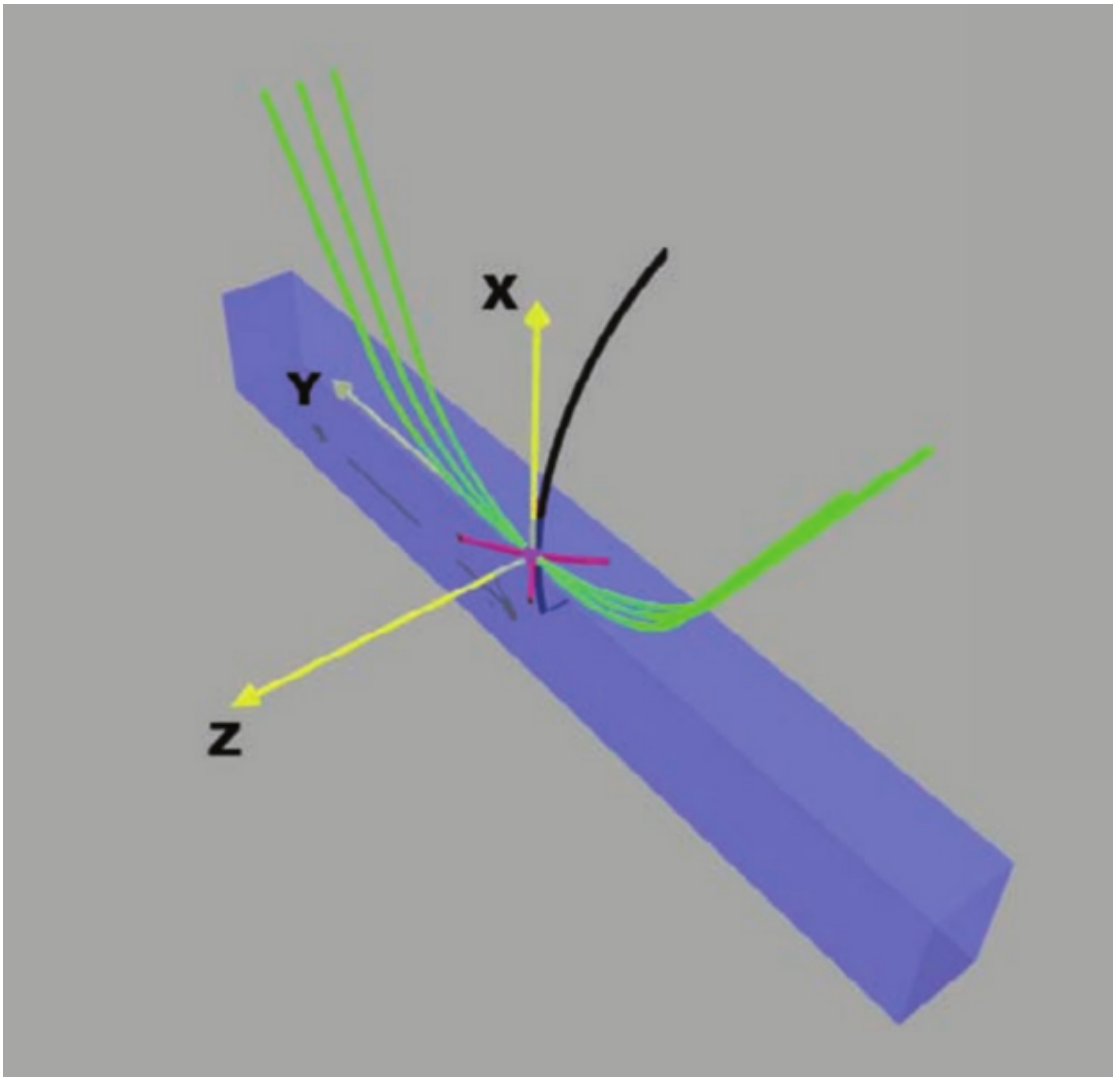

FIGURE 2.9: Tangent plane beaming model of AKR propagation from the source. The green lines represent the AKR ray paths, emitted from a source region represented by the red cross. The black line represents a high-latitude magnetic field line: the coordinate system (yellow arrows) is such that the x-direction is tangent to the local magnetic field line, the z-direction is towards the pole, and the y-direction completes the orthogonal set. From Mutel et al. (2008)

Chapter 3

Instrumentation

3.1 Wind

3.1.1 Introduction

The Wind spacecraft, launched in 1994 as part of the International Solar Terrestrial Physics (ISTP) mission, is equipped with various instruments designed to study the solar wind and radio emissions from both the Sun and Earth. The primary function of the spacecraft is that of a solar wind monitor, and Wind has most often observed from the Lagrangian point L1 (sunward of Earth); Wind first reached L1 in 1996 before spending time between 1998 and 2004 executing complex orbital manoeuvres to explore Earth's magnetosphere. The trajectory of Wind between ∼1995-2004 is shown in Figure 3.1b. The spacecraft returned to L1 in 2004 and has been there since.

3.1.2 Waves Instrument

The Waves investigation (Bougeret et al., 1995) is comprised of two antennae in the spin-plane of the spacecraft (X and Y - with original tip-to-tip lengths of 100 m and 15 m, respectively) as well as one aligned with the spin-axis (Z, of length 12 m tip-to-tip). The antennae used here are of the electric dipole type, each formed of two monopolar wire lengths along the same axis on either side of the spacecraft, with the Z antenna having a rigid structure. Of the three Waves radio receivers RAD1 operates between 20-1040 kHz, covering the whole AKR frequency spectrum, and utilises antennae that are each in the short-antenna regime, allowing for a beaming pattern that is independent of the observation frequency. The orthogonal antennae in the context of the spacecraft and the component electronics of Waves can be seen in Figure 3.1a. This section includes a description of the Waves instrument and the RAD1 receiver of interest in this thesis, as well as a description of the radio background

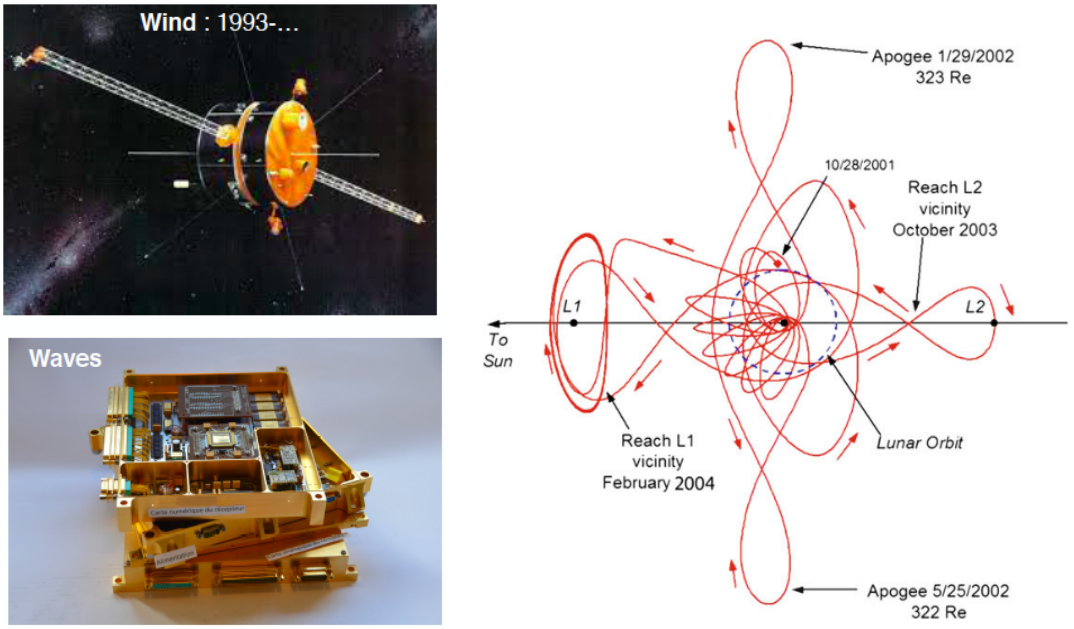

(A) (B)

FIGURE 3.1: A) Illustrative schematic of Wind (top) with photograph of the on-board electronic systems relevant to the Waves instrument (bottom). B) Wind's trajectory from October 2001 to February 2004, during which time the spacecraft travelled through a wide range of the magnetosphere and surrounding space with complex orbital dynamics. The trajectory here is projected into the ecliptic plane (Pelton and Allahdadi, 2015).

determination and calibration process applied to the raw Wind/Waves data. Developed solely for the purpose of AKR observations, the following techniques are used in chapters 4, 5 and 6.

The RAD1 receiver can operate in one of two modes: the SEP mode allows the receiver to measure with one of the equatorial antennae (usually X) and the Z antenna independently. The SUM mode performs the electronic summation of the X and Z antennae, outputting this synthetic signal as well as one with a $\frac{\pi}{2}$ phase shift applied to the equatorial antenna. The SUM mode thus returns two signals from the synthetic inclined dipole. In this work the original SUM signal will be referred to as the S antenna and that with a phase-shift applied as the S' antenna. RAD1 has 256 available frequency channels between 20-1040 kHz and channels can be chosen to sample the radio environment via three different methods. The most often used allows the instrument to be provided with a list of frequencies to be measured over the next fixed-duration sweep cycle of samples.

Each frequency channel is measured at each antenna over the respective integration time (154 ms for the S and S' antennae and 308 ms for the Z antenna) to comprise a single observation. Measurements are then repeated at that frequency across a spacecraft spin period of 3 s in order to receive a signal that corresponds to a single period of modulation. Sampling all 256 frequency channels, while offering greater

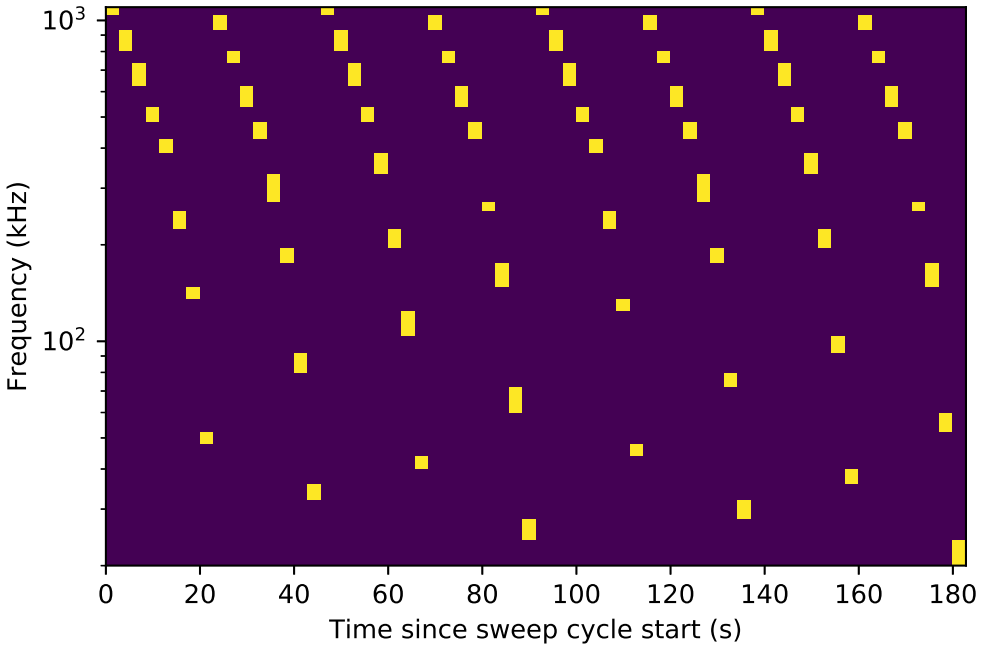

FIGURE 3.2: Schematic example of a ∼3 minute sweep cycle of the RAD1 receiver aboard Wind/Waves. Each highlighted bin represents a single rotation of Wind, with a spin period of 3 s, that comprises eight samples at the corresponding frequency channel for each of the S, S′ and Z antennae.

spectral resolution, would increase the duration of the sweep cycle and so decrease the temporal resolution. The typical total time attributed to the measurement of a single frequency for S, S′ and Z antennae, accounting for the offset incurred at the beginning of the frequency sample, is 358 ms. A sweep cycle, lasting ∼3 minutes, is typically comprised of 64 frequency measurements, each made during one spacecraft spin period. Thus a total of 8×64 voltage spectral density measurements received by each of the S, S′ and Z antennae, as well as the corresponding times of measurement, are supplied for a single sweep cycle. Each measurement is provided in units of $\mu V^2 Hz^{-1}$ and the preamplifier and receiver gain values have been taken into account. As well as this, general data including spacecraft attitude parameters and indicators for the mode of operation of the RAD1 receiver are supplied with each sweep cycle. L2-level data for the RAD1 instrument are provided as $\leq 480 \times 3$ minute sweep cycles that comprise 24 hours of RAD1 observations.

3.1.3 Radio Background

The frequency range of the RAD1 receiver is such that background radio emission is present due to both the local plasma environment and non-thermal emission from the galactic center or disk. At lower frequencies (below $\sim$ 300 kHz) the thermal motion of

charged particles in the plasma surrounding the spacecraft creates quasi-thermal noise (QTN) (Meyer-Vernet and Perche, 1989) while emission from the galaxy dominates at higher frequencies (Novaco and Brown, 1978; Cane, 1979). Previous examination of measurements across the entire Waves frequency range has consolidated the measured galactic spectrum with previously derived functional forms (Dulk et al., 2001) and more recent measurements across the RAD1 receiver show agreement with a spectrum that falls off between 100-200 kHz (Hillan et al., 2010).

Hillan et al. (2010) produced a complete background spectrum, combining models of both the galactic background and a two-component model of the QTN that defines the signal above and below the plasma frequency. As well as these sources of emission, instrumental noise is also present due to the electronics of the antenna system and the digitization of the signal and can be derived from antenna-predeployment measurements; the galactic background (taken from a quiet period above 500 kHz) is no more than double the median RAD1 receiver noise. We assume that QTN at frequencies below 100 kHz will typically dominate the background spectrum.

A similar method to that used by Zarka et al. (2004) to determine the galactic background present in the Radio and Plasma Wave Science (RPWS) instrument of the Cassini spacecraft is implemented here for all frequencies. A background spectrum is formed for every 24 hour period of RAD1 data by taking the 5% quantile at each frequency channel. Although no explicitly quiet period is selected over which to take the quantile (as opposed to the method of Zarka et al. (2004)), the definition of the quantile imposes that the remaining 95% of received signal is above this level. Although some examples of L2 data contain consistently high emission for the corresponding day at many frequencies, background spectra produced in this way agree well with other measured background levels observed by Wind, as well as producing the expected form due to the QTN and galactic background source described previously (Hillan et al., 2010). Once the background spectrum has been determined, the relevant value is subtracted from each of the eight measurements made during a spin period, implicitly assuming isotropy of the background source. If values are negative (and therefore unphysical), following background subtraction, the background value at the given frequency is stored instead.

3.1.4 Calibration for AKR Flux Density

To relate the received power of the Waves instrument to the AKR flux density, we consider the goniopolarimetric (GP) technique developed by Manning and Fainberg (1980). GP techniques allow for radio source parameters to be determined by inverse modelling the observations to the radio source parameters using the antenna reference frame and a model of the emission geometry. In their work, spin measurements from a synthetic inclined dipole (here fulfilled by the Waves S antenna) and a phase-shifted

inclined dipole (S') antenna are demodulated and combined with a spin-axis-aligned (Z) antenna to derive the Stokes parameters (flux density and the degrees of linear and circular polarisation), angular coordinates and the angular radius of the source, so describing the state of a partially-polarised extended source. To derive these parameters, it is assumed that a single radio source is observed by the instrument and that the source parameters are constant as the spacecraft completes a spin such that the modulation pattern can be inverted. For AKR this assumption is often broken; either the intensity of the source is variable on timescales shorter than that of the spin, or the spacecraft is observing emission from multiple sources in each measurement as it changes position during a spin, or a combination of the two (see section 4.1.1). It is not possible to use the combination of the Waves antennae in this case as the exact variability over the modulation pattern cannot be determined analytically without *a priori* knowledge of the source parameters. However, the spin-axis-aligned Z antenna can be used to determine the source flux density after modifications are made to the original GP inversion. We assume that, for an AKR observation, the radio source is a point source and there is no linear polarisation. We also assume that the AKR will be circularly polarised, but the received Z antenna power is independent of the source circular polarisation using the inversion of Manning and Fainberg (1980). Following from equation 21 in Manning and Fainberg (1980), this gives

$$P_Z = \frac{1}{2} G S_Z \sin^2 \theta \tag{3.1}$$

where P_Z is the power measured by the Z antenna in V^2Hz^{-1}, G is a calibration factor, S_Z is the flux of a point source derived from the single Z antenna in $Wm^{-2}Hz^{-1}$ and θ is the co-latitude of the radio source. For AKR, we can assume that the source region is approximated by the Earth's center and transform the source co-latitude θ to λ, the latitude of the spacecraft in geocentric-solar-ecliptic (GSE) coordinates. Given that this calibration is designed to be applied to all Wind observations, which are made from various latitudes and LT, and that the exact emission hemisphere cannot be determined, this assumption is the most broadly valid; errors in the spatial location of the source when assuming emission from either pole could be up to 1 R_E given the spectral range of the instrument, the azimuthal extent of AKR sources relative to Wind and their confinement along high latitude magnetic field lines. An implicit error due to assuming the Earth's center as the source location instead of the geographic poles was accounted for; the maximum error implicit for the period in question in chapter 4 is 1.2%. Details of this statistical error analysis are given in section 4.4. This modification gives

$$P_Z = \frac{1}{2} G S_Z \cos^2 \lambda \tag{3.2}$$

as the received signal of the Z antenna, oriented normal to the ecliptic plane, is minimised when the spacecraft is above the poles. This then gives the flux density S_Z for each of the eight spin measurements, which are then averaged using the mean.

The synthetically-inclined S (and phase-shifted S') antenna is longer and more sensitive than the Z antenna, making its measurements prone to spurious signals at all frequencies as receiver electronics are saturated. This is often the case when Wind observes the highly intense AKR. This contamination does not occur with the shorter, less sensitive Z antenna. While the Z antenna is less prone to saturation, its lower sensitivity means that previous methods of calibration with Wind/Waves cannot be used. These have employed measurements of the galactic background to determine a value of the instrument gain, using a model of the galactic emission to infer the observed flux during a quiet period and then equate this to measurements (Zarka et al., 2004; Zaslavsky et al., 2011). The shorter Z antenna typically measures the galactic background to be within 10 dB of the instrumental noise, as given by the received power prior to antenna deployment, so the contribution from the galactic signal cannot be determined. For this reason, the initial measurements of the instrumental characteristics are used to determine the gain using

$$G = (\frac{C_a}{C_a + C_s})^2 L_{eff}^2 Z_0 \tag{3.3}$$

where $Z_0 \sim 120\pi$ is the impedance of free space, $C_a = 30$ pF and $C_s = 45$ pF are the antenna and stray capacitances, respectively, and L_{eff} is the effective length of the antenna. Here we use the physical length ($L_p = 4.65$ m) of each monopole of the Z antenna, given that both electrical monopoles that comprise the Z antenna are in the short-dipole regime, so that $L_{eff} = L_p$.

To check the validity of using calibrated measurements from a linear antenna as proxy for the true flux of a radio source (here AKR), observations of solar radio Type III bursts from Wind and Cassini were compared. A modified calibration routine was prepared and applied to the linear Z antenna for these observations. Flux density values of Type III bursts derived using the above were compared with independent values produced by a direction-finding inversion, derived from the same initial method presented by Manning and Fainberg (1980) but bespoke to solar Type III burst observations with Wind, giving the flux density, angular coordinates and angular extent of the source with only the S and Z antennae. Initially, these independent measurements served as a scaling factor to be applied to S_Z from Equation 3.2, using an average spectrum of peak fluxes across a set of Type III bursts. After discussion during the review process it became clear that this scaling factor is only relevant for Type III bursts, but not for AKR, since it essentially corrects for the size of an extended radio source. AKR can be considered as coming from a point-source when observed at large radial distances, which is why we present S_Z as an accurate (within instrumental uncertainties in the terms of equation 3.3) measure of the AKR flux. Section 4.5 gives explicit details of this former processing step and is retained for the interest of the reader.

3.2 Ground Magnetometer Networks

Magnetometers are relatively simple instruments that are cheap to build and maintain, but can provide valuable insight into the behaviour of the terrestrial system at large. When used on the ground they can measure changes to the geomagnetic field, which is of particular use during the intensification of ionospheric current systems that are large enough to cause significant perturbations. Given the known characteristics of such systems, including the auroral electrojets, their signatures can be observed in magnetometer readings, subsequently providing temporal and spatial information of ionospheric electrodynamics. With a greater coverage of ground magnetometers the spatial sampling is improved and, as the Earth rotates while the electrodynamics are fixed in the frame of the magnetic field, these signatures are tracked over hours and better characterised. As discussed in section 2.5.2, the AE indices are commonly used in the literature (e.g. Juusola et al., 2011; Davey et al., 2012; Borovsky, 2014; Walach and Grocott, 2019) and are formed via the combination of 10-13 selected ground magnetometers in the high latitude auroral zone. As the Eastward or Westward auroral electrojets intensify, they invoke a magnetic field that either opposes or strengthens the horizontal, Northward geomagnetic field component. By measuring the smallest and largest perturbations of the included stations, as well as combining them, the average current dynamics are captured. With the extension of ground magnetometers over a greater spatial domain, the sampling has been increased and data from a global network of magnetometers is now combined to produce the SuperMAG indices, with accompanying analogues to the aforementioned indices in the SME indices (Gjerloev, 2012). Figure 3.3 shows the locations of ground magnetometer stations in the Northern hemisphere, and highlights those used by the older AE indices and those in the updated SME indices. Substorm lists derived from the SuperMAG network of magnetometers are used in chapter 5 to explore the average AKR response over 10 years of events during the event timeline, while the SMU and SML indices themselves are used in chapter 6 to give an insight into magnetospheric dynamics.

3.3 OMNI

OMNI is a data product derived from a combination of spacecraft including ACE, Wind, IMP 8 and Geotail; the majority of which have science objectives that place them in the upstream solar wind. These spacecraft each monitor important solar wind parameters for coupling to the terrestrial magnetosphere, such as the density of electrons and protons, the IMF and its separate components, and the solar wind speed. To provide standardised measurements and a valuable insight to the timing of the magnetosperic response to solar forcing, the observations are shifted as if they

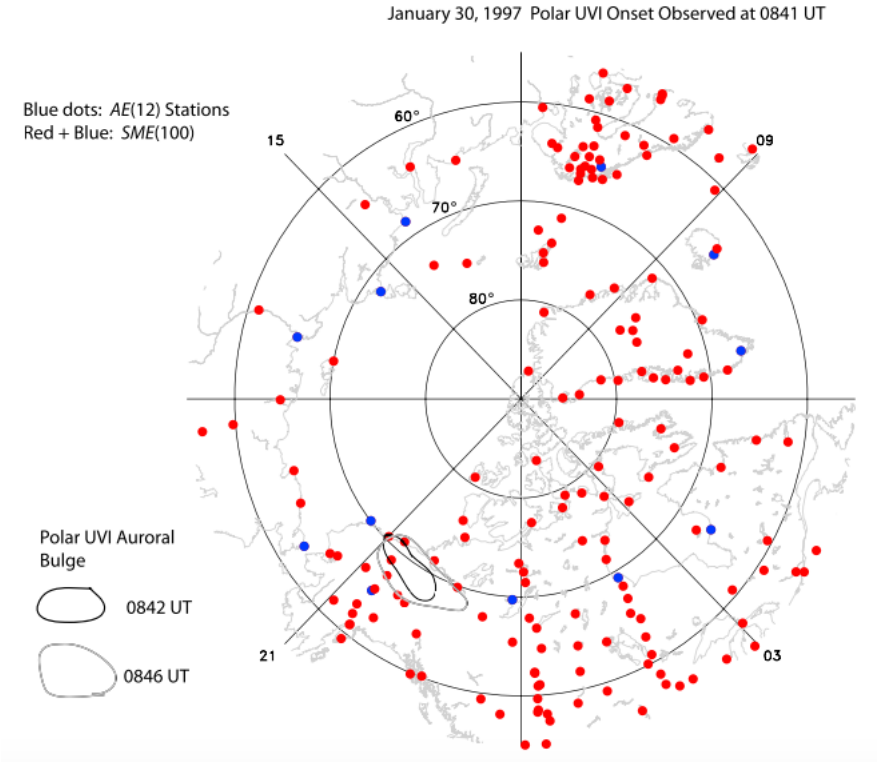

FIGURE 3.3: Illustration of the coverage of ground magnetometer networks in the Northern Hemisphere, showing both the 11 stations used in the AL index (blue dots) and the 100 stations used in the SuperMAG SML index (red dots), for a single substorm onset (from (Newell and Gjerloev, 2011)). The authors note that, for this example, the location of the UV auroral bulge (a typical, visual, spatial and temporal indicator of substorm onset) has no AL stations that can sample this region, whereas the distribution of SML stations can capture this behaviour.

were made at the nose of the bow shock. For more details of the data processing involved, see `https://omniweb.gsfc.nasa.gov/html/omni_min_data.html`.

3.4 SSUSI

The SSUSI instruments are scanning spectrometers that measure the radiance of the auroral regions in UV wavelengths. They are found onboard multiple DMSP spacecraft, which fly over each pole and observe the oval during their orbits at altitudes of 830 km. Typically, the trajectories of the spacecraft are such that coverage of both hemispheres within a 40 minute window is obtained. When in the "imaging" operation mode, SSUSI scans along a track perpendicular to the spacecraft trajectory as projected on the terrestrial surface for each pass of the pole; the track is 153 km wide and measures 16 pixels at 10 km x 10 km resolution in 22 s, as well as in multiple UV wavelengths that capture both electron- and proton-auroral emission (Paxton et al., 1992). Figure 3.4 shows examples of average auroral radiances observed in each hemisphere during two orbits of DMSP, showing the auroral dynamics in the

wavelength range 140-150 nm. SSUSI observations used to produce Figure 3.4 are used in chapter 6, where they provide context to dayside AKR observations with Wind.

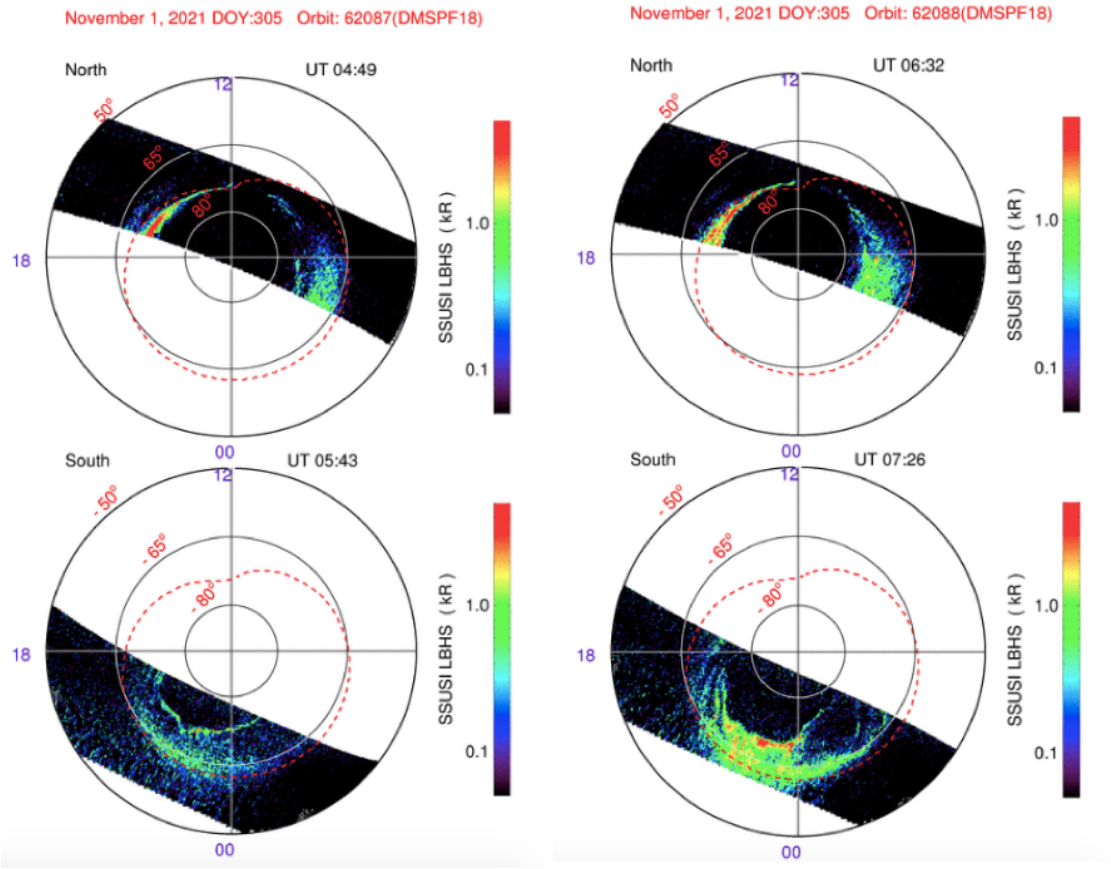

FIGURE 3.4: Summary plots for the SSUSI instruments compiled during ∼20 min passes of both Northern and Southern poles, for two orbits. Each plot is a polar projection, showing the MLT and magnetic latitude of the Northern (top) and Southern (bottom) hemispheres, with the colour bar indicating the auroral radiance of a given bin in kR between wavelengths of 140-150 nm.

Chapter 4

Empirical Selection of Auroral Kilometric Radiation

This chapter is based on results presented in the following publication: *Waters, J. E., Jackman, C. M., Lamy, L., Cecconi, B., Whiter, D. K., Bonnin, X., Issautier, K., Fogg, A. R.; Empirical Selection of Auroral Kilometric Radiation During a Multipoint Remote Observation With Wind and Cassini; JGR: Space Physics; 126(10); doi:10.1029/2021JA029425, 2021*

This work was conducted entirely by the author, although significant discussions were held with colleagues. In particular, L. Lamy, C.M. Jackman, and D.K. Whiter contributed discussion regarding scientific interpretation and analysis, while B. Cecconi, X. Bonnin and K. Issautier contributed discussion regarding calibration and treatment of Wind/WAVES, instrumental data.

4.1 Introduction

Auroral kilometric radiation (AKR) describes amplified radio emission from the Earth that is generated from relativistic, precipitating electrons along magnetic field lines in the auroral zone, and resonates at the electron cyclotron frequency (Wu and Lee, 1979). The emission frequency of an AKR source is close to the local electron gyrofrequency, so that lower frequency AKR emanates from a higher altitude along a field line. AKR is emitted between $\sim 30 - 800$ kHz and has been observed by many Earth-orbiting spacecraft such as Polar, Geotail and Cluster (e.g. Liou et al., 2000; Mutel et al., 2003; Anderson et al., 2005; Morioka et al., 2007). The emission mechanism, the electron cyclotron maser instability, is such that AKR is emitted at angles near-perpendicular to the field lines. This leads to largely anisotropic beaming of AKR from individual field lines that has been constrained both through modelling and observations. Earliest observations suggested that AKR can be observed within a

cone at angles that are increasingly oblique to the magnetic field with decreasing frequency (Green et al., 1977; Kasaba et al., 1997). However, more recent observations using Cluster suggests that AKR is emitted in a more restricted geometry, with similar longitudinal extent up to a few thousand km but emitted over a narrower latitudinal region of a few tens of degrees over the auroral zone (Mutel et al., 2008). Both models of the emission geometry have been supported by in-situ observations with the Polar spacecraft, confirming the frequency-dependent, anisotropic beaming of AKR from the source region (Menietti et al., 2011a).

Furthermore, AKR is known to be fully circularly polarised, with the handedness depending on the direction of electron gyration in either hemisphere (Kaiser et al., 1978). Where polarisation information is available, we expect to see left-handed circularly polarised (LH) emission from the Southern magnetic (Northern geographic) hemisphere and right-handed circularly polarised (RH) emission from the Northern magnetic (Southern geographic) hemisphere (assuming emission in the extraordinary mode). This has been observed at both Earth and Saturn and is a consequence of the emission mechanism (Lamy et al., 2008b, 2010). The visibility of AKR is a strong function of the position of the observer. AKR and its source regions are mostly concentrated at nightside local times; AKR has been observed consistently from local times (LTs) between ∼1600-0300 hr, whereas the most intense source regions are located at 2100-2200 LT (e.g. Gurnett, 1974; Alexander and Kaiser, 1976; Panchenko, 2003). The visibility of AKR to a spacecraft at various latitudes is constrained by the beaming of the emission, as mentioned above. Ray tracing has been used previously to examine the general propagation of AKR from the source region as well as for instances where the emission may refract; from the dense plasmasphere, for example (Green et al., 1977; Mutel et al., 2004). AKR visibility with latitude has also been examined statistically for studies of hemispheric conjugacy using multiple spacecraft (Morioka et al., 2011). For a spacecraft near the equator, it is possible to observe AKR emission from both hemispheres as the emission cones from sources on a given meridian overlap. In this case the emission from each pole cannot be separated (without polarisation information) and the observations must be interpreted as a global average. For closer radial distances a spacecraft near the equator can be beneath the superposed emission cones of each hemisphere and observe no AKR. At Saturn, this equatorial shadow zone has been modelled and found at radial distances of $< 3.6R_s$, where $R_S = 60268$ km is the radius of Saturn (Lamy et al., 2008a). At Earth, Morioka et al. (2011) attributed an approximate limit of $7R_E$ to the equatorial shadow zone, where $R_E = 6371$ km is the radius of Earth.

Given that AKR generation is intrinsic to the magnetic field, the tilt of the planetary field with respect to the rotation axis combines with the highly directive AKR beaming to produce an illumination region that is time-dependent. Temporally, significant periodicities have been found at semi-diurnal and diurnal timescales, the latter of

which has been attributed to geometrical viewing effects as the emission region precesses, like the magnetic dipole, with respect to the rotation of the Earth (Lamy et al., 2010). Other suggestions for the source of this modulation include an intrinsic modulation due to the effect on the ionosphere of the tilt of the magnetic dipole with respect to the incoming solar wind (Panchenko et al., 2009) or a physical origin within the magnetosphere itself (Morioka et al., 2013). Discerning the origin of this variability is useful to further the understanding of the magnetosphere-ionosphere coupling.

This work aims to extract AKR from the raw data of an Earth-orbiting spacecraft, as well as to interpret and quantify any visibility effects due to the location of the spacecraft relative to the radio sources. Moreover, the AKR has the potential to serve as an excellent diagnostic tool both for solar wind driving and for magnetospheric dynamics. Specifically, previous work has shown that AKR can intensify during periods of magnetospheric disturbance (Voots et al., 1977; Liou et al., 2000; Zhao et al., 2019). The generation of AKR requires the presence of strong, parallel electric fields that accelerate electrons to the necessary relativistic speeds within the magnetosphere-ionosphere coupling region. The well-studied physical phenomenon of the magnetospheric substorm manifests in various observable signatures in both the magnetosphere and ionosphere. In the magnetosphere, the magnetic field dipolarises following reconnection in the magnetotail and energetic plasma flows Earthward (Liou, 2002; Juusola et al., 2011). Energetic particles are injected into the ionosphere as the substorm current wedge strengthens the current systems at high latitudes, brightening the aurora and causing well known morphological changes in the oval (Akasofu, 1964; McPherron et al., 1973; Kepko et al., 2015). For AKR, not only does the emission intensify but the frequency spectrum undergoes characteristic changes in response to substorm behaviour. Observations with the Polar spacecraft have shown that the AKR source region morphology may have a dual structure, suggesting that a given field line has a more persistent AKR source at lower altitudes that suddenly extends to higher altitudes at the time of substorm onset (Morioka et al., 2007).

Before the properties of AKR can be studied in detail, the AKR-related radio signals must be disentangled from other radio emissions detected by a spacecraft's radio instrument. This non-trivial process is described in more detail in section 4.1.1 below. Broadly speaking, an orbiting spacecraft may detect multiple possible sources of radio emission at multiple wavelengths when surveying the radio environment. At kilometric wavelengths, corresponding to frequencies of $\sim$ 1 MHz and below, the long, drifting tails of solar radio type III bursts can be observed, which are ubiquitous when the spacecraft is in the solar wind (Krupar et al., 2018). As well as this, characteristic frequencies of the local plasma can be observed at lower frequencies. This can occur both in the solar wind, at the plasma frequency and harmonics following Langmuir waves, or within the magnetosphere, where dense, turbulent plasma in the magnetosheath leads to a rise in quasi-thermal noise (QTN)

(Meyer-Vernet et al., 1998; Meyer-Vernet et al., 2017). Thus AKR is often observed in superposition with other waves and must be explicitly selected, where possible, for a complete study. Goniopolarimetric (GP) inversion techniques are useful for selecting AKR, as the Stokes parameters of an incident wave can be derived using a model that accounts for the geometry of both the radio antennae and the source (Cecconi and Zarka, 2005; Cecconi, 2019). Then, the circular polarisation can be used to discriminate against other sources; the few observations of solar radio Type III bursts at frequencies < 1 MHz show weak polarisation (Reiner et al., 2007; Pulupa et al., 2019). This has been done at Saturn, using the radio instrument on board the three-axis stabilised Cassini spacecraft to observe SKR, the Kronian analog of AKR. As the Cassini spacecraft flew by Earth, its radio instrument was turned on for a month long period. During this time, the instrument was used to retrieve the circular polarisation state of the AKR, allowing the general emission characteristics, such as the emission power, and the temporal modulation to be studied (Lamy et al., 2010). For this month-long period, the Wind spacecraft was travelling on orbits that carried it through the nightside magnetosphere at perigee, allowing it to make remote observations of the AKR source region, as well as other opportunities to observe AKR from other local times (LT). Although it is not possible to apply previously-developed GP techniques for spinning spacecraft to AKR observations with Wind, a selection technique based on the observed variability on timescales of seconds has been developed and applied. This has provided an effective selection of AKR emission, allowing a quantitative analysis and comparison to be performed. Here I focus on the unique dual-vantage-point of this Cassini-Wind conjunction during 1999. The instrumentation and calibration of the radio data are described in chapter 3, while in the following section 4.1.1 the selection technique which I have applied to extract AKR is described. In section 4.2 I compare and contrast the viewing geometry and observations of Wind and Cassini as they traverse the terrestrial magnetosphere on different paths. In section 4.3 I summarise our findings and interpretation of the complementary data.

4.1.1 Empirical Selection of AKR

As mentioned in section 3.1.2, the Wind/WAVES Z antenna is spin-axis aligned. As the spacecraft rotates, antennae in the spin-plane observe a modulating signal that is dictated by the rotation period and the position of the antennae with respect to the source location and other parameters. While this modulation can be used to derive source parameters using GP inversion as previously mentioned, these require that the source parameters are constant during a spacecraft rotation; a constraint which is often broken for AKR. The spin-axis aligned Z antenna sees no such modulation due to the spacecraft rotation, and so any variability in the received power can be attributed to changes in the intensity of a radio source, assuming that a single source is

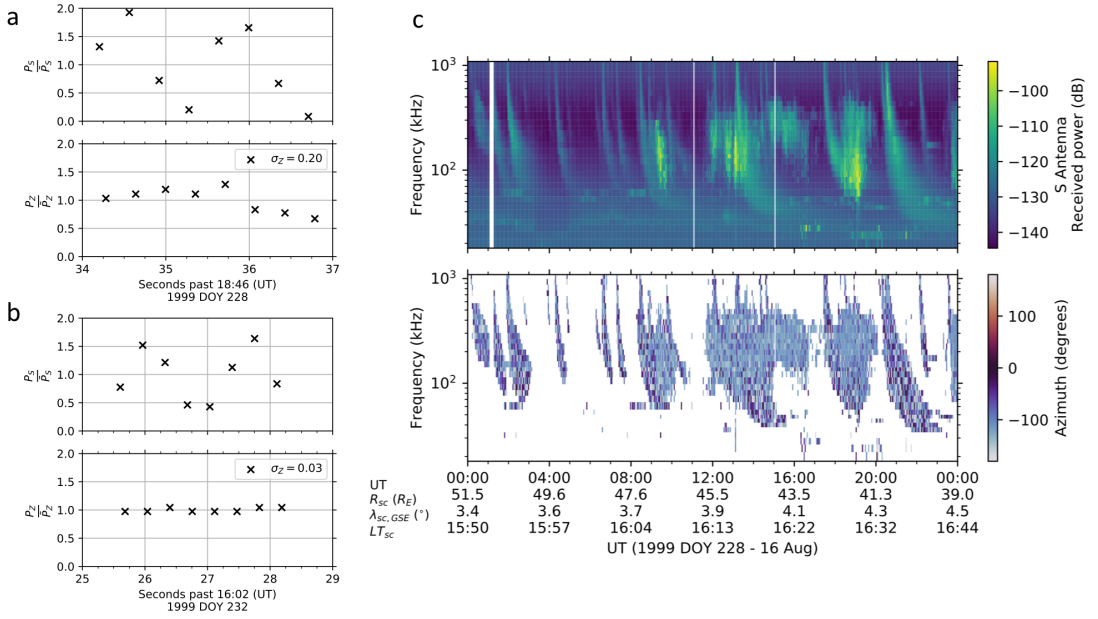

FIGURE 4.1: Measurements (P_S, P_Z) made by the synthetic-inclined (S) and spin-axis-aligned (Z) antennae of Wind/WAVES during a single spin, normalised by the average received power during this time ($\bar{P}_S$, $\bar{P}_Z$). (a) Spin observations at 124 kHz, corresponding to a rotation during the burst of AKR emission between roughly 1800 and 2000 UT in figure 4.1c. (b) Spin observations of an isolated Type III burst at 124 kHz, on 1999 DOY 232, illustrating the modulation pattern produced in the S antenna and the lack thereof in the Z antenna, observed for measurements of a near-constant intensity source. The value of the selection metric, σ_Z, is given in the legend of the bottom panel for both 1a and 1b. (c) Dynamic spectrograms showing 24 hours (1999 DOY 228) of the power received by the S antenna, in dB, in the top panel. Only observations with a signal-to-noise ratio (SNR) of > 25 dB are shown, for clarity. The bottom panel shows the apparent azimuth of the radio source, determined by application of a GP inversion for use with Wind AKR observations. Only observations with a signal-to-noise ratio (SNR) above 25 dB are shown. The azimuthal angle of the source is given in a non-rotating coordinate system (see text) with angles of 0° indicating a source in the direction of the Sun, negative angles indicating a source to the right of the Wind-Sun line and positive angles indicating a source to the left of the Wind-Sun line. For the period shown in figure 4.1c, Earth is at approximately -130° in this coordinate system.

observed. It has been mentioned that the spacecraft measures a superposition of multiple spatially-separated sources, limiting the observations by the temporal and spectral resolution of the instrument. Although this is less true for the spin period than it is for the sweep duration, it is possible that the variability measured by the Z antenna for a spin is due to the more slowly varying intensity of separated sources. Given the generation mechanism of AKR, however, it is likely that a single source will have a highly varying amplitude on spin timescales of seconds. While it is non-trivial to discern between the two effects, it is important to note that this may also lead to an overestimation of the AKR selection, although this effect is negligible when data are averaged over the sweep duration.

A statistical proxy for AKR can be derived from the Z antenna by modelling the 8 measurements made during a single spin as a normal distribution centred on a mean

intensity, with any variability then being described by its standard deviation σ. To be able to compare the standard deviation between sources of different mean intensities, the measurements are normalised by the mean intensity of the spin. This gives σ_Z, the standard deviation of the spin-normalised Z antenna measurements. σ_Z is calculated prior to background subtraction, to retain the observed variability (it is assumed that any variability represented by σ_Z will be predominantly influenced by the sources of the strongest intensity). Figure 4.1a shows the spin-normalised measurements made by the S and Z antennae during an exemplary AKR burst. It is not clear from the figure that the S antenna is displaying an insufficient modulation pattern to derive the GP source parameters and an analytic relationship between the S and Z measurements is not known. However, the variability across the Z antenna measurements shows that the observations do not meet the criteria of constant intensity for GP inversion, and the σ_Z value for this spin is given in the legend of the bottom panel of figure 4.1a. Figure 4.1b shows similar data for an observation of a solar radio Type III burst, with the double-peaked modulation pattern in the received power clearly visible in the top panel and the Z antenna measuring nearly constant intensity emission; illustrating measurements of a radio source more appropriate for use with a GP inversion. While a comprehensive study of the σ_Z distribution is not included, examination of the dynamic spectrograms show that the Z antenna consistently measures higher variability (using σ_Z) during periods of AKR bursts. To select regions that correspond to AKR emission, a numerical threshold is chosen based on visual identification of the dynamic spectrograms from Wind during the Cassini flyby; here $\sigma_Z \geq 0.1$. Given that the opposite limit of σ_Z selects sources that are less variable, σ_Z could be useful to select data that is more appropriate for a GP inversion with Wind. See 4.6 for further justification of the choice of the threshold value.

Figure 4.1c shows 24 hour dynamic spectrograms of Wind AKR observations and their general unsuitability for GP applications. The top panel shows a spectrogram of the measurements made by the S antenna; relatively faint Type III bursts are seen throughout the day, whilst bursts of intense AKR are also observed. The bottom panel shows the result of an attempt to apply the GP inversion of Manning and Fainberg (1980) to the Wind observations. The azimuthal angle of the source is given in a fixed coordinate system, independent of the spacecraft rotation, that is defined by an x-axis in the direction of the Sun with the x- and y-axes in the ecliptic plane, and a z-axis that completes the orthonormal frame and is directed Southward of the ecliptic plane. Given that the retrieval of direction-finding parameters for radio sources is dependent on a strong signal, only observations with a signal-to-noise ratio (SNR) of > 25 dB are shown, highlighting the presence of solar radio Type III bursts (multiple examples between $\sim$ 100-1000 MHz, 0000-0400 UT, or at all frequencies after 2000 UT) as well as AKR. Azimuthal angles of 0° indicate a source in the direction of the Sun, negative angles indicate a source to the right of the Wind-Sun line and positive angles indicate a source to the left of the Wind-Sun line. The GP inversion is subject to a degeneracy

in the wave vector direction, so angles that suggest an unphysical source direction for AKR have been transformed appropriately; Earth is at approximately -130° for the data shown. For the AKR between 0800 to 2000 UT, the azimuthal angle is poorly constrained and has high variability during AKR observations, due to the aforementioned variability during the spacecraft rotation. While σ_Z acts as a proxy for the radio source here, it is noted that without access to the GP inversion and polarisation information a physical inference cannot be made and so the selection is empirical. With average σ_Z spectra for each sweep, a mask can then be created and applied to the calibrated flux densities to select data that meets this criteria; here the flux densities are also averaged across the 3 minute sweep cycle. In this case the consideration of multiple spatially-separated sources cannot be ignored, and the flux spectra represent the spatial average of AKR emission across a relatively wide longitude as well as a temporal average.

Figure 4.2 shows two examples, A and B, of 24 hours of calibrated Wind/WAVES data (top panel) with the variability proxy σ_Z (middle panel) and the application of the resulting mask (bottom panel). Wind observations in both A and B contain many Solar Type III bursts with various drift rates that at times cover the entire RAD1 frequency range, as well as increases in QTN and emission at the plasma frequency at frequencies < 100 kHz. The middle panel shows the effectiveness of σ_Z as an identifier of AKR emission, with observations of Type III bursts exhibiting a standard deviation less than that of the AKR by about an order of magnitude. AKR is generally more intense than Type III bursts, and this couples with the aforementioned considerations of the AKR generation mechanism and viewing geometry to produce the observed discrepancy in the σ_Z distributions of each source, as shown here by the middle panel of figure 4.2. While not shown here, the 52 kHz channel has persistently higher σ_Z due to radio frequency interference (RFI). In figure 4.2 (and figure 4.5), the 52 kHz channel has been removed and the values of σ_Z in neighbouring channels used to interpolate an updated 'background' value to increase visual clarity. Other frequency channels exhibit higher σ_z due to RFI effects, although these are lower than that of the 52 kHz channel and contaminate the data less; an example can be seen around 800 kHz in figure 4.2. For the remaining analysis, after selecting the AKR data with the σ_Z criterion, flux densities from the 52 kHz channel are removed to avoid contamination. AKR can be seen in both examples; in A, Wind is approaching perigee at around 1600-1700 LT and 4° latitude, and emission is observed for 11 hours between $\sim 80 - 800$ kHz; it exits perigee in B, crossing 0800-0900 LT around $-6°$ latitude, and observing more sporadic emission patches throughout the day across a narrower frequency range, $\sim 100 - 500$ kHz.

Given that the metric for selection, σ_Z, is determined using the variance of measurements made during a spin, there are other sources of emission that could be responsible for the retention of a particular sample. Instrumental RFI is an example of

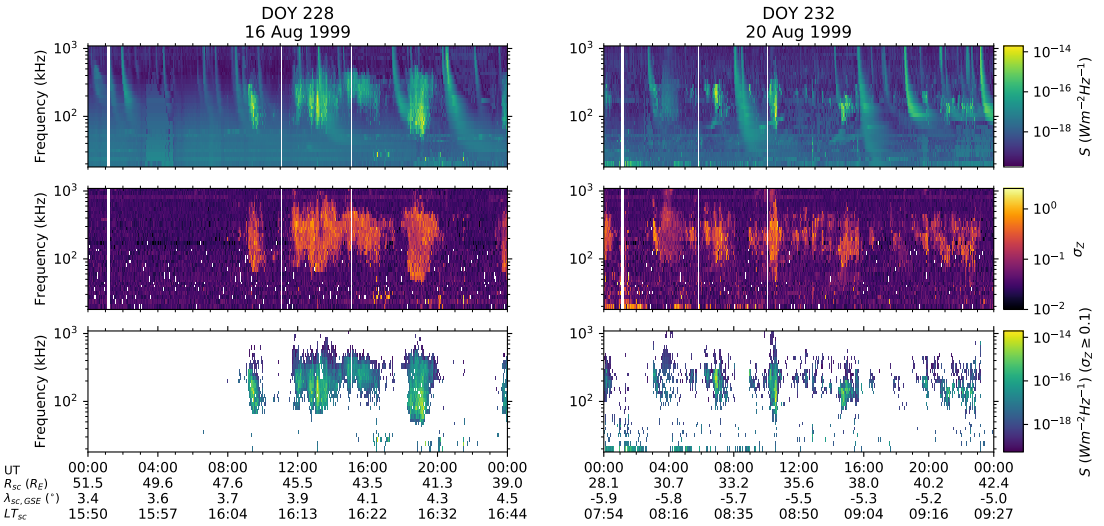

FIGURE 4.2: Two examples of application of the empirical selection detailed in section 4.1.1 to 24 hours of Wind data (3 minute resolution). For each example A (left) and B (right) the top panel shows flux density observed by Wind and derived by the method outlined in section 3.1.4, the middle panel shows σ_Z, the statistical proxy of the source amplitude variability, and the bottom panel shows the flux density with the selection mask applied (see section 4.1.1). The lower limit of the colour-bar of the middle panel is set at 10^{-2} for visual clarity. The radial distance, ecliptic latitude and local time for each example are shown in the ephemeris at the bottom of the plot.

this, but particularly rapid changes in intensity due to energetic fluctuations in the local plasma can also produce signatures similar to those produced by AKR. Particularly when Wind travels through the turbulent, dense plasma in the magnetosheath (see ∼DOY 229-231 and 251-254 in figure 4.5) the majority of the emission at lower frequencies is retained. At times when Wind is on the dayside, within the solar wind, emission is occasionally selected that has no observed, corresponding AKR signal at higher frequencies, and is assumed to be caused by similar local and temporal variations in the plasma. Intensification of the signal at other characteristic frequencies of the plasma are also occasionally seen and retained by the selection, such as emission at the plasma frequency. The retention of non-AKR signals is lessened at higher frequencies, where Wind typically sees contributions from AKR, Jovian hectometric or kilometric radiation which is often faint (Zarka et al., 2004), or solar radio bursts which have little variability across the spacecraft spin period. As well as other sources of emission that could be responsible for the variability, there is also the possibility that Wind is subject to incident waves from multiple radio sources. Due to this, it is not guaranteed that only AKR will be present in any of the selected data, although the most intense emission determines the modulation pattern in these cases. AKR is typically more intense than other radio sources for Wind observations, and this is the case particularly when Wind is at a favourable viewing position for AKR. Observations where solar radio type III bursts are the most intense emission arriving at the Z antenna, for example, are thus removed using the selection with σ_Z. Although fine structure and variability has been observed

in the spectra of Type III bursts and there is no complete way to discriminate between this variability and that exhibited during AKR observations, applications of the selection such as those in figure 4.2 show that, on average, observations where the Type III dominates are removed. Given the ubiquity of Type III bursts and sources of other less variable emission, and the simplicity of the σ_Z selection criteria used here, the technique is utile for studying AKR emission, as shown in the following section, and conversely for removing the contribution of AKR in studies of solar radio bursts. Applying the flux-density calibration and selection of AKR to Wind/WAVES observations since 1994 can form a unique dataset to investigate AKR characteristics. The next section takes advantage of the selection to make an initial comparison to AKR radio measurements obtained by Cassini in 1999.

4.2 Multipoint Observation with Cassini

4.2.1 Spacecraft Ephemerises

Figure 4.3 shows the Wind trajectory projected onto the ecliptic plane for the period studied here, as well as part of the Cassini trajectory. The start of day of year (DOY) 230 is indicated in colour for each spacecraft, during which Cassini reached its closest approach to Earth at a radial distance of 1.2 R_E. After traversing the dawn flank of the magnetosphere and passing Earth, Cassini continued downtail between 0100 and 0200 local time (LT) at $\sim 9\ R_E/h$. Figure 4.4 shows the latitudes of both spacecraft in both geocentric solar ecliptic (GSE) and magnetic coordinates. The latter refers to the coordinate system used in Lamy et al. (2010), which defines positive latitudes as those in the Northern magnetic (Southern rotational) hemisphere.

During Cassini's flyby of Earth and the 30 day period studied by Lamy et al. (2010), from 15th August to 14th September 1999 (DOY 227 to 257), Wind completed close to two petal orbits with a perigee radii of $\sim 13\ R_E$ and apogee radii of $\sim 88\ R_E$. At the start of this period, Wind approached its first perigee from a position duskward of Earth at roughly 1500 LT on DOY 227, with a geocentric-solar-ecliptic (GSE) latitude of 3.0° and a radial distance of 67 R_E. From there, Wind approached the magnetosphere and crossed the bow shock and magnetopause before the first perigee was reached. Wind reached perigee around 0100 LT, at a GSE latitude of 1°, while traversing the magnetotail. Wind then exited the magnetosphere, covering the dawn flank and reaching apogee on DOY 241 at a GSE latitude of $-0.4°$ around 1200 LT. After 23 days Wind reached 1500 LT once more at a closer radial distance of 44 R_E and a GSE latitude of 4.6°. Entering the nightside magnetosphere for the second time during the period, Wind reached a second perigee on DOY 252 at 0000 LT and close to the ecliptic plane. Wind then exited the magnetosphere once more, and the final observations that

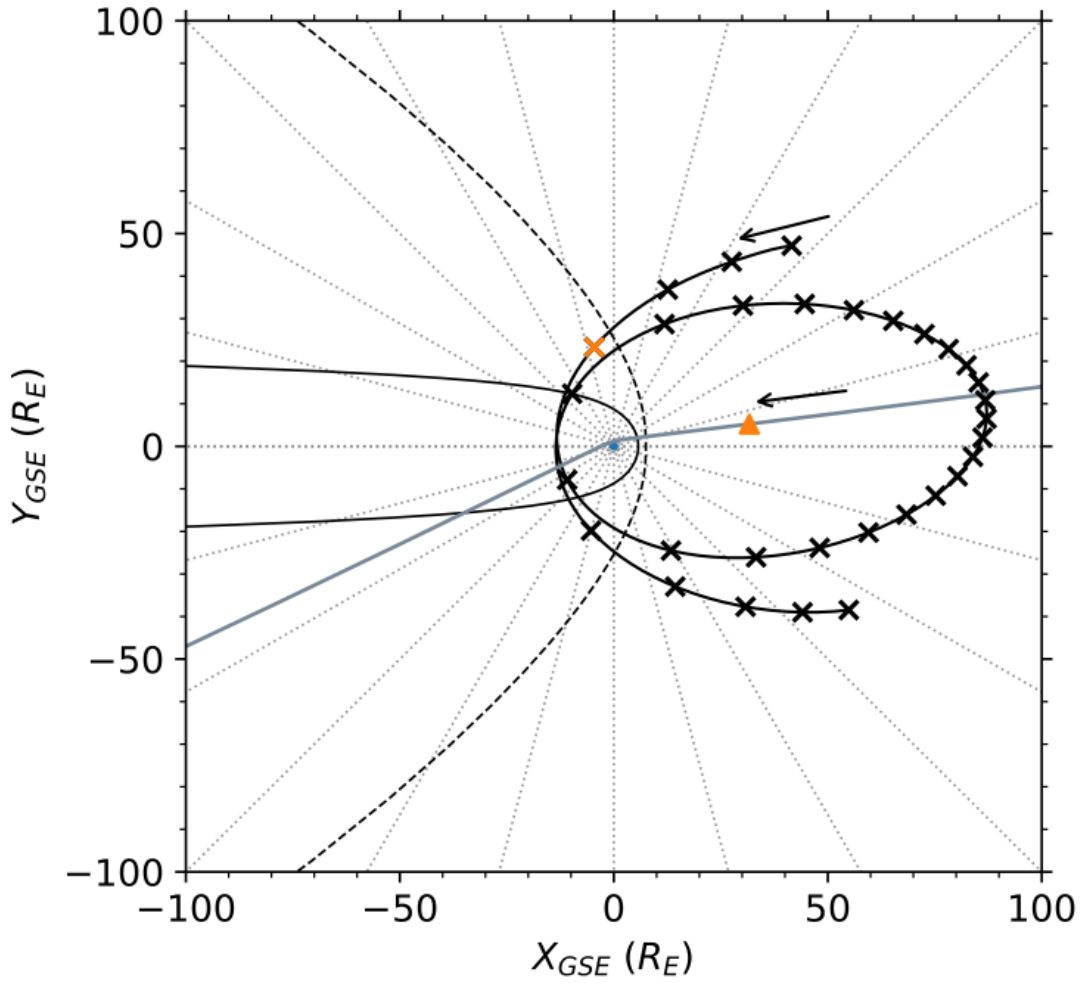

FIGURE 4.3: Orbital trajectory of Wind for 1999 DOY 227-257, projected onto the ecliptic plane. The start of each day for the Wind trajectory is marked by crosses. Also shown in grey is the Cassini trajectory for the closest approach, with the start of DOY 230 marked by the triangle. The Cassini trajectory can be found to a greater extent in figure 2a of Lamy et al. (2010). The arrows indicate the direction of travel for both spacecraft and the coloured markers indicate the start of DOY 230. Average modelled magnetopause and bow shock surfaces are shown as thin solid and dashed lines respectively; the Sun is to the right. The former is given by the model of Shue et al. (1998), using solar wind data from OMNI with average parameters. The latter surface is derived using similar data and the model of Wu et al. (2000).

are conjunct with Cassini are made at around 1000 LT with GSE latitude of $-3.0°$ and a radial distance of 67 R_E.

As mentioned in section 3.1.4, GP inversions have been successfully applied to observations from Cassini and allowed the circular polarisation of the radio emission to be determined and thus the hemisphere of origin. For the empirical selection of AKR emission, used here with Wind, there is no unambiguous way to determine the circular polarisation from the flux measurements. Due to the anisotropic, widely-beamed emission from the AKR source regions, visibility of the emission from either pole is highly dependent on the magnetic latitude of Wind, and inferences of

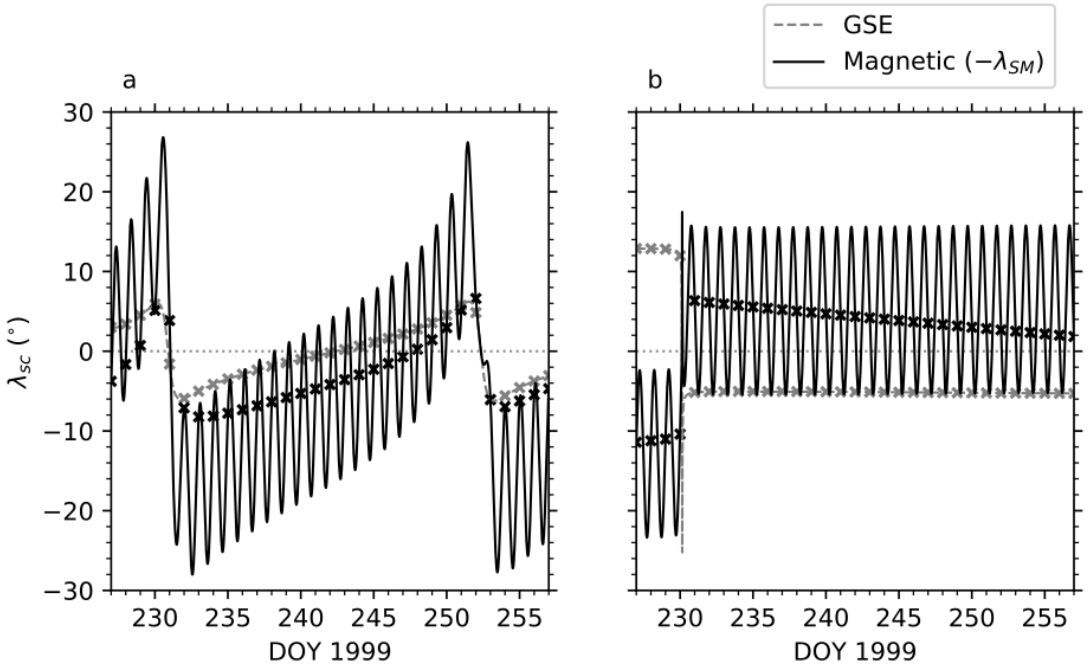

FIGURE 4.4: Latitudes of the Wind (a) and Cassini (b) spacecraft for the period shown in geocentric (GSE) coordinates with the grey, dashed line and magnetic coordinates with the black, solid line. Magnetic coordinates are as defined in Lamy et al. (2010), with positive magnetic latitudes in the Southern geographic (Northern magnetic) hemisphere. The magnetic coordinate system used here has the z-direction oppositely defined to that in solar magnetic (SM) coordinates, indicated by $-\lambda_{SM}$ in the legend. Markers show the beginning of each day.

the origin of the emission can be made based on this. While Wind is on the dayside, approximately between the two perigees at DOY 231 and DOY 252, it covers a range of low magnetic latitudes in first the Southern then the Northern magnetic hemispheres, crossing the magnetic equator near the apogee (see figure 4.4). In both cases where Wind crosses the nightside, where AKR is expected to be most visible, the spacecraft approaches from the dusk flank in the Northern magnetic hemisphere and crosses into the Southern magnetic hemisphere at perigee. Magnetic coordinates are as defined in Lamy et al. (2010), with positive magnetic latitudes in the Southern geographic (Northern magnetic) hemisphere. The magnetic coordinate system used here has the z-direction oppositely defined to that in solar magnetic (SM) coordinates. Given that the magnetic latitude does not exceed 30°, it is uncertain whether or not the spacecraft will be in either or both of the regions illuminated by emission from either hemisphere. Previous examination of the average AKR source region has suggested that emission from both hemispheres can be observed at distances $> 12R_E$ in the equatorial plane (Gallagher and Gurnett, 1979), with the approximate perigee distance of Wind ($\sim 13R_E$) implying that this will be the case for all nightside observations for this period. In their study, Lamy et al. (2010) use the polarisation information to assess the average AKR power from each hemisphere when Cassini is above a given magnetic latitude finding that LH AKR was close to 4 orders of magnitude weaker

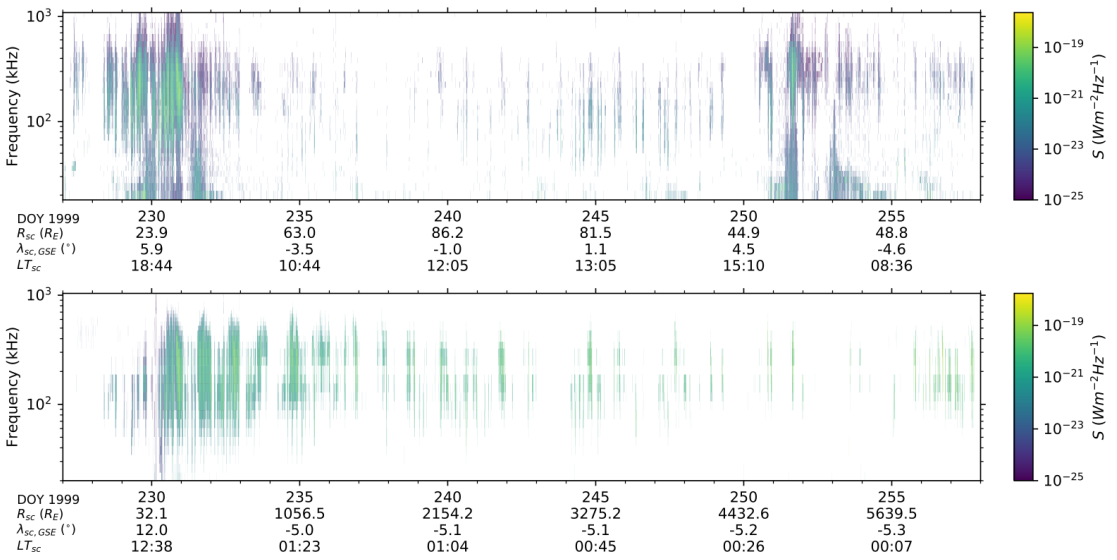

FIGURE 4.5: Dynamic spectrogram showing the flux density measured by Wind/WAVES (top) and Cassini (bottom) for 1999 DOY 227-257 and normalised to a distance of 1 AU. The top panel shows the average flux density at 3 minute resolution as selected with the σ_Z threshold described in section 4.1.1. The flux density is computed by calibrating the power received by the spin-axis aligned Z antenna, as outlined in section 3.1.4. The bottom panel shows the flux density observed by the Cassini spacecraft, namely the maximum of the LH or RH AKR emission of a given frequency at 90 s resolution (for complete details of the calibration and selection of AKR with Cassini, see Lamy et al. (2010)). The radial distance, ecliptic latitude and local time of each spacecraft are shown in the ephemeris at the bottom of each panel.

than the RH AKR when the spacecraft had a magnetic latitude $\lambda_m > 10^\circ$. This suggests that Wind is likely illuminated by emission from AKR sources in both hemispheres whilst near the equatorial plane, with Southern, LH emission likely to be dominant prior to perigee and Northern, RH emission afterwards.

4.2.2 AKR Flux Density and Power

Figure 4.5 shows the AKR flux density of both Wind and Cassini for the entire 30 day period studied here. The AKR flux density with Wind is obtained using the calibration and selection outlined in chapter 3 and section 4.1.1. The AKR flux density with Cassini contains that of both LH- and RH-circularly polarised AKR, obtained using a GP inversion technique and selecting data with $|V| \geq 0.2$, where V is the normalised Stokes parameter describing circular polarisation (Lamy et al., 2010). The maximum of either the LH or RH AKR is shown at 90 s resolution in the Cassini spectrogram. Both flux densities are scaled for the distance from the approximate source (Earth's center) and normalised to 1 AU to enable a comparison between the two datasets. The general effect of viewing position on the AKR observations from each spacecraft can be seen here; emission is stronger and more consistent for Cassini as it travels away from Earth downtail, remaining on the nightside, while a periodic variability is seen in

the Wind spectrogram as it passes the nightside during its perigees. While the day-to-day variability in the observed emission is not studied here, it is interesting to note differences between the two perigee observations. Wind sees more persistent, stronger emission for the first perigee (∼DOY 229) than the second (∼DOY 251). While this variability between orbits is not surprising given the changing solar wind conditions that affect AKR, it demonstrates the differences between observations made at different times which will clearly bias any average result with a limited selection of data.

Figure 4.6 shows AKR flux density spectra from both spacecraft given by statistical thresholds, namely the median spectra and those for the 90% and 99% quantiles, or increasing intensity thresholds. The top panel shows Cassini flux densities for both LH and RH circularly polarised AKR, reproducing figure 6a of Lamy et al. (2010). The middle panel shows Wind flux densities returned by the selection (described in section 4.1.1) applied to data from 1999 DOY 227-257. Given the anisotropy of the AKR beaming and the longitudinal distribution of AKR source regions, it cannot be assumed that each spacecraft will observe the same emission region at a given time from different viewing positions in space. To elicit a valid comparison of the reduced spectra between the spacecraft, I select Wind data such that only observations made from a similar viewing position are included; Cassini was in the region with a magnetic latitude $-23^\circ \leq \lambda_m \leq 16^\circ$ and within 0000 to 0200 hours LT during its flyby. A complete discussion of the flux densities observed by Cassini can be found in Lamy et al. (2010), but here I compare the main features with those of Wind.

While the Cassini spectra for both LH and RH AKR flux see a mostly shallow increase up to the peak at $\sim$ 200 kHz, this is not the case for Wind. A consistent plateau is seen in each of the spectra in the middle panel below 50 kHz, after which the flux density increases more sharply for each quantile. Discrepancies in the spectra can be seen at lower frequencies, which is likely due to a combination of the nature of low frequency AKR emission and the fragmented viewing by Wind when in the appropriate position. While Cassini makes 30 days of remote observations in this magnetic latitude and LT range, Wind spends ∼9 hours in the same position, with each observation ∼20 hours apart. Without considering the viewing effects, the transience of AKR below 100 kHz alone could produce the discrepancies in the average spectra. As well as this, Wind is closer to Earth and passes the nightside while crossing the magnetic equator, which could affect the viewing of high altitude, low frequency AKR sources. The σ_Z selection is limited at low frequencies due to contamination by QTN and local plasma waves, although I assume that the aforementioned effect dominates given that Wind is likely inside the magnetosphere for the selected observations (as shown by the average magnetopause boundary in figure 4.3) where these emissions have less of a presence than in other regions. Figure 4.6 also shows better agreement between the two spacecraft at $>$ 100 kHz, the resulting range including the typical

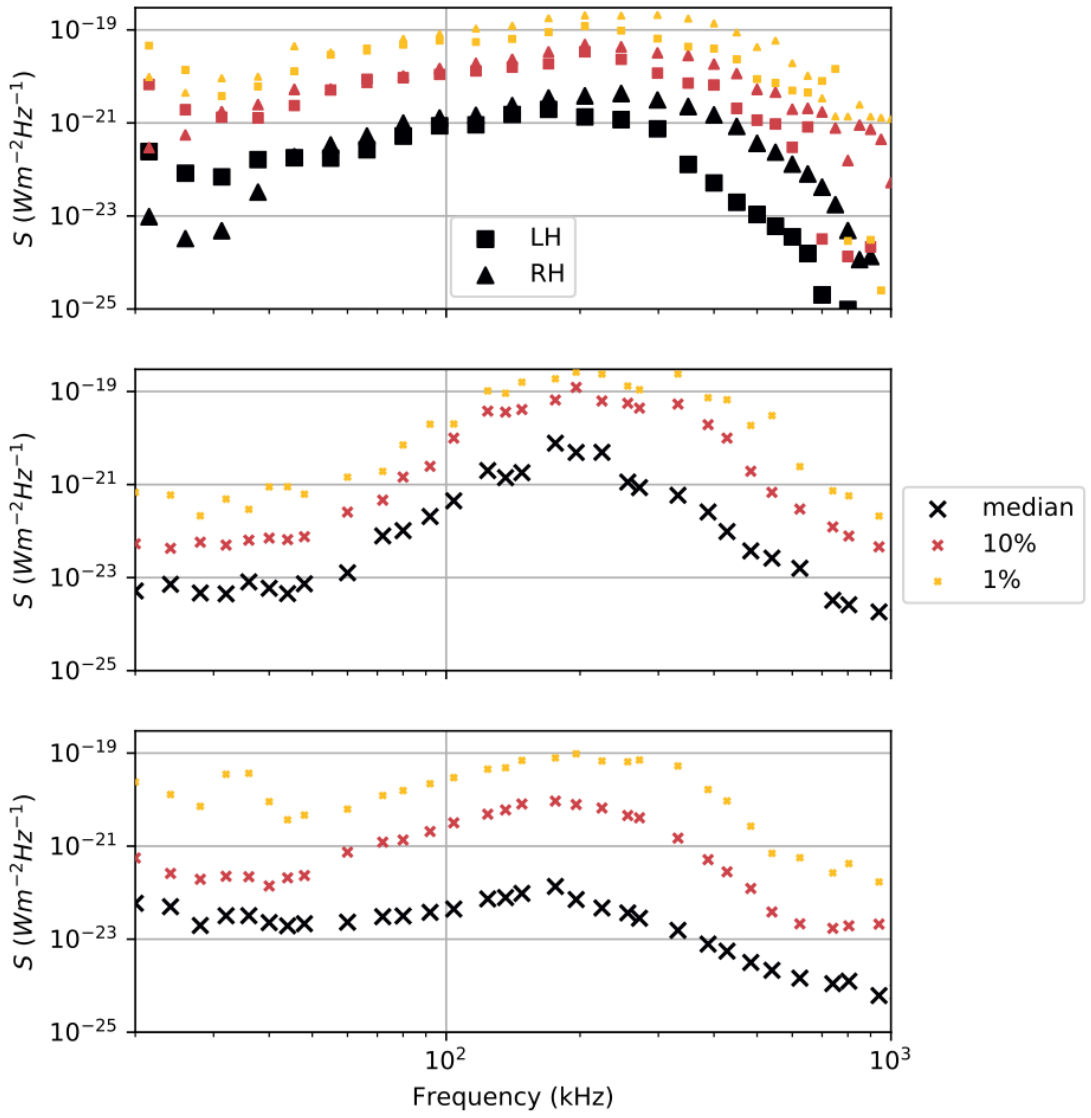

FIGURE 4.6: Reduced flux density spectra comparing AKR observations from Cassini during the whole period (top panel) with those made by Wind when in a comparable viewing position (middle and bottom panels). For this, the Wind data was further selected such that the spacecraft was located from $-23^{\circ} \leq \lambda_m \leq 16^{\circ}$ and within 0000 to 0200 hours LT. Flux density data in each case are reduced to give the measured intensity reached 50% (median - black), 10% (red) and 1% (orange) of the time. The top panel shows spectra for both the LH and RH circularly polarised AKR as given by the GP inversion applied to Cassini. The middle panel shows AKR- and position-selected data from Wind during the 30-day period studied here. The bottom panel shows AKR- and position-selected data from Wind for all of 1999, to increase the statistical rigour of the selection verification (see main text).

spectral peak of AKR. The AKR emission at higher frequencies is known to be more temporally consistent and can be said to be better representative of the average AKR signal compared between remotely observing spacecraft. For these reasons, in the following, only the selected signal above 100 kHz is considered. At frequencies higher than this, discrepancies between the spectra may exist simply due to the two spacecraft primarily observing different AKR source regions as I do not expect the AKR spectrum to be constant at all LT.

Again comparing the Wind spectra in the middle panel with Cassini in the top panel of figure 4.6, the peak of the Wind median spectrum agrees, existing at a frequency close to 200 kHz and between the peak flux of the Cassini LH and RH AKR median spectra; also in agreement with initial AKR observations (Kaiser and Alexander, 1977b). While the differences at lower frequencies are likely due to contamination, the Wind median spectrum falls off more rapidly than the RH median spectrum of Cassini and is more comparable to the LH median spectrum. At the frequencies > 700 kHz, the Wind median spectrum is more closely comparable to the RH AKR median spectrum, although the aforementioned limitations prevent close physical interpretation of the differences or similarities between the spectra. Generally, however, the Wind median spectrum has a minimum at the highest observed frequencies, which again agrees with the Cassini measurements. Each of the Wind spectra that show the higher intensity thresholds in the middle panel show generally good agreement in magnitude with those of Cassini; a similar increase of 2 orders of magnitude between the median and highest intensity spectra is seen in the selected Wind data. This is interesting considering the small amount of time Wind spent in the region relative to Cassini, and suggests that the limited Wind measurements here are characteristic of the AKR that Cassini observes for the whole period. There is also evidence of broadening of the spectral peaks to higher frequencies with increasing intensity in the middle panel as observed by Cassini.

Given that Wind spends the least amount of time on the nightside during perigee for this period, it is important to consider the limiting effect of the position selection. To highlight this, while Wind spends $\sim 1.2\%$ of the time in the specified region during this 30 day period, 5.1% of the AKR data selected here is observed in this region. However, this increase shows the efficacy of the empirical selection in reflecting the preferential location of the nightside for observing AKR emission and the AKR sources themselves. Although the Cassini spectra cannot be compared with Wind observations made outside of the temporal range covered by the Cassini flyby, increasing the scope of the data included can allow me to characterise the selected data more rigorously by comparing the general features of the spectra. For this reason, the bottom panel of figure 4.6 shows spectra defined by the same thresholds but applied to Wind data from the entirety of 1999 after selecting the AKR as described. Although the magnitude of the spectra is lower (which is expected as more AKR emission is

included, assuming that the more extreme events will happen less regularly) the broadening of the spectral peak to higher frequencies with increasing intensity is present. There is a larger increase of 3 orders of magnitude between the median and highest quantile spectra in the bottom panel, suggesting that the observations made in the 30 day period here are more intense than other times in the same year. There is also a separate, much shorter peak around 30-40 kHz that exists in the highest intensity spectra of the bottom panel, which could be indicative of the average state of the magnetosphere or solar wind throughout 1999 as consistent Langmuir wave excitations may be seen close to the local plasma frequency in this region.

The AKR source region, as discussed in section 2.7, is typically found at altitudes of roughly 2000-10000 km along a given field line, corresponding to emission at frequencies 100-800 kHz. This higher frequency emission is much less transient than that of higher altitude sources that emit between $\sim 30 - 100$ kHz and are well correlated with substorm onset (Morioka et al., 2007). To characterise the AKR observed by Wind and facilitate the comparison between the two spacecraft, the selected flux data are integrated over the frequency range 100-650 kHz. While the frequency range used by Lamy et al. (2010) (30-650 kHz) encompasses both the lower frequency and main band of AKR, I increase the lower frequency limit here to mitigate the inclusion of spurious data as mentioned above. While this does not allow for a direct comparison between the integrated powers of Wind and Cassini, it enables general characteristics of the AKR, such as the viewing geometry and temporal modulations, to be studied. With a more refined selection of AKR signal at frequencies below 100 kHz, the power can be integrated over a frequency range such as 30-100 kHz to investigate the lower frequency AKR component. Given that the integration time of each flux density measurement is the spin period of the spacecraft, the power can be integrated by simply taking the mean of the flux densities and integrating over the frequency channels. The flux densities have been normalised to 1 AU, so this distance is used as the effective area for the integration. Although I derive the AKR flux as that from a point source, the AKR is emitted in a wide geometry and so I present the AKR power as a fraction of the true beaming in units of Wsr^{-1}.

4.2.3 AKR Viewing Geometry

Figure 4.7 shows the integrated power data described in the previous section 4.2.2 after taking the mean power in 1 hour spacecraft LT (GSE) bins and plotting the $\log_{10}$ power as a rose plot; the noon and midnight sectors are on the right and left of the figure, respectively, and the dawn and dusk sectors are on the bottom and top. A large asymmetry can be seen in the selected power with a 3-4 order of magnitude increase of the LT bins between 1700 to 0300 over those on the dayside that have the lowest powers, namely the LT sector at 1100 hours. The broad picture of figure 4.7 is thus

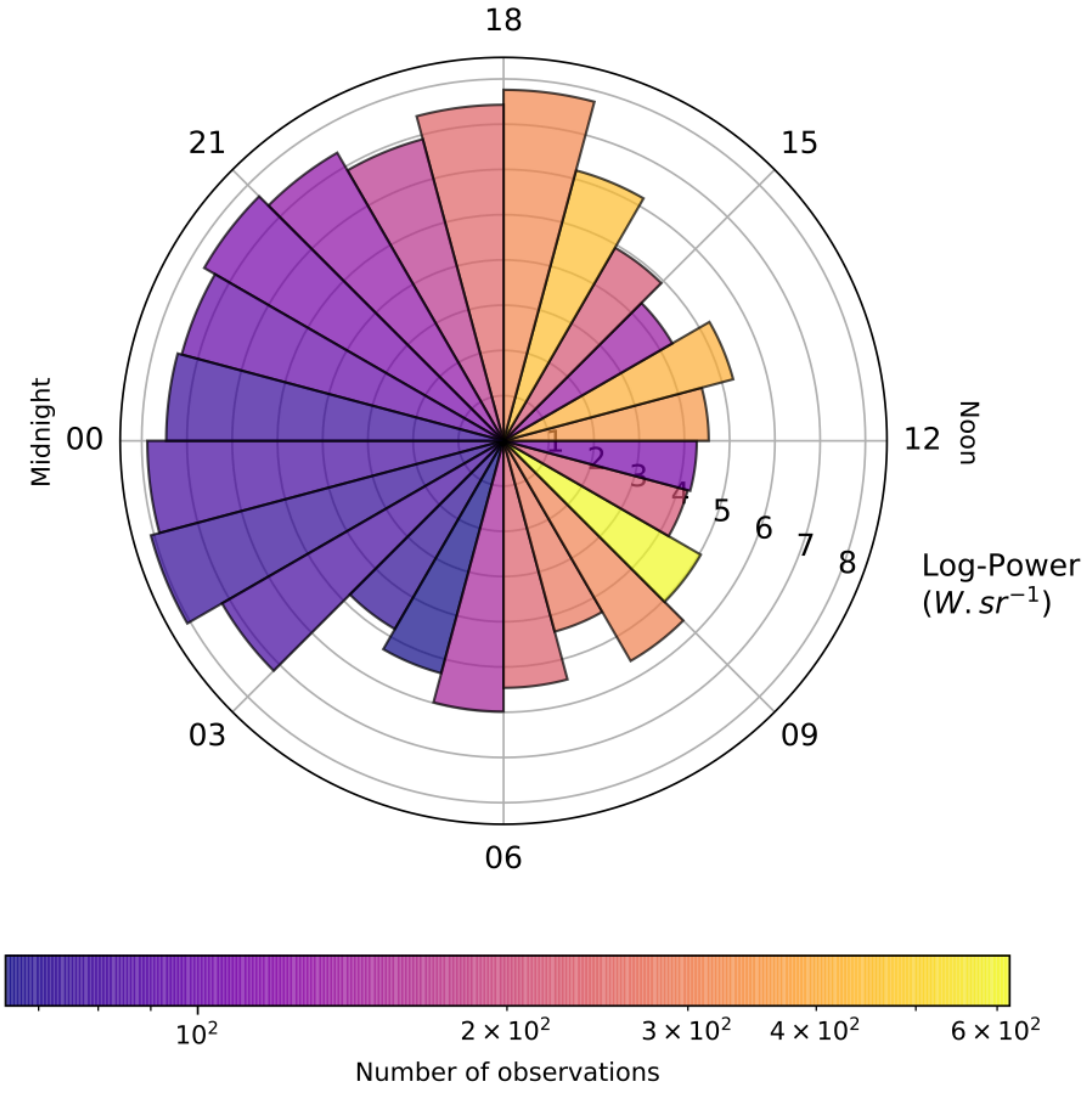

FIGURE 4.7: Log power in Wsr^{-1} integrated across the range 100-650 kHz for the AKR flux (as selected by 4.1.1) and averaged in LT bins 1 hour wide. The sun and noon sector is to the right, while the midnight sector is to the left. Colours show the number of 3-minute-resolution observations, retained by the empirical selection, in each LT bin.

consistent with previous findings which suggest that the source regions are located on the nightside and beam anisotropically (Alexander and Kaiser, 1976; Gallagher and Gurnett, 1979; Mutel et al., 2004, 2008). Also of interest here are the bins at 2100 and 2200 hours LT, in the centre of the range of intense emission. This corresponds to previous observations of the LT of the source regions most favoured by AKR sources (Panchenko, 2003; Mutel et al., 2004), as well as the average LT of the most intense AKR source region at 2200 MLT (Green, 2004). Given the illumination region of an AKR source, and that the observations here are made from comparatively large radial distances and with a swept frequency receiver, it is expected that the emission from an AKR source could be measured by Wind from a neighbouring LT sector. At Saturn,

this longitudinal difference has been observed to be up to 2 hours LT (Lamy et al., 2008b; Kimura et al., 2013). The location of the centroid of the most intense average power in figure 4.7 is an indication of the effectiveness of the AKR selection used here.

While AKR has been previously observed from the dayside it can be difficult, without polarisation information, to discern whether this emission is attributable to the illumination of the spacecraft by a source on the nightside via either emission viewing geometry or scattering, or that of a dayside source (Hanasz et al., 2003; Mutel et al., 2004; Schreiber et al., 2017). Deducing the exact origin of the source of emission is complex and is not possible within the scope of this work. However, the dynamic spectrogram in figure 4.5 as well as the distribution of average power in figure 4.7 show that we can observe AKR at all LT, with some of the most intense observations on the dayside made when Wind was within the LT sector 1300-1400 hrs and near the ecliptic plane.

The colour of each LT bin reflects the number of data used to compute the average, where each data point represents the power of each 3 minute frequency sweep. The orbital dynamics of the spacecraft produce the overall colour distribution, with perigee on the nightside limiting the number of observations that can be made and vice versa on the dayside. For this reason more total observations will be made on the dayside, but fewer of those observations will be selected given the preferred nightside location of the AKR source regions. This is seen when taking the ratio of the number of observations made in a local time sector with the number of selected data from the same sector. For the observations made on the dayside ($0600 \leq \text{LT} < 1800$) an average of 38% of data is retained by the selection, while 83% of nightside observations ($1800 \leq \text{LT} < 0600$) are retained by the selection. The variation in the number of selected data in the noon sector in figure 4.7 shows that the distribution here may not be indicative of the true average AKR power, as temporal variability of the state of the magnetosphere system will bias this count as the spacecraft crosses the dayside once during the 30 day period studied here. As discussed in section 4.2.1, Wind crosses the nightside twice during this period, so the data contributing to the average on the nightside are comprised of two separate samples of this region. Further discussion of the power distributions that produced the averages for each LT bin can be found in 4.7.

As well as the viewing constraints introduced by the interaction of the terrestrial magnetosphere with the solar wind in figure 4.7, the latitudinal distribution of AKR sources is such that I expect better viewing of AKR from individual magnetic hemispheres at higher latitudes. Figure 4.8 shows the distribution of AKR power with magnetic latitude with the LT of Wind indicated; while Wind was at relatively low magnetic latitudes for the period, it approached the nightside from the dusk flank at increasingly higher magnetic latitudes in the Northern magnetic hemisphere before crossing the magnetic equator and travelling to mid-latitudes as it leaves via the dusk flank. This can be seen in the top panel of figure 4.8, which shows all selected data for

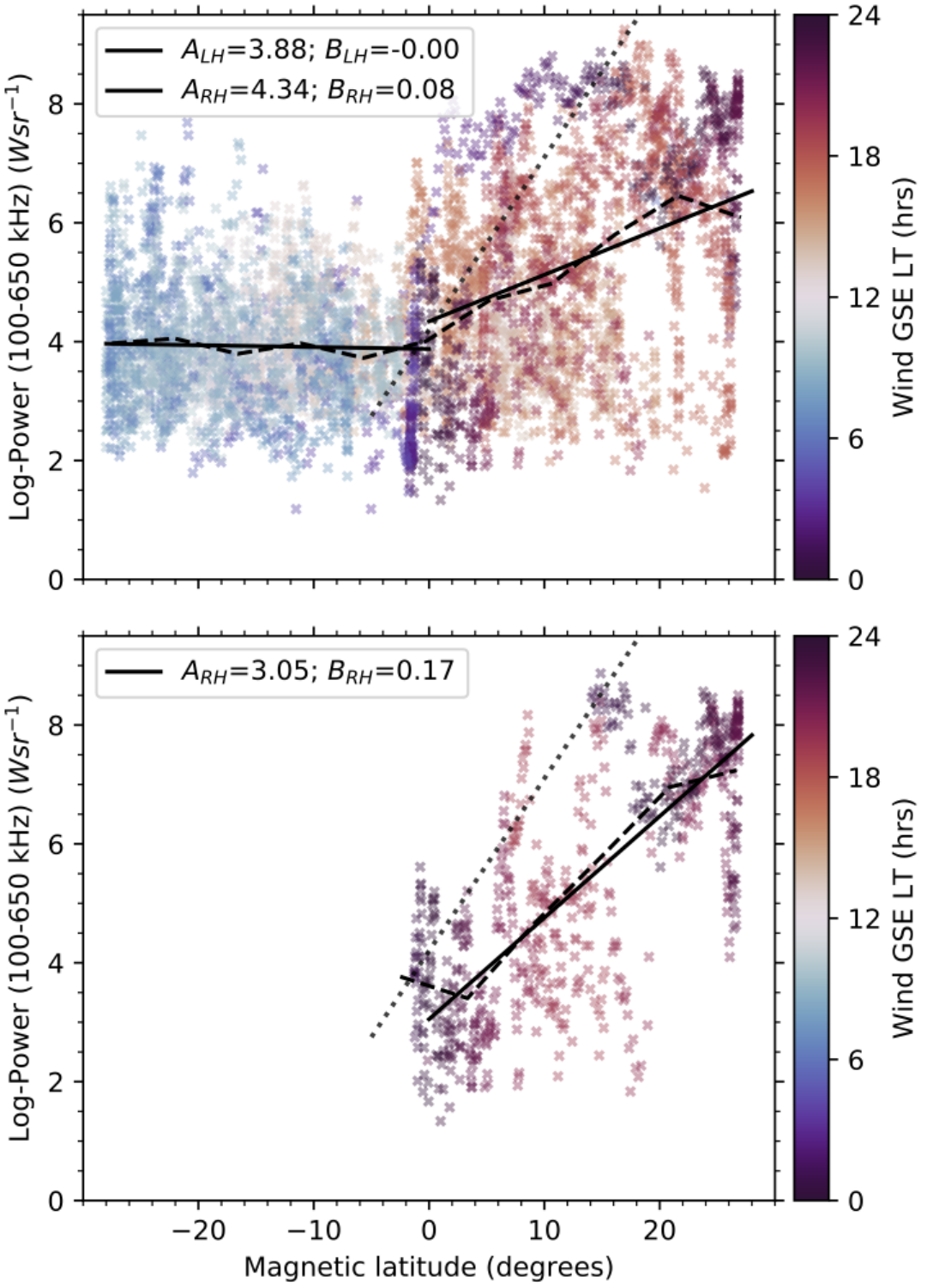

FIGURE 4.8: Distribution of AKR power (100-650 kHz) with magnetic latitude. The colour bar shows the LT of Wind in GSE coordinates, with observations in the Northern magnetic hemisphere made from the dusk flank, prior to perigee, and those in the Southern hemisphere from the dawn sector. The top panel shows all selected observations from DOY 227-257, whilst the bottom panel shows a subset of observations made between 1900-0100 LT to account for poor viewing. The dashed black line shows the mean of the log-power after binning in 5 degree wide latitude bins. The solid black lines show linear-log fits to the average data for negative and positive magnetic latitudes, where dominant emission from LH and RH circularly polarised AKR, respectively, is expected. The legend indicates the coefficients (in ascending rank order) of the linear-log fit of the form shown in equation 4.1. The dotted black line in each panel shows the analytic form found for Cassini RH AKR observations (see equation 4.1; A∼4.2, B=0.29) (Lamy et al., 2010).

the period. While powers were often observed as low as 10^2 Wsr^{-1} for all LT, the azimuthal viewing constraints of AKR are also seen as the average AKR power in the Southern magnetic hemisphere is relatively constant, indicating that Wind is not best situated to observe the most intense LH emission as it travels to the dayside, as shown also in figure 4.7. The bottom panel of figure 4.8 shows a smaller subset of the selected AKR data and attempts to mitigate the effect of the LT viewing, with only observations made between 1900-0100 LT included. While this LT range is slightly more restrictive than suggested by the distribution in figure 4.7, it is chosen for a better characterisation of the AKR for these observations. In both plots, the mean of the log-power observations made in 5 degree wide magnetic latitude bins is shown, with a linear-logarithmic fit of the form used in equation 1 of Lamy et al. (2010), repeated here

$$\log P = A + B\lambda_{W,m} \tag{4.1}$$

where P is the AKR power for a given hemisphere (eg LH or RH emission) in Wsr^{-1}, and $\lambda_{W,m}$ is the magnetic latitude of Wind in degrees. Lamy et al. (2010) found, using the polarisation to characterise each hemisphere, that the average emission from the Northern magnetic hemisphere, when integrated over 15 minutes, gave values A$\sim$4.2, B=0.29. Close to the magnetic equator it is expected that AKR from both hemispheres will be observed, but their observations also showed that RH emission can be observed at $< 10^2$ Wsr^{-1} from magnetic latitudes of up to 5° in the opposite hemisphere of origin (Southern). Without the polarisation state we cannot discern the exact origin of emission, so the fit in equation 4.1 is performed on data subset by negative or positive magnetic latitude, corresponding to assumed LH and RH AKR emission, respectively. The observations in the Southern hemisphere, made mostly on the dawn flank, show little dependence with latitude for reasons previously discussed. The differences between the positions of the spacecraft and the LT of Wind also clearly affect the observations made at positive magnetic latitudes, seen by the difference between the fit to positive latitudes in the two panels of figure 4.8. The bottom panel shows better agreement with the RH power dependence observed by Cassini, with a shallower increase of the average power with latitude. As well as Cassini being at a much greater distance from Earth and therefore observing less low power AKR bursts, poorer temporal and spatial sampling from ideal viewing positions by Wind are assumed to produce the observed discrepancy. A full statistical characterisation of the latitudinal dependence is out of the scope of this work and is not included.

4.2.4 AKR Temporal Modulation

To quantify the temporal variability of the AKR whilst accounting for the viewing, I perform a Fourier analysis on the entire time series as well as three subsets that comprise the two nightside passes/perigees of Wind during DOY 228-233 and

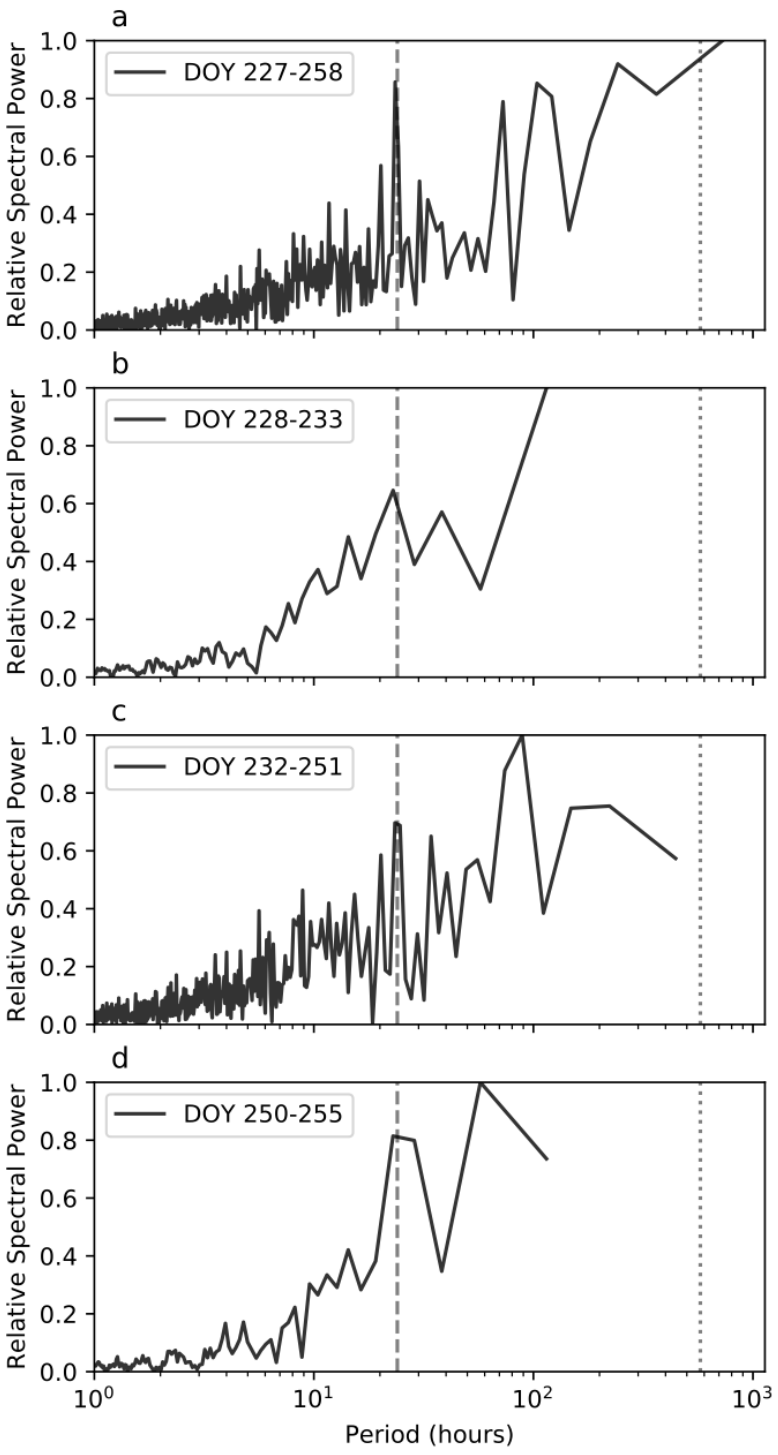

FIGURE 4.9: Fast Fourier Transforms (FFT) of the AKR power, integrated over 100-650 kHz, for the whole 30 day period (a), a 5 day period that spans Wind's first nightside perigee (b), a 19 day period spanning Wind's apogee on the dayside (c) and a 5 day period spanning Wind's second nightside perigee (d). The legends in each panel show the 1999 DOY for each subset, exclusive of the last date in each case. The integrated power is input at 3 minute resolution; data where no AKR is present are set to $P = 10^{-8}$ Wsr^{-1} to include them in the analysis. Analysis is performed on the integrated powers after applying a 3 hour rolling window and log-transforming the data. The relative spectral power is shown; data of each panel are normalised by the value at the respective peak. The vertical grey dotted line is at a period of 24 days, the approximate orbital period of Wind, highlighting the peak period of figure 4.9a. The vertical grey dashed line shows a period of 24 hours.

250-255, defined by a five day period approximately centred on the midnight meridian, and the dayside traversal during DOY 232-251. Figure 4.9 shows the result of a fast fourier transform (FFT) when applied to the Wind AKR power, integrated over 100-650 kHz, for the four aforementioned timeframes. The AKR power is initially averaged over a 3 hour window to smooth the data and remove local temporal variability. Given that the integrated power can vary over several orders of magnitude the FFT is performed after log-transforming the data to reduce the weight of this variability on the analysis. The relative spectral power is shown, having normalised the FFT output by the maximum spectral power found at the maximum period relevant to each timeframe. For example, the FFT output of the entire period in figure 4.9a has the maximum peak at a period of 24 days (576 hours), denoted by the vertical grey dotted line, and corresponding to the approximate orbital period of Wind during this time. The presence of a peak at this period can be explained with reference to figures 4.3b and 4.5; the perigee of Wind precesses dawnward across the nightside magnetosphere, measuring intensifications in the AKR as it passes the nightside across two to three days, separated by the dayside apogee. I do not comment on the origin of the maximum peaks of the FFT in figures 4.9b-d.

The vertical dashed grey line in each panel of figure 4.9 indicates a period of 24 hours. For figure 4.9a, covering the entire 30 day period, the FFT output is noisy, particularly at lower frequencies but also at periods between 1-24 days. A peak of comparable power to the maximum at a 24 day period is seen at a period of 24 hours, showing the observation of the diurnal modulation of AKR. Figures 4.9b and d, including data corresponding to the two nightside perigees, also both show peaks at 24 hour periods, with the spectral resolution being limited by the length of these time series. Figure 4.9c, corresponding to apogee on the dayside, also shows a diurnal modulation; each period was tested for statistical significance with bootstrapping, where the time series is shuffled randomly before undergoing the same analysis and comparing the spectral peak, allowing the null hypothesis to be tested. I found that the peak at 24 hours for each panel in figure 4.9 has a p-value of 10^{-5} and so is significant. While the presence of diurnal modulation has been previously observed and is a validation of the empirical selection used here in itself, a significant peak in Wind observations on the dayside further corroborates the hypothesis that the diurnal modulation is predominantly due to a geometric viewing effect. Given that the diurnal modulation is seen during observations near noon, and near the magnetic equator, I expect that intrinsic variability of the AKR sources is unobservable and so such a modulation is likely due to the extremes of the emission cones illuminating Wind as the magnetic dipole tilts.

For a highly directional emission such as AKR, with spatially complex source regions and triggering via coupling to the dynamic magnetosphere, I can examine the temporal variability observed from each spacecraft's position to attempt to further

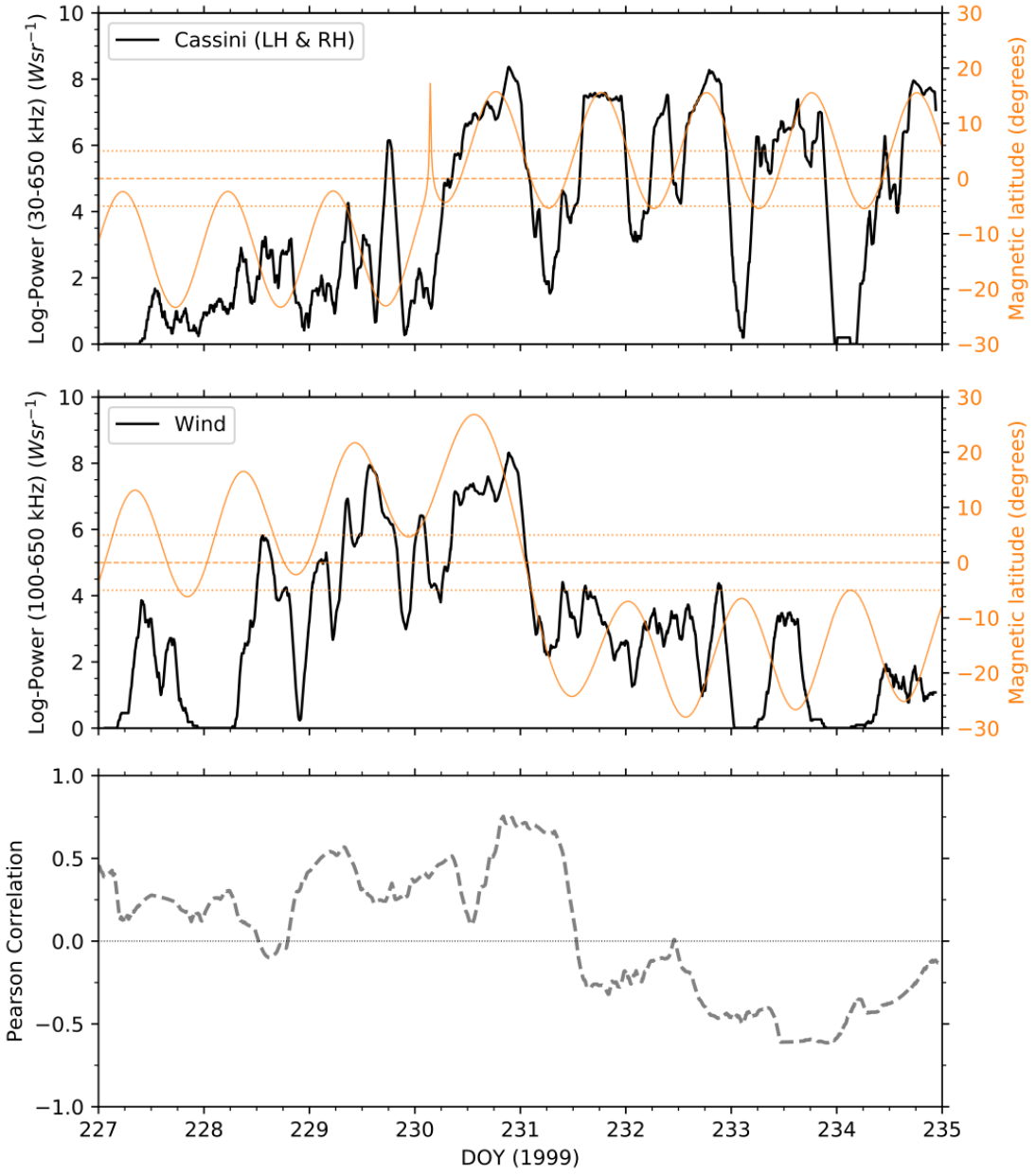

FIGURE 4.10: Comparative time series of AKR power for the eight days (DOY 227-235) that comprise Wind's first perigee, taking it across the nightside. The top panel shows the Cassini integrated power (30-650 kHz) averaged over a moving 3 hour window and including both LH and RH emission. The middle panel shows the 3-hour-averaged Wind integrated power (100-650 kHz). Shown in orange on the right ordinate of both the top and middle panels is the magnetic latitude of the respective spacecraft. Also shown in the top and middle panels are lines indicating the magnetic equator and $\pm 5°$. The bottom panel shows the linear cross-correlation between the AKR power as observed by Wind and the magnetic latitude of the spacecraft, with a 24 hour moving window.

explain these diurnal modulations. Figure 4.10 shows time series of the AKR power observed by Wind and Cassini for DOY 227-235, during which Wind travelled across the nightside from the dusk to dawn sectors, crossing the magnetic equator around DOY 231. The power shown for Cassini in the top panel is for both LH and RH AKR, is integrated over the range 30-650 kHz and is averaged similarly over a 3 hour window. 3 hour averages of the Wind AKR power are shown in the middle panel, but again integrated over the range 100-650 kHz for reasons given in section 4.2.2. Although I expect some discrepancy in the magnitude of the average power for this reason, the effects of this will be negligible compared to those introduced by the viewing positions and it is preferable to compare this range to reduce the contamination from low frequencies. Given the dependence of viewing of the AKR from a particular hemisphere on the magnetic latitude as observed by Cassini and shown in figure 8 of Lamy et al. (2010), I can assume that the dominant AKR observed by a spacecraft at a magnetic latitude $|\lambda_m| > 5^\circ$ will be of the corresponding magnetic hemisphere, with little contribution from the other hemisphere if observed. Visual inspection of the AKR power from both spacecraft shows that the bursts are not only seen to be antiphased when in opposite hemispheres, but that they can also be in phase on various timescales regardless of the spacecraft position. A particularly strong example of this is seen in the peak $\sim 10^3$ Wsr^{-1} in the AKR power observed by Wind when between -20° and -30° magnetic latitude, centred on DOY 233.5, whilst Cassini sees a peak of $\sim 10^7$ Wsr^{-1} whilst close to the magnetic equator at positive latitudes.

Given the significant diurnal modulation, I can attempt to discern its origin by examining the correlation of the AKR bursting with the magnetic latitude of the observing spacecraft, here Wind. The bottom panel of figure 4.10 shows the linear cross-correlation of the AKR power with the magnetic latitude over a 24 hour moving window. While a similar analysis is performed over a 5 day window in Lamy et al. (2010), the data coverage of Wind while in an appropriate viewing position is insufficient for this. While the choice of the window size is arbitrary, this was chosen to examine correlation features on a similar timescale to the modulation in question. While the correlation fluctuates, the AKR power is mostly correlated positively with the magnetic latitude of Wind, with the correlation increasing as Wind travels to higher latitudes in the Northern magnetic hemisphere, away from the region in which the emission from either hemisphere is observable and of a comparable intensity (cf figure 8 of Lamy et al. (2010)). Once wind crosses the magnetic equator at the start of DOY 231, the AKR power becomes anti-correlated with Wind's magnetic latitude after perigee; whilst the AKR power decreases as Wind travels away from the nightside and into the dawn sector, the time series clearly shows the dominant emission from the Southern magnetic hemisphere after Wind crosses the magnetic equator. These observations are consistent with those of Cassini, which showed an anti-correlated diurnal modulation of the RH and LH AKR power, with each correlating with the magnetic latitude of the corresponding magnetic hemisphere. This was interpreted as

the result of the diurnal rocking of the AKR source region and the beaming pattern, and this is assumed to be the dominant source of the modulation observed here. On the other hand, the presence of phased bursts in observations of both spacecraft regardless of magnetic latitude is contrary to this. While AKR observations with Wind alone appear to be consistent with those of Cassini, with peak AKR power observed at extremes of the spacecraft magnetic latitude and suggesting dominance of a viewing effect, the phasing between AKR bursts observed by both spacecraft brings another new and important constraint to the origin of the diurnal modulation. While the combination of the Wind and Cassini observations here has again illustrated the value of multipoint measurements of AKR, the detailed investigation of the burst phasing is beyond the scope of this work.

4.3 Conclusion

I have described a new method of selecting AKR emission from the complex radio environment observed by Wind, using a statistical measure of the variability of radio flux across the spin-axis-aligned Z antenna during a spacecraft spin. Examination of individual spins and the flux density dynamic spectrograms during a 30 day trajectory of Wind shows that the selection is effective at removing ubiquitous solar Type III bursts from the data and isolating AKR (figures 4.1 and 4.2). Although there are limitations at lower frequencies as RFI and sources of high temporal variability from the local plasma can contaminate the selection, the selection criterion employed here is based on a simple numeric threshold, and can be readily applied to the extensive dataset of Wind. Here I applied the AKR selection to Wind data for an interval overlapping with the Earth flyby of the Cassini spacecraft. The Cassini data have previously been treated with a full GP inversion (Lamy et al., 2010), but here they provide context for the sensitivity of radio observations to the viewing position of the spacecraft. After considering the discrepancies between the viewing positions of the two spacecraft during the period (figures 4.3 and 4.4), the flux density dynamic spectrograms of the 30 day period between Wind and Cassini are compared in figure 4.5. This shows the expected reduction in observed emission as Wind traverses the dayside and is no longer illuminated by the most intense AKR sources located on the nightside. Examining the data more closely, I compare the flux density spectra of Wind observations made from a comparable region to that of Cassini for the period and find that the general characteristics of the AKR spectrum are reproduced well at frequencies $>$ 100 kHz. Figure 4.6 shows the broadening of the spectral peak at around 200 kHz in the median spectrum to higher frequencies for the most intense emission, agreeing with the accepted AKR spectrum and the previous Cassini observations.

Accounting for the aforementioned limitations, I integrate the flux densities measured by Wind between 100-650 kHz for each 3 minute sweep to represent the confident selection of AKR, covering the main frequency range and allowing a comparison with previous results from Cassini. I have accounted for the viewing geometry of AKR in the observations by averaging the integrated power measured in each one hour LT bin, shown in figure 4.7. This reproduces quantitatively the day-night asymmetry that can be seen in figure 4.5 and is again expected, with a 4 order of magnitude increase from $\sim 10^4 - 10^8$ Wsr^{-1}. This also provides confidence in the selection of AKR by this method given that it also reproduces the dawn-dusk asymmetry associated with the close correlation between the AKR source region and the auroral region in the ionosphere. Emission is selected at all local times, showing that we can observe AKR from many of Wind's various viewing positions in the magnetosphere and solar wind and shows promise for future studies where the selection can be applied to a larger Wind dataset and aid statistical analyses of events. I also examine in figure 4.8 the dependence of the average AKR power with the magnetic latitude of the observation. While I cannot confirm a latitudinal dependence of the AKR power for sources observed from the dayside, Wind observations made at ideal LT show general agreement with the relationship found for RH AKR observed by Cassini in the Northern magnetic hemisphere.

Using the selected integrated power I examined the temporal variability of the Wind AKR observations, confirming the presence of a diurnal modulation with a FFT analysis, shown in figure 4.9. I observe a statistically significant ($p < 10^{-5}$) peak at 24 hours for the entire period, as well as for three subsets of the data corresponding to the first perigee from DOY 228-233, the traversal of the dayside from DOY 232-251, and the second perigee from DOY 250-255. In figure 4.10 I compared in more detail the AKR power between Wind and Cassini during the first perigee of Wind, which placed it ideally to observe intrinsic AKR modulation over a few days. A linear cross-correlation between the Wind AKR power and the magnetic latitude of the spacecraft showed that the AKR is generally correlated in the Northern magnetic hemisphere and then anti-correlated as it crosses into the Southern, lending weight to the visibility of the AKR emission cone in each hemisphere as the predominant source of the diurnal modulation. On the contrary, however, AKR bursts are also observed that are in phase whilst the spacecraft are in separate magnetic hemispheres, although only a short time period is shown here and further inference is out of the scope of the study. Given the ease of masking the Wind data with this technique, longer-term studies of diurnal and semi-diurnal modulations can be conducted with Wind alone, which has > 2 decades of observations from a variety of positions. With the verification of the empirical selection as seen here, statistical analyses can also be conducted between resulting AKR dataset and lists of substorm onsets that cover decades and are complimentary to Wind's lifetime.

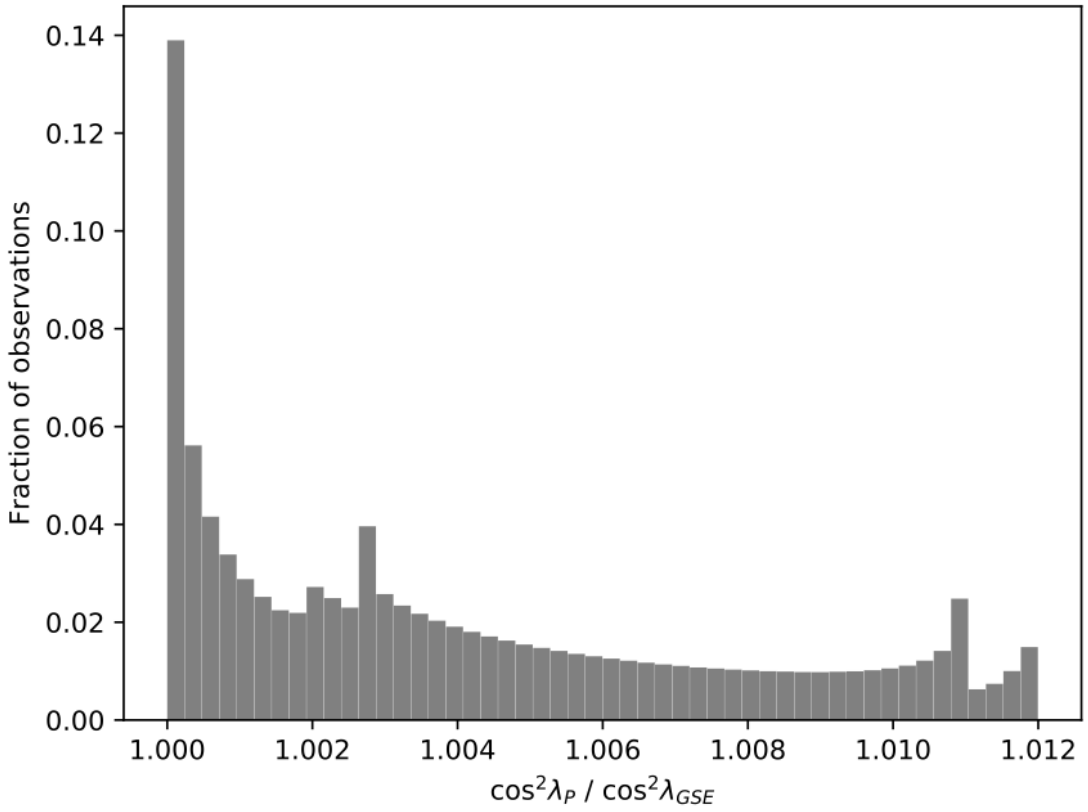

FIGURE 4.11: Statistical characterisation of the error implicit in the assumption of Earth's center as the direction of the AKR source. Presented data relates only to the 30 day period studied here, and shows the fraction of Wind observations that would be affected by a given error factor. $\cos^2 \lambda_{GSE}$ is the term used in equation 3.2, while $\cos^2 \lambda_P$ is the term calculated using the apparent latitude of Wind with respect to geographic poles.

4.4 Errors Due to Assumption of Source Direction

As described in section 3.1.4, we do not have an exact indicator of the AKR emission hemisphere and expect that both LH and RH AKR will illuminate Wind during certain times, dependent on its viewing position. AKR source regions are known to be confined to nightside LT along high latitude magnetic field lines which allows the geographic or magnetic poles to be used as a reasonable assumption for the source center, which pole being dependent on the spacecraft magnetic latitude, for example. For a generally applicable selection algorithm, however, it is favourable to apply a consistent assumption to all observations. Figure 4.11 shows the distribution of errors introduced by using the Earth's center over the poles. λ_P, the apparent latitude of Wind when translating the ecliptic plane to either geographic pole, gives a proxy of the geographic pole direction from Wind. From equation 3.2, I compare the ratio $\frac{\cos^2 \lambda_P}{\cos^2 \lambda_{GSE}}$ to characterise the implicit error introduced here and find that the maximum value in the distribution is 1.2%.

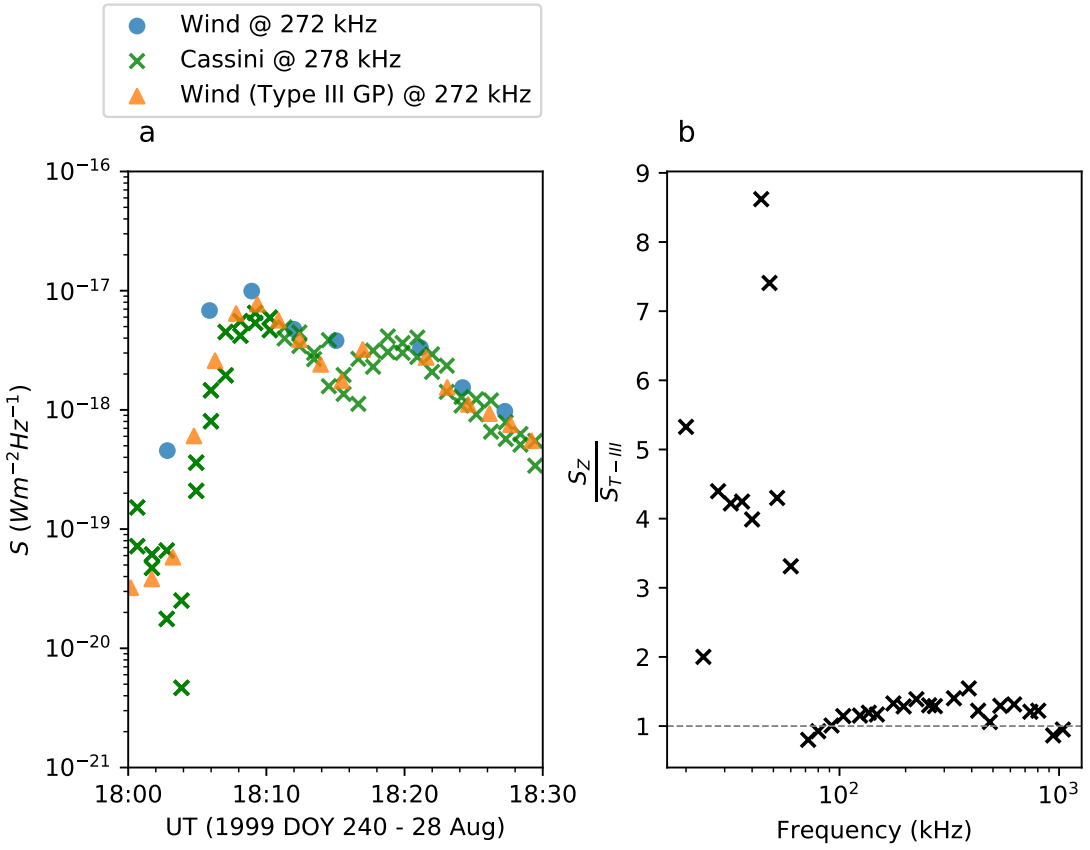

FIGURE 4.12: Comparing flux densities of a single Type III burst at comparable frequency channels between spacecraft (left) and the resulting ratio between the two datasets from Wind, using the peak flux spectra from the Type III burst (right). Included in the left panel are data derived from Wind using the calibration method described in section 3.1.4 (S_Z, blue circles), modified to account for the change in radio source (see 4.5), data from Cassini using a GP inversion that treats Type III bursts (green crosses) and data from Wind using a similarly modified GP inversion at the original 90 s resolution of the frequency channel (S_{T-III}), orange triangles). The panel on the right shows the ratio $\frac{S_Z}{S_{T-III}}$, where each data point is given by the ratio of the peak flux between datasets during DOY 240 18:00-18:30. The grey, horizontal, dashed line is at unity.

4.5 Cross-Checking Flux Densities Using Type III Bursts

As mentioned in section 3.1.4 I initially compared the flux density resulting from equation 3.2, derived from the linear Z antenna, with those from a full GP inversion. Although the scaling factor that results from this work is not applied, I retain the results here as a point of interest, given the observed discrepancies. I have access to results from a GP inversion that assumes the source parameters of a solar radio Type III burst (namely that they are unpolarised) and utilises the Wind/WAVES system such that the total flux density is retrieved. The S' antenna, used explicitly to retrieve the degree of circular polarisation, is thus ignored in this inversion. To compare the fluxes from the Z antenna to GP fluxes, I must omit the $\cos^2 \lambda$ term from equation 3.2

to reflect the fact that the source direction is no longer assumed to be at Earth, and the Type III burst source region is sufficiently far enough away and close to the ecliptic plane that the Z antenna is always perpendicular to the emission. Explicitly, the Z antenna is pre-calibrated using

$$P_Z = \frac{1}{2} G S_Z \tag{4.2}$$

for the observations presented in this section. Here G is the gain as used in equation 3.2 and given in equation 3.3. The fluxes from the Type III inversion with Wind are derived using a calibration from Zarka et al. (2004), which has since been corrected by a factor 2 by Zaslavsky et al. (2011) and is accounted for here. The fluxes from the Type III inversion with Cassini are similarly derived but have already accounted for this factor (Cecconi et al., 2017).

Figure 4.12 shows the comparison of calibrated flux densities for an example of a Type III burst observed by Wind and Cassini during 1999 DOY 240. The Wind observations are given at different resolutions; the data used here are averaged over the 3 minute sweep, while the original resolution of each frequency channel is retained in the data from the Type III GP inversion with Wind. The peak of the primary Type III burst at 272 kHz is seen close to 18:10 UT in this example, and while good agreement is seen between the Type III GP inversions with Cassini and Wind, the Z antenna-calibrated data have an approximately constant offset following the peak. By defining the bounding UT of the Type III burst as well as its frequency limits following visual examination of the relevant dynamic spectrogram, I can track the peak flux of the Type III burst for each set of fluxes and produce a spectrum of the ratio $\frac{S_Z}{S_{T-III}}$, where S_Z is the flux from equation 4.2 and S_{T-III} is the flux from the Type III GP inversion with Wind. The example in figure 4.12 shows the entire Wind/WAVES RAD1 spectrum, including the lower frequencies that the Type III emission does not reach and showing the discrepancy between the two data below $\sim$ 70 kHz. By compiling the spectra of $\frac{S_Z}{S_{T-III}}$ for multiple Type III bursts selected in this way, I can derive an average cross-calibration spectrum with which to scale AKR fluxes from equation 3.2, giving a better representation of the true intensity of the radio source and allowing a proper comparison between Wind/WAVES fluxes here and those from Cassini/RPWS. While I do not explore it in detail, it is interesting to note that the Cassini observations, derived with an inversion adapted to AKR sources, sees good agreement with the Wind observations from the Type III inversion.

Figure 4.13 shows the mean $\frac{S_Z}{S_{T-III}}$ spectrum from a set of 19 Type III bursts. The uncertainties on the cross-calibration spectrum are given by the standard error of the mean, and show the better-constrained values at frequencies $>$ 50 kHz for which the majority of the selected Type III bursts are emitting. $\frac{S_Z}{S_{T-III}}$ tends to increase at the lowest frequencies, with the most pronounced increase seen at 20 kHz. This is likely due to the inclusion of spurious emission from the visual examination, as well as the limited number of Type III bursts (7) that were emitting at this frequency. The fact that

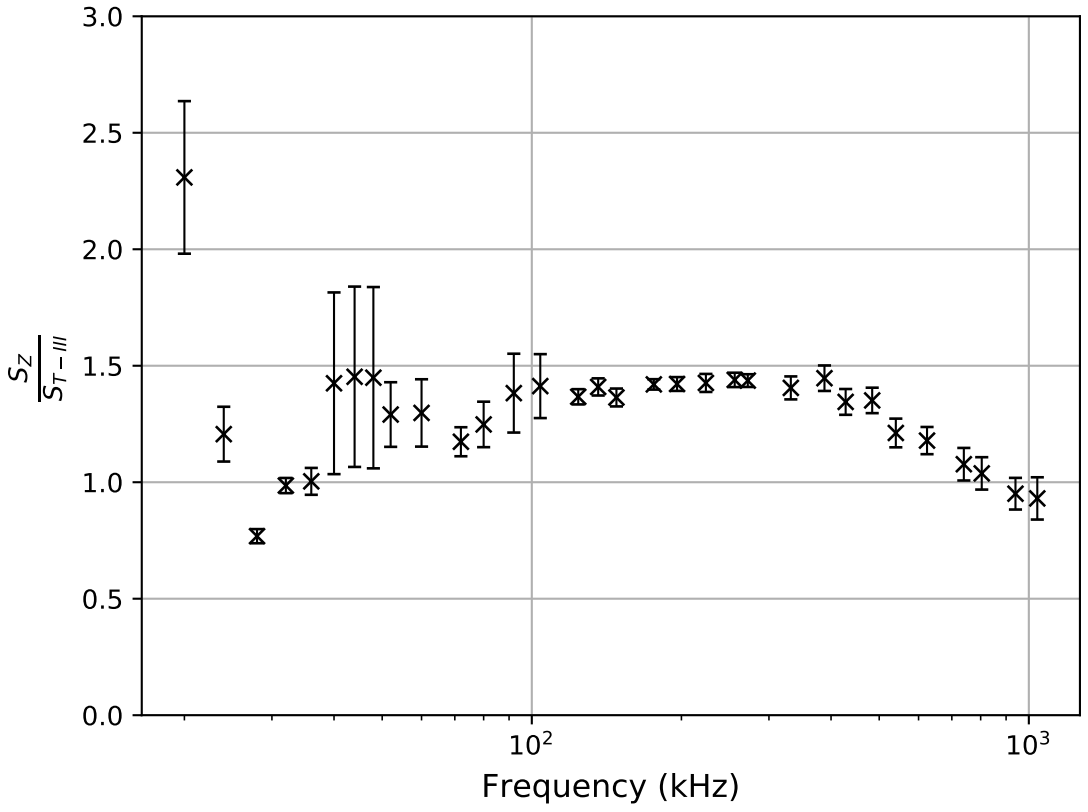

FIGURE 4.13: Spectrum of the average ratio between peak flux spectra for a total of 19 Type III bursts. As detailed in section 4.5, each Type III example is described by a start and end time as well as its frequency limits. A spectrum is formed for each example by taking the ratio of the peak fluxes in each channel between the bounding times (see text). The average spectrum shows the mean of the ratios of each frequency channel, with error bars showing the standard error of the mean.

the linear Z antenna observes calibrated fluxes larger than those from two independent sets of observations using GP inversions with Wind and Cassini is puzzling, but I do not explore the details for this here.

4.6 Threshold Justification

Figure 4.14 shows the distribution of σ_Z values observed at 272 kHz and during the 30 day period studied here. This frequency channel was chosen to present as it is a good representation of the typical peak frequency of the AKR spectrum. Shown in the plot is the value used to select AKR data as described in section 4.1.1; at values lower than this the majority of the emission is found, with a strong Gaussian profile centred roughly on $10^{-1.5}$ representing the majority of other emission such as Type III bursts and background sources, while at values higher than 10^{-1} a second population is seen that contains AKR as well as low frequency contaminants. While determining the exact σ_Z distribution of AKR observations for the entire spectral range is out of the

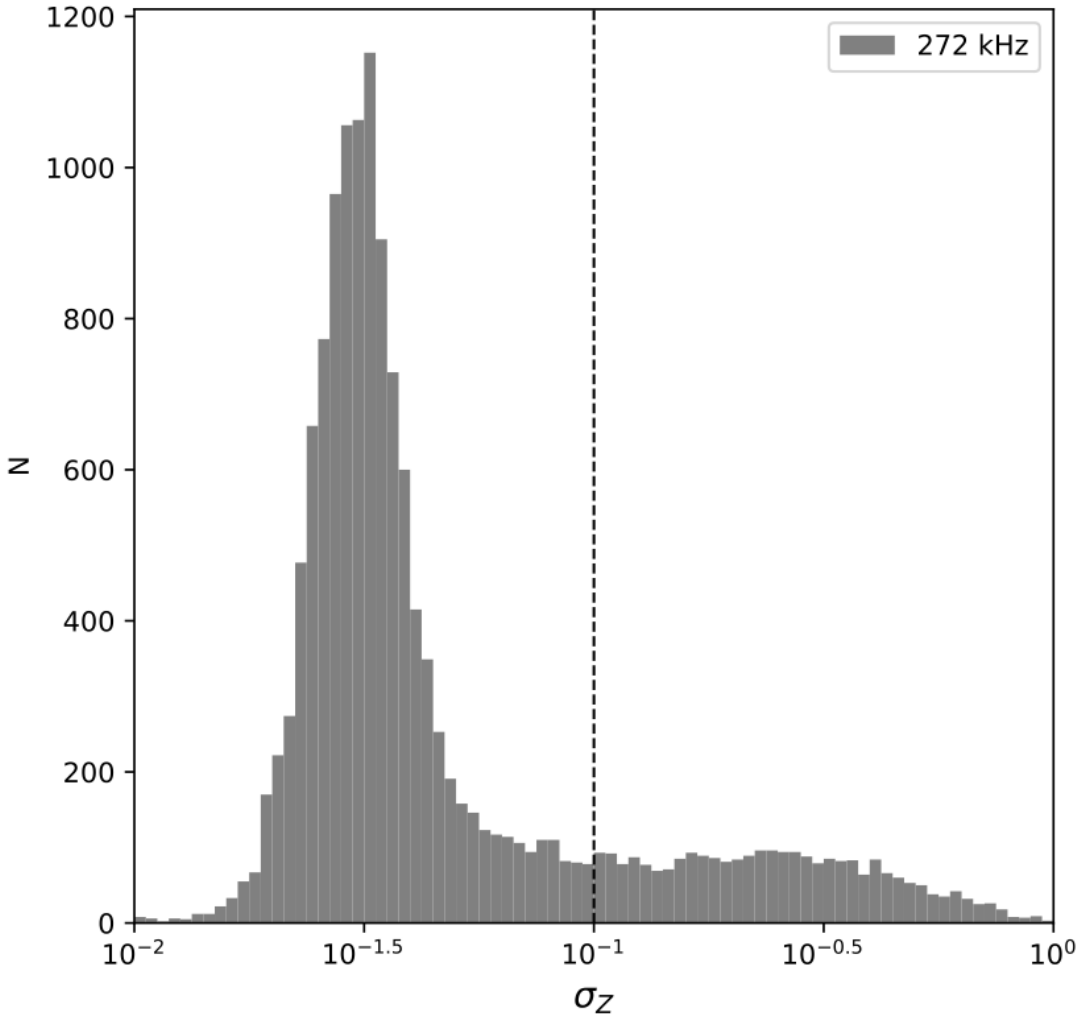

FIGURE 4.14: Distribution of σ_Z values for all observations made at 272 kHz during the 30 day period studied here. The black, vertical dashed line shows the value of the threshold ($\sigma_Z \geq 0.1$) chosen to select AKR data.

scope of this work, examinations of this metric at other frequencies exhibit similar distributions that lend weight to this choice of the threshold.

4.7 AKR Power Distributions with Spacecraft LT

Figure 4.15 shows the distribution of integrated power observations (100-650 kHz) for each LT bin used to compute the average values for figure 4.7. From the top and bottom rows, corresponding mostly to LT sectors that Wind travelled through on two, separate occasions, evidence can be seen that suggests that the distributions are comprised of two separate events of AKR emission which differ in intensity, whether due to intrinsic differences due to the current state of the magnetosphere or other effects. Some of the bins exhibit two distributions that are separated by 6 orders of

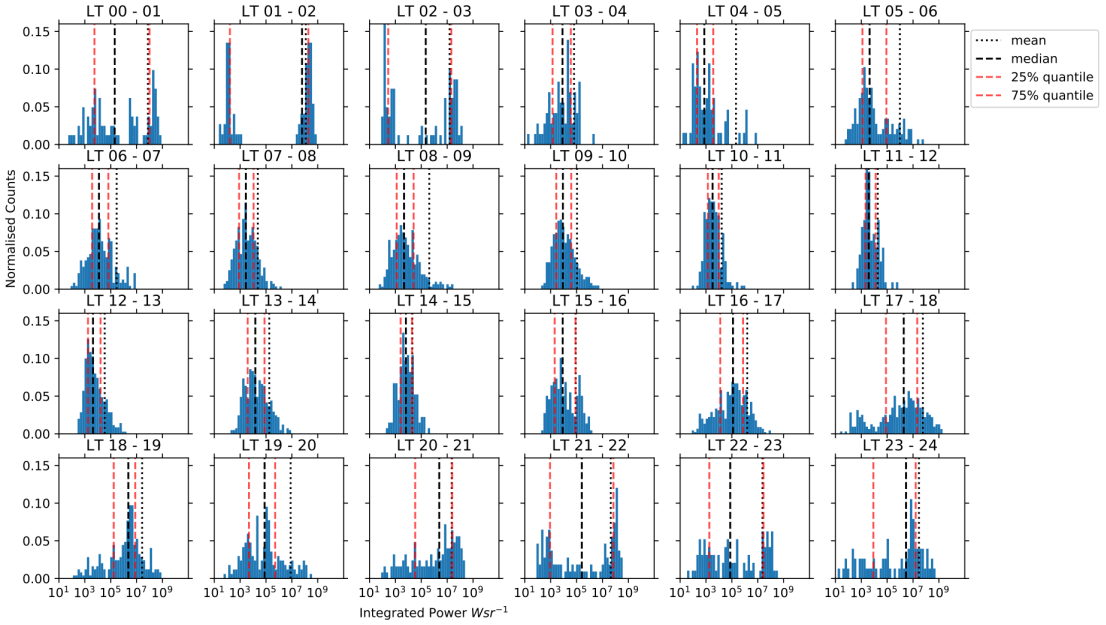

FIGURE 4.15: Normalised histograms showing the distribution of log integrated power in each 1 hour LT bin used to create figure 4.7. Each histogram has black dashed and red dashed vertical lines to represent the median and lower and upper quartiles of the distributions, while the black dotted line shows the mean.

magnitude in some cases (eg 01-02 LT), as well as non-Gaussian distributions (eg 08-09 LT). Applying the selection technique over a longer period will remove some of these local effects and better characterise the statistical AKR power distribution with LT. Taking the mean of the distributions here gives an average that is skewed towards higher values and represents more closely the larger extreme of the total distribution of data, as seen by its position with respect to the 75% quantile in most panels of figure 4.15. The median of these distributions would be a more statistically rigorous measure of the average. Here, however, where the aim is to demonstrate the empirical selection of AKR data and not to rigorously define the average AKR power of these observations with LT, the mean is sufficient.

Chapter 5

Statistical Analysis of the AKR Response During Substorms

This chapter is based on results presented in the following publication: *Waters, J. E., Jackman, C. M., Whiter, D. K., Forsyth, C., Fogg, A. R., Lamy, L., Cecconi, B., Bonnin, X., Issautier, K.; Empirical Selection of Auroral Kilometric Radiation During a Multipoint Remote Observation With Wind and Cassini; JGR: Space Physics; 126(10); doi:10.1029/2021JA029425, 2021*

This work was conducted entirely by the author, although significant discussion was held with colleagues. In particular, C.M. Jackman, D.K. Whiter, C. Forsyth and L. Lamy contributed significantly to discussion regarding scientific interpretation and analysis of data.

5.1 Introduction

Auroral Kilometric Radiation (AKR) is non-thermal radio emission generated within a plasma cavity that is extended longitudinally about the terrestrial nightside at high magnetic latitudes (Gurnett, 1974; Calvert, 1981; Mutel et al., 2008; Yearby and Pickett, 2022), with the emission frequency being very close (typically within 1-2%) to the electron gyrofrequency (Wu and Lee, 1979) and correlating with discrete auroral activity. AKR is described in more detail in section 2.7. As well as auroral brightenings, AKR is also coincident with many of the other observed processes in the magnetosphere that occur during substorms and times of disturbance, such as high velocity flows and geosynchronous particle injections in the magnetotail and increased ground magnetic activity (Fairfield et al., 1999). The activation of a lower frequency AKR source implies that the source region has extended to higher altitudes along the field line, and as such is a proxy for the structure of the auroral acceleration

region, which has been confirmed by in-situ measurements of the source region (Ergun et al., 1998). As mentioned in section 2.6, the auroral acceleration region is integral to understanding magnetosphere-ionosphere coupling, and AKR observations have been used to infer its changing morphology during times of disturbance (Morioka et al., 2010).

Substorms are space weather events that are characterised by various plasma dynamics under changing magnetospheric configurations and orientations of the interplanetary magnetic field (IMF). Fundamentally, they result from the transfer of energy when the dayside and nightside reconnection rates are imbalanced, this is described in section 2.4. Related to the explosive release of energy in the magnetotail, as the cross-tail current is diverted to the ionosphere and nightside reconnection occurs, is the intensification and changes to the spectra of AKR. This is quantified in studies of the AKR power and the AE index (Voots et al., 1977; Kaiser and Alexander, 1977a), field-aligned currents (Green et al., 1982) and electron precipitation (Imhof et al., 2000). Global observations of the auroral oval at substorm onset have also provided an insight to coincident AKR enhancement (Liou et al., 2000). As well as this, AKR intensifications are typically accompanied by spectral extensions, notably to lower frequencies (Hanasz et al., 2001). These low frequency extensions (LFEs) occur close to substorm onset, and have been studied by the Polar plasma wave instrumentation (PWI) in conjunction with ground and in-situ measurements of the magnetic field, electron populations and other plasma parameters (Morioka et al., 2007, 2010). The spectral changes observed in AKR during these events has allowed, by proxy, the evolution of the auroral acceleration region to be inferred; extending to higher altitudes as source regions of low frequency AKR become active along high latitude magnetic field lines (Morioka et al., 2012). While these studies of AKR have allowed for characterisation of this important region of the magnetosphere they are typically conducted over a limited number of events.

With the selection technique detailed in chapter 4, there is now an opportunity to significantly extend the study of the link between substorms and AKR due to the availability of years of high fidelity data from the Wind spacecraft. Accounting for viewing limitations, 10 years of calibrated AKR observations from 1995-2004 are now able to be examined, with properties of the emission itself and spectral features available (Waters et al., 2021a; Fogg et al., 2021). This allows coincident lists of substorm events, derived from various observational signatures and that also cover decadal timespans, to be compared with the AKR observations. With the novel data available, I examine the AKR observations during the magnetosphere-ionosphere coupling timeline of substorms as defined by the aforementioned lists. In this way I aim to characterise the average AKR response with respect to other changes within the magnetosphere, as well as examine how both the intensity and spectral parameters of AKR change with the size of the substorm.

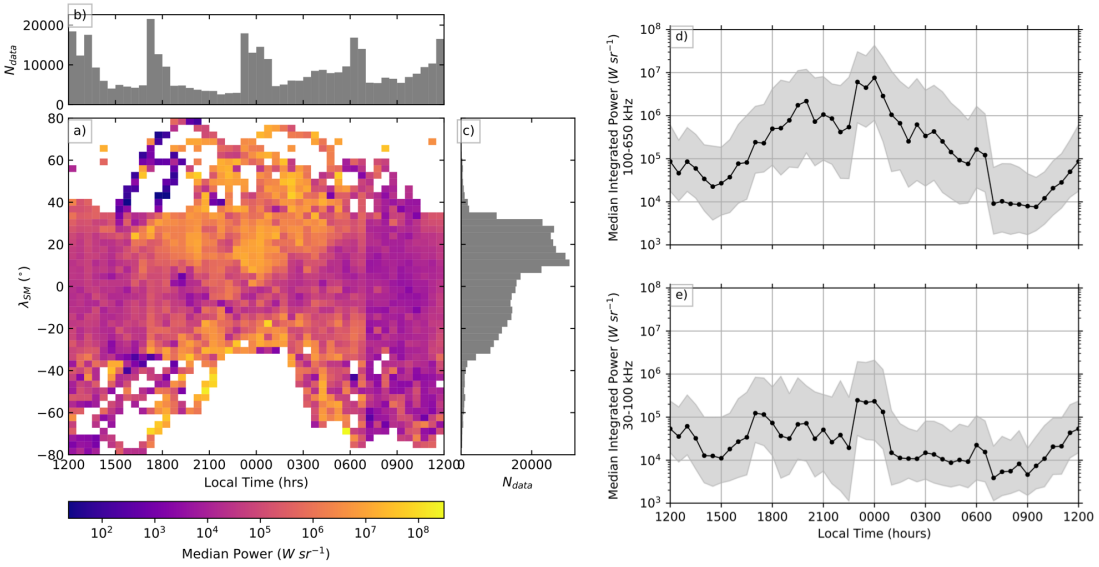

FIGURE 5.1: Average AKR power (a) for viewing positions of Wind from 1995-2004 inclusive, with marginal distributions of spacecraft LT (b) and magnetic latitude (λ_{SM}) (c) of the observations shown. Panels (d) and (e) show the median AKR power for frequency ranges that represent the higher frequency (HF 100-650 kHz) and lower frequency (LF 30-100 kHz) components of AKR, respectively, with the upper and lower quartiles shown.

In section 5.2 I introduce the AKR data used here, giving the important context of spacecraft viewing to the 10 years of observations, as well as introducing the various lists of substorm events and their associated observational signature. Section 5.3 details the analysis of the AKR power with the substorm timeline as defined by each of these lists and the interpretation of the results, while section 5.4 concerns the analysis and interpretation of the spectral parameters of AKR, providing insight to the typical evolution of the auroral acceleration region. In section 5.5 I conclude this work with a summary of the analysis conducted and their primary results.

5.2 Data and Methods

5.2.1 Wind Radio Measurements and AKR Bursts

For this statistical study I use 10 years of radio data from the Wind spacecraft, covering the interval from 1995-2004 inclusive. During this time, Wind explored all local times (LT) at a range of radial distances and latitudes which allowed it to probe the solar wind and various magnetospheric regions *in-situ* in order to tackle different science objectives (Pelton and Allahdadi, 2015). From mid-2004 onwards, Wind reached what is to be its final destination, as it entered a Lissajou orbit about the first Lagrangian point L1. For the first 5 years of observations, from ∼1995-2000, Wind

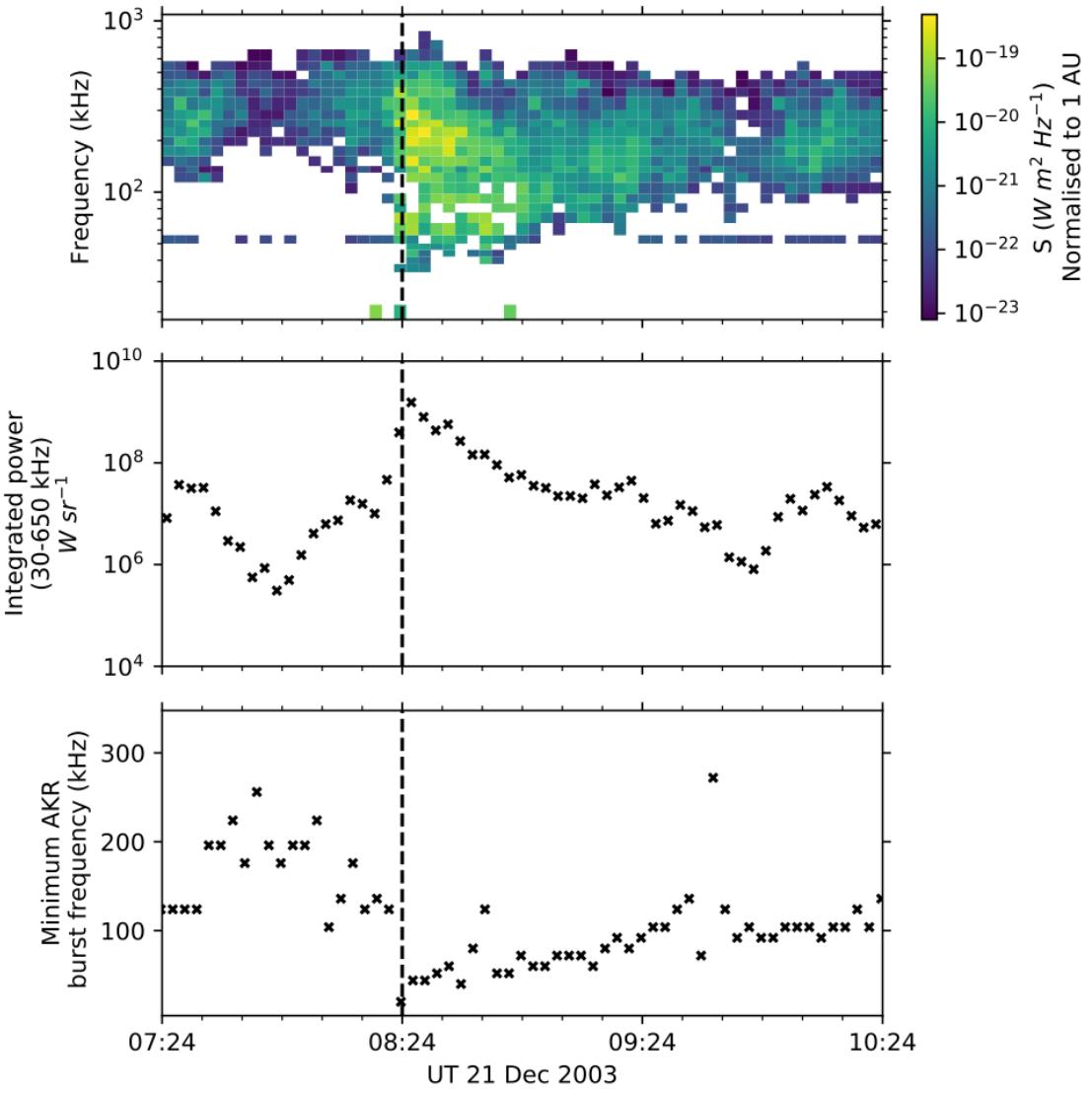

FIGURE 5.2: AKR response during a substorm onset at 08:24 UT on 21 December 2003, as defined by the SOPHIE algorithm with 90% expansion percentile threshold (EPT - see section 5.2.2). The top panel shows the frequency-time flux density dynamic spectrogram from Wind/WAVES, following the selection of AKR outlined in (Waters et al., 2021a), for a 3 hour period about onset, which is indicated by the black dashed line. The middle panel shows the corresponding observed radio power, here integrated between 30-650 kHz. The bottom panel shows the minimum frequency bound of the AKR burst determined by Fogg et al. (2021).

observed most often from dayside LTs during precessing orbits with dayside apogees. Near 2000 Wind was sent into a trajectory that took it to radial distances of 250 R_E (1 $R_E = 6371$ km (1 Earth radius)) on the dawn and dusk flanks. From mid-2003 to mid-2004, Wind explored the nightside magnetosphere, being placed in a trajectory that sent it downtail to the Lagrangian point L2. The nightside location of the source regions and the highly anisotropic beaming of the emission has consequences for the viewing of AKR for a remote sensing spacecraft such as Wind, and so the spacecraft position at the time of substorm onset must be considered. The RAD1 receiver of the Wind/WAVES instrument takes a variable number of samples (between 1-4) of 32 frequency channels, between 20-1040 kHz, over a $\sim$3 minute sweep cycle (Bougeret et al., 1995). Figure 5.1 shows the median AKR power observed during 1995-2004, binned by the LT and magnetic latitude of Wind during the sweep cycle, as well as the marginal distributions that show the number of sweeps made in each LT and latitude bin respectively. Figure 5.1a shows the median power integrated over typical AKR frequencies, namely 30-650 kHz here. Observations are binned in a 48×50 grid, with 0.5 hour wide LT bins and 3.2° wide latitude bins. Data are shown such that observations made in the ecliptic plane at midnight are in the centre of the plot. Note that these distributions do not show the complete distribution of Wind viewing positions, but only those in which AKR was detected.

The LT distribution in Figure 5.1b shows increases around noon (12:00 hours), midnight (00:00 hours), dawn (06:00 hours) and dusk (18:00 hours). This is due primarily to the varying orbital trajectory of Wind for the 10 years, and represent the excursions to Lagrangian points as mentioned. As the marginal distributions in Figure 5.1 show only AKR observations from Wind, it does not show the complete range of viewing positions, namely those from which AKR was not observed due to source inactivity or the distance of the spacecraft from the beamed emission. The relative fraction of measurements for which AKR is observed is much lower on the dayside than on the nightside. The strongest AKR sources are known to be localised to the nightside magnetosphere; this is reflected in Figure 5.1a, which shows a significant decrease in observed AKR power between $\sim$06:00 to 18:00 hours LT. There is a sharp decrease at all latitudes in the median AKR power close to 06:00 hours LT which is likely due to AKR sources preferentially found towards dusk, in the premidnight LT sector. If AKR sources activate more readily in a wider range of premidnight compared to postmidnight LTs, the decrease in AKR power will be smoother in this region.

The latitudinal distribution of the Wind AKR observations, shown in Figure 5.1c, gives the latitude of the spacecraft in solar magnetic coordinates (λ_{SM}, with positive values aligned with the magnetic pole in the Northern hemisphere), and shows the general bias towards measurements made in the Northern magnetic hemisphere. The majority of observations are made between -40° to 40°, while Wind infrequently reached higher

latitudes to a maximum magnitude of 80°. The appearance of the average data at higher latitudes is due to slow, sparse passes of the spacecraft through these regions. The general trend in the AKR power shows an average increase when viewed from higher latitudes in either hemisphere, with decreased power and dependency on latitude in dayside LTs; agreeing with previous observations (Lamy et al., 2010; Waters et al., 2021a). It should be noted however, that the majority of these observations are made at relatively low latitudes when compared with other studies, that may constrain the viewing of lower latitude or higher altitude AKR sources given recent models of tangent plane beaming (Mutel et al., 2008; Schreiber et al., 2017).

Figures 5.1d and e show the median AKR integrated power again binned in LT, after Fogg et al. (2021), extended to cover the relevant interval 1995-2004. This corroborates their results, with a similar decrease in power seen as Wind observes from dayside LT, out of view of the primary emission from the nightside sources. For this work, where I focus on comparison of AKR bursts with substorm lists, I focus on intervals where Wind was observing from local times between 1800 to 0600 hr LT as these represent the best viewing of the AKR sources.

The data in Figure 5.1 is derived from 3 minute resolution flux density data from Wind, processed with a calibration specific to AKR observations and an automatic selection of data based on the change in intensity across the Wind spin period (Waters et al., 2021a). Measurements are given in 32 frequency channels between 20 and 1040 kHz. Note that the 52 kHz channel is often selected but can contain emission not associated with AKR; I replace these flux densities with interpolated values of neighbouring channels in the following analysis. This selection allows me to explore the AKR intensity on a statistical basis, given the breadth of Wind data available and simple applicability of the selection algorithm, as well as the coincidence of low-frequency extensions with other magnetospheric phenomena. This can be done with the flux densities themselves, but also by integrating the power over particular spectral ranges to further characterise the AKR. Fogg et al. (2021) has recently refined the AKR selection, output by Waters et al. (2021a), to formulate a list of discrete AKR bursts. This process includes steps based on *a priori* knowledge of the AKR morphology, as seen in dynamic spectrograms, namely that low frequency emission (below 100 kHz) is generally accompanied by AKR at higher frequencies. Morioka et al. (2007) describe the lower frequency, higher altitude AKR sources as existing between 6000-12000 km. The lower of these altitudes corresponds to an upper bound of ∼200 kHz for the lower frequency AKR range. Here, a conservative estimate of 100 kHz is chosen to constrain the behaviour of the highest altitude sources. As well as start and end times of clusters of observed AKR emission, or bursts, the output of this processing also parameterises each burst for spectral information, namely its upper and lower frequency bounds.

Figure 5.2 shows an example of the Wind/WAVES data used in this work; a substorm onset from the SOPHIE algorithm is shown (see section 5.2.2), with radio data from 60 minutes before onset to 120 minutes after onset. The top and middle panels show AKR-calibrated flux densities and emitted power per unit solid angle respectively, from Waters et al. (2021a), while the bottom panel shows the minimum frequency bound of the burst associated with the example onset, from Fogg et al. (2021) The frequency-time flux density dynamic spectrogram in the top panel of Figure 5.2 shows AKR emission predominantly between ∼200-500 kHz before onset. Intensifications of at least 2 orders of magnitude are then seen at most frequencies recorded between this range, while channels sampled below 200 kHz activate as the AKR extends to lower frequencies. Note that the AKR flux densities used here are normalised to 1 AU to account for the various distances at which the observations were made (Waters et al., 2021a). While the spectral information is lost, the middle panel of Figure 5.2 shows the radio power integrated between 30-650 kHz, which characterises the AKR response temporally and provides an informative metric over which to compile substorm events. The bottom panel of Figure 5.2 shows the minimum observed frequency of the AKR burst of Fogg et al. (2021) associated with this substorm, used as a proxy for the average upper altitude bound of the AKR source region.

5.2.2 Substorm Lists

As mentioned in section 2.4 substorms have signatures throughout the magnetosphere-ionosphere system, such as dipolarisation and bursty bulk flows (BBF) in the magnetotail and strengthening of the westward electrojet in the high latitude ionosphere. They have been characterised by a number of these observational phenomena, initially by visual examination (e.g., the extensive all-sky camera observations historically used by Akasofu (1964) to describe the main auroral evolution of the substorm) and later with processing of extensive datasets made available by spacecraft observations or large networks of ground magnetometers. These efforts have created a variety of lists of substorm onsets, as defined by these various signatures. Some of these have been retrospectively applied to long-standing observational datasets, and as such have created lists that span a comparable time range to that of the Wind observations.

In this work, I consider lists of onsets derived from a single observational proxy. One such observational proxy is derived from the global SuperMAG network of ground magnetometers which forms the SML index (Newell and Gjerloev, 2011), an analogue to the historic AL index (Davis and Sugiura, 1966), which measures the strength of the Westward electrojet. The Substorm Phases from Indices of the Electrojets (SOPHIE) (Forsyth et al., 2015) algorithm analyses the SML index to select times of significant decreases of the index relative to the considered timespan. This algorithm also uses a

free statistical parameter, as only events with decreasing rates of change in SML greater than that given by the expansion percentile threshold (EPT), or a given quantile over the included SML data (Forsyth et al., 2015). In this way, higher EPT values generate a list of substorms with a larger response in the Westward electrojet. Forsyth et al. (2015) published three event lists, with EPT values of 50%, 75% and 90%. By including *a priori* knowledge of the observed structure of a substorm and the average duration, further steps are performed to produce a list of the start times of substorm phases, namely the growth, expansion and recovery phases. The published lists each cover the period from 1995-2014. Some expansion phases follow recovery phases in the SOPHIE output; these are attributed to intensifications of the substorm as opposed to an initial onset, and are removed from our analysis, where I instead focus only on substorms which have growth, expansion onset and recovery phases in order. Flagged expansion phase onsets, where changes in the SML are similar to changes in SMU and thus may be instead attributed to steady magnetospheric convection (SMC), are also removed.

The list by Borovsky and Yakymenko (2017) uses measurements of the specific entropy of the electrons in the nightside dipolar region, made by the SOPA instruments onboard the LANL spacecraft in geosynchronous orbit, to determine whether an injected population due to substorm onset is present. This list is hereafter referred to as the LANL list. A specific entropy of the electron population attributed to the substorm injection is calculated for each of the spacecraft, with a 30 minute resolution. Measurements from all the spacecraft are compiled, and the occurrence of a substorm is determined when the minimum specific entropy across all spacecraft decreases by a fixed threshold for recurrent timesteps. As determined by the identification scheme, the minimum time between substorm injections is 60 minutes. As the measurements are derived from multiple geosynchronous spacecraft that are not necessarily near local midnight, the onset times are subject to a 0-30 minute uncertainty due to the time taken for the substorm-injected population to drift to the position of the spacecraft. The published list covers the period from 1989-2007.

McPherron and Chu (2018) published a list that uses ground magnetometers at mid-latitudes ($|\lambda| < 50^\circ$) to determine substorm onset, using a typical signature in both the Northward and Eastward components of the magnetic field to derive the mid-latitude positive bay (MPB) index. McPherron and Chu (2018) use a statistical threshold to define a potential pulse due to substorm, prior to further processing to eliminate short or weak events.

Each of the lists used in this work are represented in Figure 5.3, where each list has been used to perform a superposed epoch analysis of the southward component of the interplanetary magnetic field (IMF) from OMNI, as well as the SML index derived from the SuperMAG network of gound magnetometers, both at 1 minute resolution. The median of the respective parameters is computed across 3 minute wide bins.

Substorm expansion phase onset typically follows a significant period of southward IMF ($B_Z < 0$), as magnetic flux is loaded into the nightside magnetosphere via dayside reconnection and convection across the polar cap. This is seen prior to onset for each of the included lists, which see southward IMF for an hour prior to onset; SOPHIE lists are displayed with their EPT values in percentages.

The average SML profile from the SOPHIE 75% and MPB lists are comparable in magnitude, with minimum deviations in SML of between -250 to -150 nT. The same is true for the SOPHIE 90% and LANL lists with minimum deviations between -400 to -300 nT. As such, the selection criteria for these latter lists tend to favour larger substorm events. The SOPHIE lists show the effect of using the rate of change in SML as a threshold for event selection, as SML begins to decrease sharply before the epoch. While the SML response from the LANL event list begins to decrease more than 40 minutes before onset, falling gradually compared to the other lists, this is due to the coarse resolution of the event list. Explicitly, the coarse resolution here refers to the minimum 60 minute time between identified substorm onsets, as well as the calculation of the specific entropy of injected electrons at 30 minute timesteps. Given that the timescale for substorm dynamics during the expansion phase is around 20 minutes, the resolution of the LANL identification scheme could affect the response of AKR power during substorm onset, when averaging over many events, and introduce ambiguity. This effect is particularly seen in figure 5.3, where the most negative IMF B_Z period occurs much earlier than for other lists, and both the IMF B_Z and the SML index have a smoother time profile for the LANL lists than others. Although the effect of the list resolution has an effect on the IMF B_z and SML profiles of figure 5.3, a potential physical explanation is given here. The AKR power could increase prior to onset due to the injection of an electron population that reaches the auroral acceleration region and has energy enough to ignite new AKR sources or strengthen existing ones, but not enough to register the step change in specific entropy needed to indicate a substorm by the method used for the LANL list.

The median reponse of the IMF B_Z shows the comparative magnitude of the events that are retained by the respective event selection; those with more negative B_Z prior to onset are assumed to produce a greater disturbance within the magnetosphere as this allows for longer periods of ideal IMF conditions to provide magnetic flux to the magnetotail via dayside reconnection. Comparing the median B_Z from the SOPHIE 90% list with that from the LANL list, for example, which have minimum B_Z of between -2.5 to -2.0 nT, suggests that these lists contain larger events. Given that the LANL event list is based on particle injections at geosynchronous orbit, for an event to be retained it requires a substorm of a magnitude that will allow the Earthward-travelling electron population to reach a distance of at least 6 R_E. It can be assumed that not all substorms will be of the energy to meet this criteria, and so the comparison between the LANL and the SOPHIE 90% event lists is warranted given

		Substorm list			
		SOPHIE 75% initial onset[a]	SOPHIE 90% initial onsets[a]	LANL[b]	MPB[c]
Wind LT range	1800 - 2100	470	295	283	1038
	2100 - 0000	471	409	378	1008
	0000 - 0300	647	491	438	1405
	0300 - 0600	974	723	618	2127
	2000 - 0400	1428	1114	1027	3011

TABLE 5.1: Total number of substorm onsets from each event list used in the superposed epoch analyses for each of the LT ranges used to account for Wind viewing. [a]Forsyth et al. (2015). [b]Borovsky and Yakymenko (2017). [c](McPherron and Chu, 2018).

the 90% quantile threshold applied to SML deflections in the SOPHIE algorithm. Other lists show a more pronounced minimum, with the 75% and 90% SOPHIE lists having similar profiles.

Figure 5.3 also shows the influence of using the different observational proxies to define onset and encapsulates the various temporal uncertainties inherent in each dataset. This is important when interpreting the results of similar analyses performed on the AKR power and other features. Due to the various types of observation and methods of determining substorm onset used here, each superposed epoch analysis is performed over a different number of substorm onsets. AKR has been observed to have a transient spectral response at low frequencies at substorm onset, and correlates with the historic AE index (Morioka et al., 2007, 2010; Voots et al., 1977). With the breadth of AKR data now available from Wind, I explore the extent to which AKR can be used as a similar metric for the onset of substorms, and how the AKR emission relates to the substorm timeline. For section 5.3 I assess the AKR power with respect to each of the aforementioned lists.

5.3 Substorm Timeline

Intensifications of AKR are known to coincide with auroral brightenings; it is expected that the average apparent power of the AKR will increase around substorm onset as the auroral oval expands and becomes brighter, signifying the presence of a substorm-injected electron population which subsequently lead to the generation of AKR. Integrating the AKR power over a particular spectral range gives a proxy of the extent of the source regions along a field line; an increase in power integrated over a given observation frequency range implies the ignition of AKR source regions within an altitude range given by the corresponding electron gyrofrequencies.

With an appropriate list of substorm onsets, such that Wind is an appropriate viewing position, a superposed epoch analysis can be performed on the AKR power. In this way, the average variations in the AKR power with respect to the substorm timeline

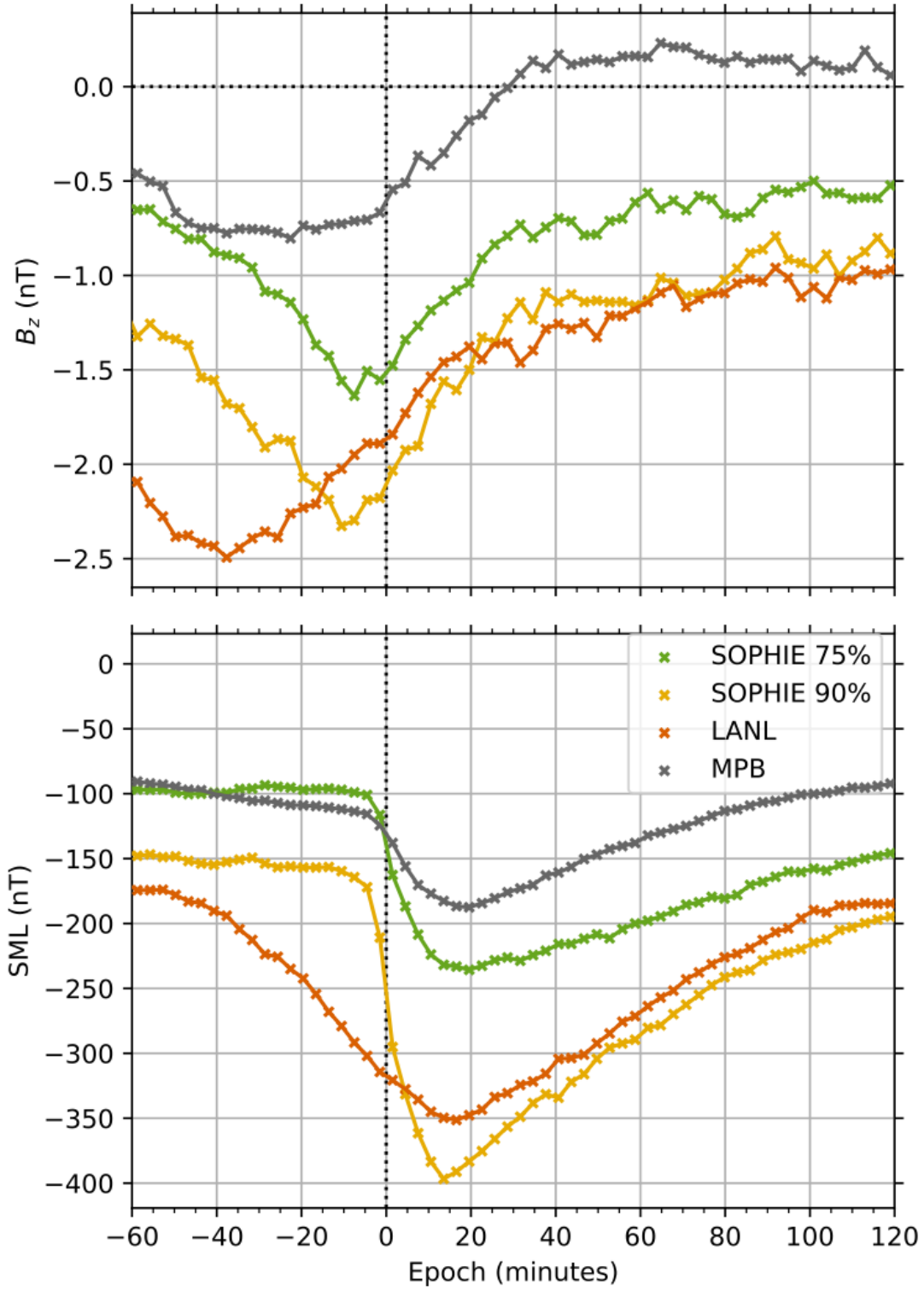

FIGURE 5.3: Superposed epoch analysis of a) solar wind data from OMNIWeb (Papitashvili and King, 2020), showing the median B_Z (z component of the interplanetary magnetic field (IMF) in GSM coordinates) and b) median SuperMAG (Gjerloev, 2012) SML for a 3 hour window about the time identified as substorm onset by various event lists. The legend denotes the median values derived from the respective event lists. The first two refer to the list derived by Forsyth et al. (2015) which relies on the SuperMAG network of ground magnetometers. Accompanying percentages represent the expansion percentile threshold (EPT) value used in their algorithm. For the two SOPHIE event lists, only the substorm expansion phase onsets are used instead of substorm intensifications (initial instead of multiple successive onsets). The LANL list is that derived by Borovsky and Yakymenko (2017) and uses observations of energetic electron particle injections from the LANL satellites at geosynchronous orbit. The MPB list is that derived by McPherron and Chu (2018) and uses the mid-latitude positive bay (MPB) index, also derived by ground magnetometers.

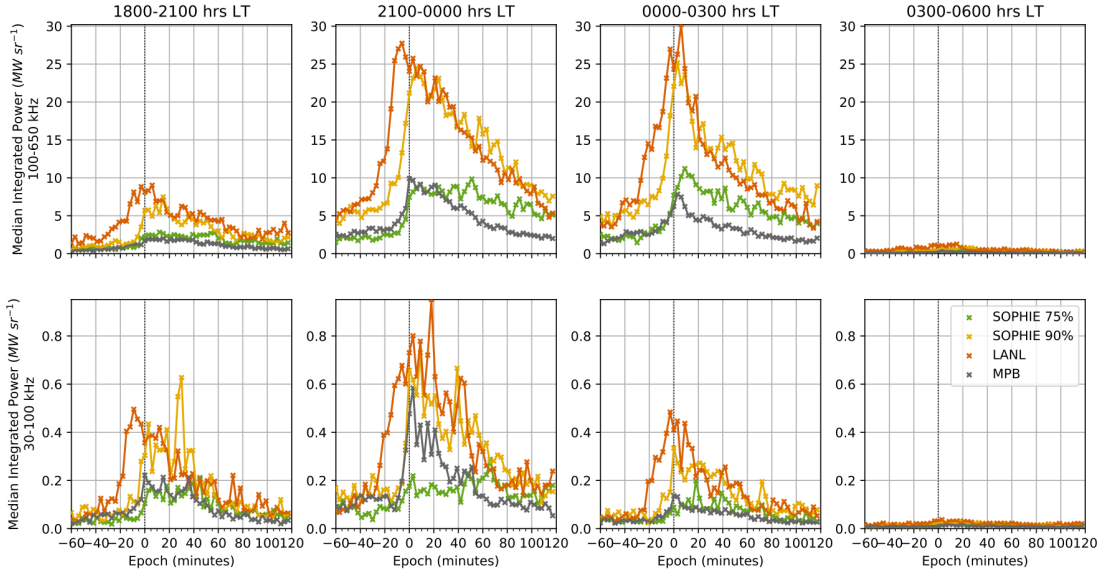

FIGURE 5.4: Superposed epoch analyses of the median AKR power about substorm expansion phase onset. The AKR power is given in units of $MWsr^{-1}$ and binned at 3 minute resolution, and is shown for a 3 hour window, offset from the onset by 30 minutes. The AKR power is integrated in two frequency ranges, 100-650 kHz and 30-100 kHz, characterising what is referred to here as HF and LF AKR. The top row of the figure shows the HF AKR response, while the bottom row shows the LF AKR response. Each column shows the AKR response for epochs based on the observation LT (of Wind), representing 3-hour-wide LT sectors covering the nightside from 1800-0600. Each line shows the AKR power for a different event list of onsets, denoted in the legend and corresponding to the same event lists as in figure 5.3.

can be deduced, removing any variations that could be present for single events and not representative of the typical AKR response. For each of the onset lists described in section 5.2, I select the substorm onsets in the appropriate period (1995-2004). As mentioned in section 5.2, the SOPHIE lists are then reduced to include only expansion phase onsets that follow growth phases (i.e removing onsets that represent substorm intensifications), as defined by the SOPHIE algorithm. After selecting events to correspond with the observation period of Wind, I further subset the event lists to include only those events which occur when Wind is found in particular LT ranges. The nightside is split into 3-hour-wide LT sectors from 1800 to 0600, and superposed epoch analyses are conducted for observations from these sectors. For each of the substorm onset times in their respective lists the AKR power across the epoch window is binned in 3-minute wide bins before the median is taken over all of the events. Data where no AKR observations are recorded are excluded from the analysis. Here, the epoch window is taken to be 3 hours (-60 to +120 minutes about onset). Given that the outputs of both the initial AKR selection and the refined AKR burst selection may contain empty observations, each set of 3 minute bins may not be filled for all events from a particular list. Thus, for a given number of substorm onsets, a variable fraction of these contribute to the overall average.

Table 5.1 shows the number of resulting onsets for each LT sector that are used in the

following analysis. The table again reflects the sensitivity of the substorm onset event lists, with the MPB list giving the most events while the LANL and SOPHIE 90% lists, which record stronger substorms, contain the least. It is important to note that the LT selection refers to the observer (Wind) and not the AKR sources themselves. The beaming of AKR and the nature of the remote Wind observations are such that the emission from an AKR source may be observed by Wind when it is at a position up to ∼2 hours away in LT, based on previous observations of AKR and equivalent emission at Saturn (Lamy et al., 2008a; Kimura et al., 2013; Schreiber et al., 2017). However, given that the AKR response here is averaged over a significant number of events, and following comparison with results of a superposed epoch analysis using events from a wide LT range centred on midnight (2000-0400 hours), it is likely that the response is attributable to the most intense AKR sources at least close to the corresponding 3 hour wide sectors mentioned above.

Figure 5.4 shows the results of superposed epoch analyses for each event list and LT sector. Each column of the figure shows results from a different LT range, displayed at the top of the plot. The top row of the figure pertains to the HF AKR response, showing the median AKR power integrated over the frequency range 100-650 kHz, while the bottom row presents the median AKR power integrated between 30-100 kHz and thus the LF, higher altitude AKR response. The median AKR power in both the HF and LF frequency ranges show an increase close to onset, although the largest increases are seen in the LT ranges 1800-2100, 2100-0000 and 0000-0300. The average response observed from 0300-0600 is barely apparent on a comparable scale; the LF peaks for the 0300-0600 LT range reach no more than 10% and 5% of the LF peaks for the 0000-0300 and 2100-0000 LT sectors, respectively, when comparing the results from the SOPHIE 90% event list. The HF peak of the 0300-0600 LT sector reaches no more than 5% of the HF peaks for 2100-0000 and 0000-0300 LT sectors.

The comparative magnitude of events selected by each list is seen in the AKR response, with the median power for the LANL and SOPHIE 90% lists greatly exceeding that for the SOPHIE 75% and MPB lists, which each have a similar response in magnitude. In the HF, each list sees a gradual increase in the AKR power from 20 to 0 minutes before the epoch, with an increasingly steep rise to a clear peak in the 20 minutes after the epoch. For the LF, each list also sees an increase in the AKR power from 20 to 0 minutes before the epoch, but the peak is seen up to an hour after the epoch. The profiles are noisier in the LF, however, which could be due to the inclusion of less AKR observations at low frequencies and subsequent influence of powerful bursts for a given observation. Particularly prominent peaks appear in the LT ranges 1800-2100 for the SOPHIE 90% list, and 2100-0000 for the SOPHIE 90% and LANL lists, at ∼20-40 minutes after onset. This could be indicative of further substorm intensifications occurring.Although changes in the average AKR power profile gained using events from the LANL list tend to precede those from other lists, this is assumed

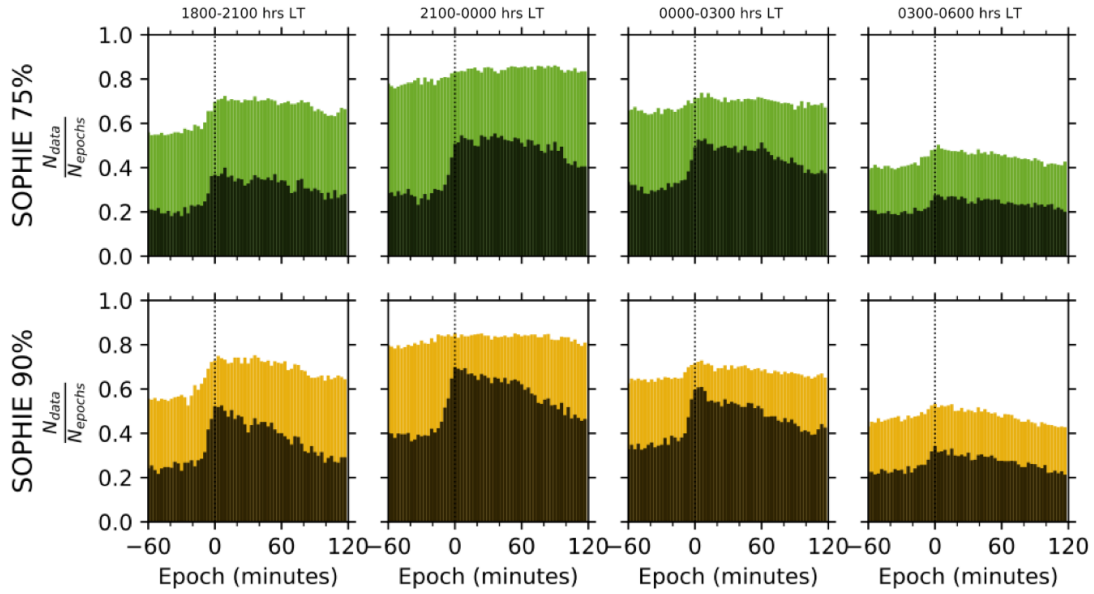

FIGURE 5.5: Occurrence of AKR observations in each 3 minute bin relative to epoch used in the analysis, for both SOPHIE 75% (top row) and SOPHIE 90% (bottom row) event lists. The columns represent LT ranges of analysis in the same way as Figure 5.4. The coloured distribution for each panel represents the HF AKR observations, while the black distribution represents the LF AKR observations.

to be due to the aforementioned coarse resolution of the selection algorithm used. While there is a clear gradual rise in AKR power in the 20 minutes preceding onset, the beginning of the steep increase to the peak is clearly seen between $\sim$ -20 to -5 minutes, which could indicate the ignition of more powerful AKR source regions prior to other observable signatures of substorm onset. The idiosyncracies of the lists may have a greater influence than a true AKR response, however. For SOPHIE lists, the AKR response here could reflect the median SML response in Figure 5.3 which begins to decrease prior to the epoch. The coarse resolution of the LANL event list means the exact time of an onset-associated response in the corresponding AKR observation may be lost. It is also important to note that the minimum resolution for all frequency channels from the Waters et al (2021) dataset is 3 minutes, thus the analysis of the AKR coupling timeline during substorm onset is limited by this resolution. While it is clear from Figure 5.4, then, that the AKR response begins to increase before the identified substorm onset, more work is needed to properly determine the prevalence of an AKR signature as a precursor to substorm onset.

Figure 5.5 shows the number of AKR power data included in each 3 minute epoch bin, compiled over all events and as a fraction of the total number of onsets in each LT range (as shown in Table 5.1), for both HF and LF AKR power. Each column of Figure 5.5 corresponds to a LT range in the same way as Figure 5.4. The top row of Figure 5.5 shows the distributions for the SOPHIE 75% list, while the bottom row shows those for the SOPHIE 90% list. Each panel shows the HF power counts in colour and the LF power counts in black. Each event list shows a greater increase in the occurrence of LF

	1800-2100	2100-0000	0000-0300	0300-0600
HF	2.2 ± 0.2	2.7 ± 0.1	2.2 ± 0.1	1.7 ± 0.3
LF	2.5 ± 0.2	3.6 ± 0.2	2.9 ± 0.2	1.5 ± 0.2

TABLE 5.2: Ratios, shown for HF and LF frequency ranges and for the nightside LT sectors, of the median power extremes for events from SOPHIE 90% and SOPHIE 75%, and associated uncertainties. See text for a detailed description of the data aggregation.

AKR power at onset than for HF AKR power, in all LT ranges except for 0300-0600 where the increase is similar. This difference is most notable for both lists in the 2100-0000 range, where HF AKR is persistent throughout the epoch while LF AKR is recorded ~ 2 times as often at the epoch than LF AKR at prior times. This is less clear in LT ranges 1800-2100 and 0000-0300, and could be due to the expansion of the auroral oval to wider longitudes from the typical premidnight brightening location (Milan et al., 2009), thus igniting both low and high altitude AKR sources at wider LT. As well as the greater increase in occurrence of LF than HF AKR power at the epoch, the occurrence is consistently higher for the SOPHIE 90% list, indicating that substorms with larger deviations in SML have a greater likelihood of igniting higher altitude AKR sources, on average.

Comparing the response of the AKR power for the SOPHIE 75% and 90% event lists, as shown in figure 5.4, for both frequency ranges across the epoch, it can be seen that the power decreases more gradually after the peak at onset for the SOPHIE 75% (weaker substorms) compared to the SOPHIE 90% (stronger substorms) lists. For the average LF AKR power from the SOPHIE 75% list, considering the 2100-0000 LT range, this continues to increase past the epoch. This could be due to the fact that intensifications (expansion phase onsets following recovery phases) are removed from the analyses, but I have not discriminated substorms that are followed by an intensification. In these cases, the intensification that follows later in the epoch will have associated auroral dynamics, and so also AKR dynamics. Considering the SOPHIE 75% and 90% event lists are derived from a quantile threshold of the rate of change of SML (the EPT value), it follows that the former list will include more events in total than the latter as events with smaller magnetic fluctuations are retained in the event selection. If those events are also the initial expansion phase onset before multiple intensifications, which may be more likely for a smaller EPT value, then their combined, average effect could produce this.

Table 5.2 shows the result of aggregating statistics of the HF and LF AKR power for each individual event. For each subset of events by LT range, for the SOPHIE 75% and SOPHIE 90% lists, I take the 90th percentile of the AKR power for each event. These values, which represent the extremes of the AKR power reached during the epoch window, are then averaged using the median, with associated uncertainties given by the relative median absolute deviation (MAD). For each LT and power range, the

ratios of the corresponding SOPHIE 90% with the SOPHIE 75% values are taken. In this way, the relative increase in AKR power for stronger substorms in the 3 hour epoch window used here can be characterised for both LF and HF frequency ranges. For all LT and frequency ranges, the average extreme power for events increases for the SOPHIE 90% list over the SOPHIE 75%; this is expected as the differing sensitivities of the event lists (as seen in Figure 5.3) and the results of Figure 5.4 indicate a greater AKR power for larger substorms. Within the uncertainties given in Table 5.2, derived from appropriate error propagation of the corresponding MAD value, the ratio of average extreme power values for HF AKR is lower than LF AKR for all LT ranges except 0300-0600. It is unsurprising that this LT range differs from the others, given the weakest response in AKR power was seen here. The discrepancy is most notable for the premidnight LT sector at 2100-0000, with the average extreme AKR power in the LF 3.6 ± 0.2 times greater for SOPHIE 90% (stronger) onsets than SOPHIE 75% (weaker) onsets, compared to 2.7 ± 0.1 times greater in the HF range. This corroborates previous studies of the statistical magnetic local time (MLT) of substorm onset as well as AKR source locations (Milan et al., 2009; Schreiber et al., 2017). The results of Table 5.2 indicate that the ignition of higher altitude AKR sources is much stronger for larger substorms, and that in turn the activation of the extended auroral acceleration region is higher for these events. It is possible to say that the AKR sources are present at higher altitudes due to the observed emission and increased power. However, the increased intensity of the emission at a certain frequency (and so at a given altitude) could be attributed to a change in the growth rate of the cyclotron maser instability, or the azimuthal extent of the auroral cavity, or both. For this reason, it is difficult to make a direct inference on this without in-situ measurements of the acceleration region, especially with a statistical perspective over many events as shown here.

5.4 Low Frequency AKR Characteristics

The determination of AKR bursts allows me to quantify spectral features such as the bounding frequencies of the bursts and their spectral extent (Fogg et al., 2021). Such parameters can give further insight into the altitudinal evolution of the auroral acceleration region during the substorm timeline. Namely, the bounding frequencies of the observed bursts allow me to estimate the spatial extremes of the auroral acceleration region in which AKR is generated.

Figure 5.6 shows the evolution of burst parameters that result from a superposed epoch analysis that uses the SOPHIE 90% event list, further subset as previously mentioned. The superposed epoch analysis is similarly conducted over a 3 hour window, with AKR observations binned at 3 minute resolution. The top panel of figure 5.6 shows the median spectral extent of AKR bursts, or the difference between

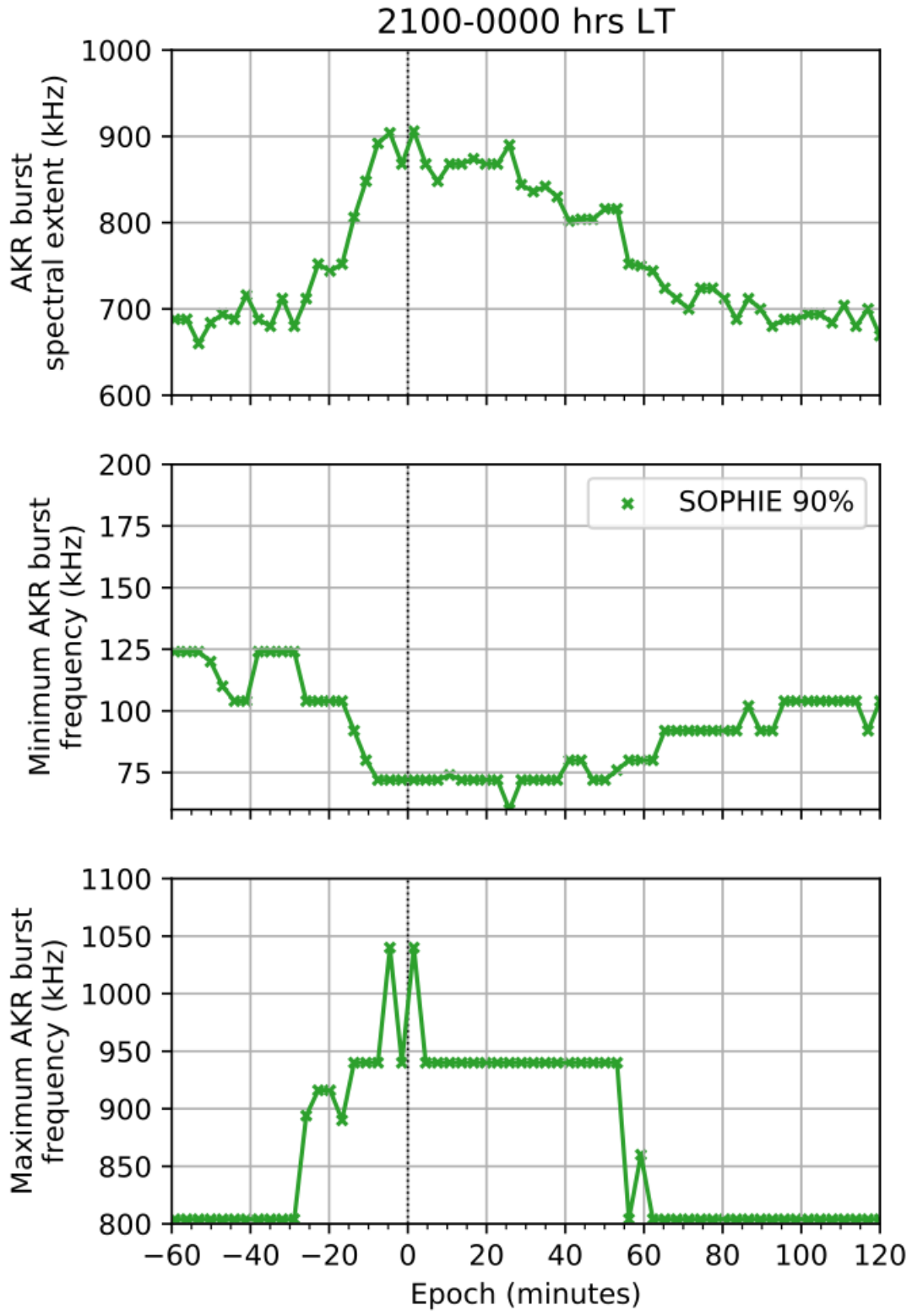

FIGURE 5.6: Superposed epoch analyses of AKR burst parameters observed from the 2100-0000 hrs LT sector. Median burst parameters are shown across the epoch using events from the SOPHIE 90% list for the period 1995-2004. The top panel shows the median spectral extent of AKR bursts, while the middle and bottom panels show the median minimum and maximum bounding frequencies of AKR bursts.

the maximum and minimum frequency channels in which an AKR burst is observed. This provides information on the vertical extent of the acceleration region, given that the cyclotron-maser-instability that generates AKR produces emission at frequencies inversely proportional to the source altitude. For more context to this, and to allow me to quantify the exact altitude of the extremes of the acceleration region, the middle and bottom panel show the median minimum and maximum bounding frequencies of AKR bursts throughout epoch. This allows me to explore how the radio sources grow/move in response to substorm-associated excitation: for example we can see whether the low-frequency component ignition occurs before, simultaneous, or after substorm onset (as defined by complementary datasets in the SOPHIE list). This timing is critical for quantifying the magnetosphere-ionosphere coupling timescale.

The median spectral extent of AKR burst begins to increase from approximately 700 kHz around 20 minutes before onset, approximately coinciding with the increase of AKR power in both frequency bands. The spectral extent peaks at $\sim$ 900 kHz just after onset for this LT sector. This maximum extent is transient, remaining for 3 minutes before gradually decreasing to 700 kHz again 80 minutes after substorm onset. While there is a secondary increase of the spectral extent between 40-60 minutes after onset, this is likely due to the much larger spacing between higher frequency channels and the change in median maximum bounding frequency for this time, as seen in the bottom panel.

The middle panel of figure 5.6 shows the clear decrease in the minimum frequency of AKR bursts during substorm onset. Around 20 minutes before onset, the minimum frequency is measured at approximately 100 kHz. This falls to 75 kHz at onset, which is generally consistent following onset. As found previously, but here shown over a statistical basis with many events, this corresponds to an extension of the AKR to low frequencies at substorm onset. However, these results show a persistent minimum frequency which indicates a more sustained increase in altitude of the acceleration region.

Spectral AKR burst parameters are derived from the discrete frequency channels of Wind observations. This limits the accuracy of the estimation of the height of the source region, particularly at lower altitudes (higher frequencies, here greater than $\sim$ 200 kHz) where observation channels are logarithmically spaced. At higher altitudes however, corresponding to lower frequency channels between 60-148 kHz, the spacing between channels is between 8-20 kHz, with an average spacing of approximately 12 kHz between the 8 frequency channels in this range. This corresponds to an altitude range of $\sim$ 1000 km, assuming the source location is given by the electron gyrofrequency equivalent to the emission frequency and lies on a magnetic field line with an invariant latitude of 70° (as included in and estimated from Figure 3 of (Morioka et al., 2007)). I note that the invariant latitude used to calculate the emission altitudes is higher than the $\sim$65° typical of substorm onset.

The bottom panel of figure 5.6 shows the median maximum bounding frequency of AKR bursts during the substorm timeline. The maximum frequency is mostly consistent in the 30 minutes before onset, at 800 kHz. As well as for the lowest frequencies however, the highest frequencies of emission also change around 20 minutes before onset, increasing to measurements at 1040 kHz 10 minutes before onset. The maximum frequency reaches a peak after onset at the maximum frequency channel of the Wind observations used here, at 1040 kHz. Although there are limitations based on the measuring capabilites of the Wind/Waves RAD1 instrument, as previously mentioned, it is clear that emission that is fairly characterised as AKR is present here.

These results show conclusively that the response of the range of emission frequencies of AKR begins to extend around 20 minutes prior to substorm expansion phase onset as determined by SOPHIE. As well as the results from section 5.3, it is clear that the AKR response precedes substorm onset. This highlights the potential usefulness of the average AKR response as an indicator of substorm onset, particularly given that the low-frequency extensions is apparently exclusive to substorm dynamics. However, more study of the conditions presiding over AKR emission and the occurrence of AKR source dynamics is needed to constrain this understanding.

5.5 Summary

AKR sees enhancements in intensity and changes in frequency, and has been postulated to be associated with other dynamics in the terrestrial magnetosphere such as auroral brightenings and discrete arcs, earthward bulk flows of electrons and strengthenings of high latitude current systems. Previous studies have explored the AKR variability alongside these phenomena, which are also closely associated with substorm dyanmics, but have used AKR observations that cover a few months or studies that include only a few tens to a hundred events. Here I use observations of AKR from Wind, made between 1995-2004, that coincide with published lists of substorm events to expand upon previous studies and further examine the average AKR response during the substorm timeline. I integrate the AKR power over two important frequency ranges that best characterise the spectrum, covering higher and lower frequency portions. To infer the evolution of the acceleration region, I also examine the observed spectral extent of the AKR bursts as well as the minimum and maximum bounding frequency. I use a variety of substorm lists, including those output from the SOPHIE algorithm at EPT values of both 75% and 90%, that derived from the MPB index, and the list derived from the geosynchronous LANL satellites and their measurements of electron populations. The SOPHIE and MPB index lists are themselves derived from ground magnetometer observations. As an initial comparison of the substorm lists themselves, I perform a superposed epoch analysis

of the B_Z component of the interplanetary magnetic field, shown in figure 5.3. This demonstrates the sensitivity of each substorm list; those with a larger southward component prior to onset indicate a list containing the largest events. To ensure observations with approprite viewing of the nightside AKR sources are retained in the analysis of the AKR features, substorm events are subset by the LT of Wind at the time of onset. Once subset in this way, both the AKR power and spectral features of AKR bursts are examined in superposed epoch analyses for each of the substorm lists.

Figure 5.4 shows the results of the superposed epoch analysis of the AKR power for each substorm list, with events subset into four LT sectors, each 3 hours wide, covering the entire nightside from dusk to dawn. Seperate analyses are conducted for the frequency range that characterises the lower frequency AKR component (30-100 kHz) as well as for the higher frequency component (100-650 kHz). These results show that the primary AKR response is centred pre-midnight, and is mostly confined to the sectors neighbouring midnight (LT sectors 2100-0000 hrs and 0000-0300 hrs). The sensitivity of the substorm lists to event size is also seen in the response of the AKR power, with a larger magnitude response for the LANL and SOPHIE 90% lists. Figure 5.4 also shows a response in the AKR power, for all lists, and in both frequency ranges, prior to the onset epoch time. While this suggests that AKR enhancements precedes the other typical signatures of substorm onset shown here, more work is needed to assess the influence of the uncertainty of the event lists. The distribution of AKR power data throughout the epoch for both HF and LF frequency ranges, and both SOPHIE 75% and 90% event lists, is shown in Figure 5.5. This shows a greater increase in occurrence of LF AKR at onset than HF AKR for LT from 2100 to 0300, and that there is a greater likelihood of LF AKR for the stronger events of SOPHIE 90%. The discrepancy between HF and LF occurrence is greatest for pre-midnight observations, corresponding to the typical substorm location. To highlight the differing AKR response between substorms of different strengths, I compare directly the average response from the SOPHIE lists with 75% and 90% EPT values. Table 5.2 shows the increase in averaged, extreme power values during each event, with LF AKR power values 3.6 ± 0.2 times greater for stronger events from the SOPHIE 90% event list than those of the SOPHIE 75%, while HF AKR has values 2.7 ± 0.1 times greater.

The results of comparing the AKR burst parameters with the SOPHIE 90% event list show the average evolution of the nightside AKR source region, viewed remotely, as it extends vertically. Figure 5.6 shows that the response of the AKR power during substorm onset is attributable to this vertical extension of the AKR sources, and the auroral acceleration region by proxy. Our work, based on a decade of high fidelity radio data from Wind/WAVES has shown the utility of the AKR as a proxy for magnetospheric dynamics. In particular, I track the increase in radio power and the expansion in frequency of the spectral signature associated with substorm onset for 10 years of observations where Wind is suitably located. The timing of the AKR response

has been compared between the event lists and show a similar time profile to averages of corresponding indices such as SML, while the greater increase in AKR power for stronger events is likely due to a greater occurrence of LF AKR. While important to acknowledge the temporal uncertainties present in the event lists, further study of the time and magnitude of AKR intensification across events of various sizes can show insightful disparities in the auroral acceleration region via AKR. The utility here suggests that AKR integrated power can be employed more widely by the magnetospheric/ionospheric community as another geomagnetic index to track the global impact of variable space weather.

Chapter 6

AKR Observations Amid Response to ICME

6.1 Introduction

A partially Earth-directed CME was observed at 15:35 UT on 2021 October 28th, following an X1.0 class solar flare emitted from the AR12887 region and the ejection of relativistic protons and electrons from the solar atmosphere. The solar protons ($\sim$450 MeV) produced rare ground level enhancements (GLEs) at Earth, one of five since 1976 that occurred with a flare of this magnitude (Papaioannou et al., 2022). Accelerated electrons radiated non-thermal radio emission in a host of particularly intense solar radio bursts. The CME was observed by the Large Angle Spectrometric Coronagraph (LASCO; (Brueckner et al., 1995)) C2 as a partial halo propagating towards the south. From the broader literature (e.g. Taylor et al., 1994; Hutchinson et al., 2011; Kilpua et al., 2017), a strong geomagnetic response is expected when the upstream medium is characterized by high solar wind flow speed, high solar wind dynamic pressure and southward-directed interplanetary magnetic field (IMF).

This solar activity provided an opportune event, in the new rising phase of the solar cycle, to study its effect on Earth's magnetosphere in the space weather context. While *in-situ* observations can provide insight into the solar wind plasma itself, the suite of terrestrial instruments (both remote and ground-based) can also be used to track the coupling of the magnetosphere to the CME-associated solar wind, or interplanetary CME (ICME). With upstream monitors like Wind at the Lagrange point L1, the interplanetary magnetic field (IMF) and plasma parameters can be measured continuously. These parameters have been used to define non-linear coupling relationships (e.g. Milan et al., 2012) that characterize magnetic reconnection processes between the IMF and the planetary magnetic field on the dayside of the terrestrial magnetosphere, allowing inference of open flux being transported across the polar cap

and into the nightside magnetosphere. Widely distributed magnetometer stations are used to measure the magnetic disturbance, signalling strengthened current systems and the onset of storms and substorms (Iyemori, 1990; Newell and Gjerloev, 2011). Electron precipitation along magnetic field aligned currents (FACs) produces the UV and optical aurora in the ionosphere, but also source regions of Auroral Kilometric Radiation (AKR) above it under certain conditions (e.g. Wu and Lee, 1979; Treumann, 2006). These auroral emissions, monitored remotely, provide a comprehensive picture of the dynamics of the auroral acceleration region when accounting for complex viewing effects of AKR (Gurnett, 1974; Alexander and Kaiser, 1976; Mutel et al., 2008; Zhao et al., 2019).

In this work, I examine the response of the near-Earth environment in terms of solar wind conditions and various geomagnetic indices, giving both an in-situ and remotely sensed picture of magnetospheric conditions in the days during and following the arrival of the ICME. Furthermore, I present subsequent, novel observations of AKR made by Wind/Waves from L1, 250 R_E from Earth. Section 6.2 presents the observations made throughout the coupling timeline following the CME: section 6.2.1 describes the upstream solar wind conditions following the arrival of the ICME at Earth. Section 6.2.2 describes the timeline of the geomagnetic response at various scales using OMNI data, SuperMAG geomagnetic indices (Gjerloev, 2012) and PC indices (Troshichev and Andrezen, 1985; Stauning, 2013), supplemented by Wind/WAVES AKR observations. Section 6.2.3 presents UV auroral observations with the observed AKR to interpret the driving origin of the radio emission. Section 6.3 summarises the case study of the event.

6.2 Observations

6.2.1 Solar Wind Conditions at the Bow Shock

Figure 6.1 shows a combination of remote sensing and *in-situ* data which illustrate the impact of the ICME at Earth. Radio observations made by the Wind/WAVES/RAD1 instrument are seen in the top panel, exhibiting clear signatures of solar type III radio bursts, characterised by bright sweeping arcs that are much more intense than the radio background. Type IIIs are generated by fast (∼0.3c) electron beams; they indicate solar activity, particularly travelling shockfronts, associated with the CME. An example of an intense Type III burst is seen at ∼15:30 UT in panel a of Figure 6.1. Panels b and c illustrate the IMF and solar wind conditions as the ICME sweeps over OMNI spacecraft, parked at the Lagrange 1 point 250 R_E upstream of Earth.

The Z and Y components of the interplanetary magnetic field (IMF) propagated to the terrestrial bow shock are presented in the panel b of Figure 6.1. At the beginning of the

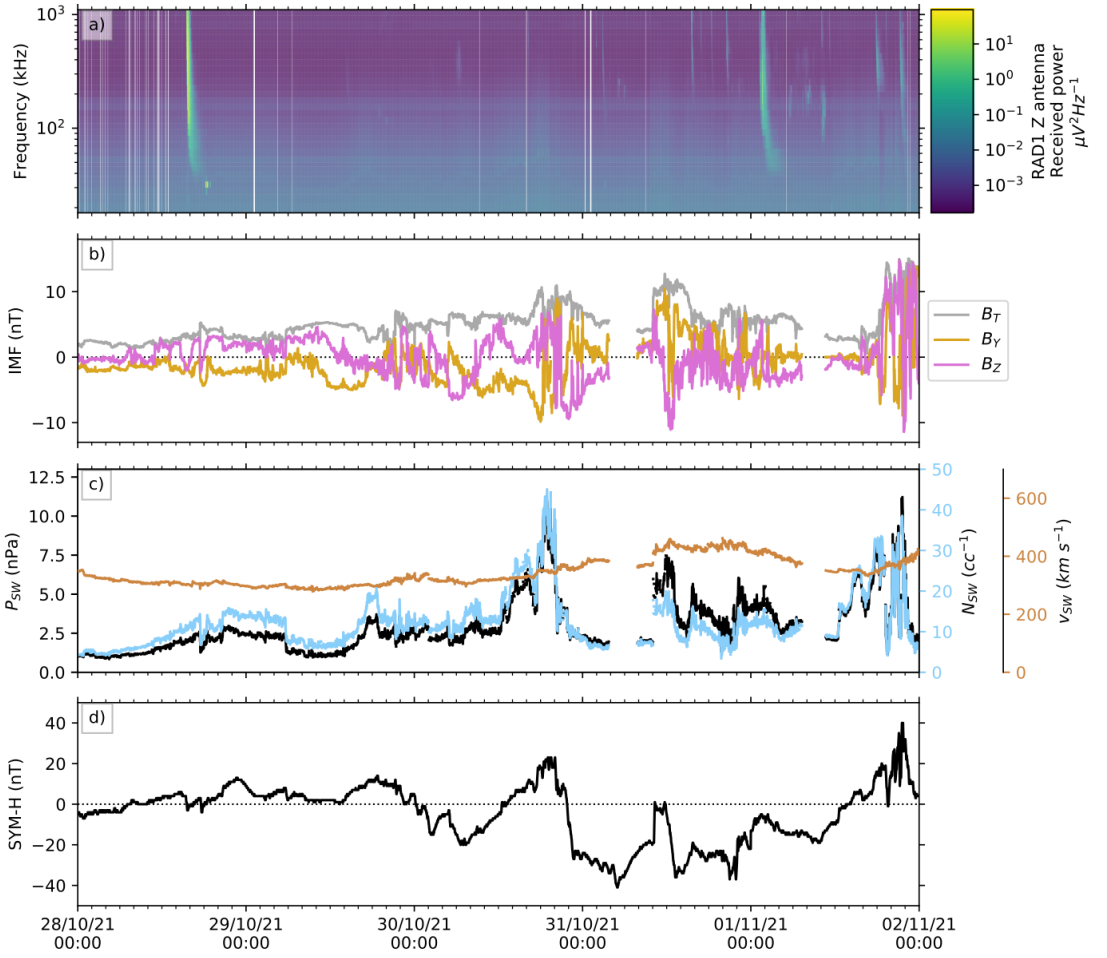

FIGURE 6.1: Observations between the 28th October and 2nd November 2021 of: a) radio emission showing intense Type III bursts near the time of the CME; b) total (B_T) and transverse (B_Y, B_Z) IMF magnitudes; c) solar wind flow pressure (P_{SW}), proton density (N_{SW}) and flow speed (V_{SW}); d) SYM-H, showing the terrestrial ring current response.

presented interval, the magnitude of both components is close to zero, often with weakly positive B_Z and weakly negative B_Y. While the total magnetic field begins to slowly increase from the start of the interval, significant fluctuations in the B_Z and B_Y IMF components and a total increase are seen from ~21:00 UT on 29th October 2021, after which large excursions in the Z and Y components continue as does the increase in the total magnetic field density. This results in a rotation in the clock angle, which is particularly dramatic at around 20:00 UT 30th October 2021, and continues afterwards. This is similar to signatures associated with the passing of an interplanetary coronal mass ejection (ICME) (e.g. Carter et al., 2020).

The solar wind characteristics during this event are presented in panel c of Figure 6.1, with the dynamic pressure in black, proton density in blue and flow speed in gold. Simultaneous to rotation in the clock angle mentioned previously, a multi-step increase in solar wind dynamic pressure is observed in the later half of 30th October

2021. The peak dynamic pressure of ∼12 nPa occurs at 18:56. This pressure (proportional to $N_{SW}V_{SW}^2$) increase is dominated by the shape of the density curve displayed in blue, and no clear related signatures are observed in the flow speed for 30th October 2021. Combined with the clock angle rotation, this is indicative of the passing of an ICME, such as that observed by Carter et al. (2020). Noting that median P_{SW} values at 1 AU are of the order of several nPa (e.g. Fogg et al., 2022), a pressure enhancement reaching the order of 10 nPa suggests a substantially compressed magnetosphere. This is confirmed (Araki, 1994) by a rapid increase in SYM-H (presented in the panel d of the Figure 6.1), followed by a sharp decrease to negative values, with oscillations around the negative peak at ∼05:00 UT, 31st October 2021. Such a signature, driven by a rapid compression of the magnetosphere, is known as a geomagnetic sudden storm commencement (SSC); shown to be driven by ICMEs by Taylor et al. (1994). A disturbed recovery period is observed in SYM-H. This is an SSC of only moderate magnitude, surpassing the quiet level of -15 nT defined by Walach and Grocott (2019) by about 25 nT at the peak of the storm.

6.2.2 Geomagnetic Activity

Geomagnetic indices are powerful tools which characterise the state of the magnetosphere. In this work, SYM-H, PC(N,S), SMU and SML indices are used; all continuous, minute resolution products derived from ground based magnetometer data, thus not limited by spacecraft position. Each index is amalgamated from individual stations, and shows deflections in the magnetic field as a result of changes in overhead currents. SYM-H (Iyemori, 1990) is derived from magnetometers at equatorial latitudes, indicating changes in the ring current and showing characteristic signatures of geomagnetic storms (e.g. Walach and Grocott, 2019). The polar cap indices PC(N,S) (e.g. Troshichev and Andrezen, 1985; Stauning, 2013) are measured by stations at polar latitudes in the northern and southern (geographic) hemispheres; they record the strength of cross polar currents, with larger values suggesting faster antisunward flux transport. Those used here are based on the original concept for the PC index referred to in Troshichev and Andrezen (1985), although Stauning (2013) indicate issues with the derivation method a detailed discussion is deferred here. Finally, SMU and SML (Gjerloev, 2012) are the upper and lower envelopes of the SuperMAG electrojet index, and show the strength of the eastward and westward electrojets respectively. These are measured from magnetometers in the auroral zone, and are roughly equivalent to the auroral electrojet indices AU and AL (Davis and Sugiura, 1966), which were not available for this interval. Most famously, SML/AL show distinct substorm signatures (e.g. Newell and Gjerloev, 2011; Forsyth et al., 2015). Figure 6.2 shows several parameters which reveal the terrestrial magnetospheric response to the arrival of the ICME.

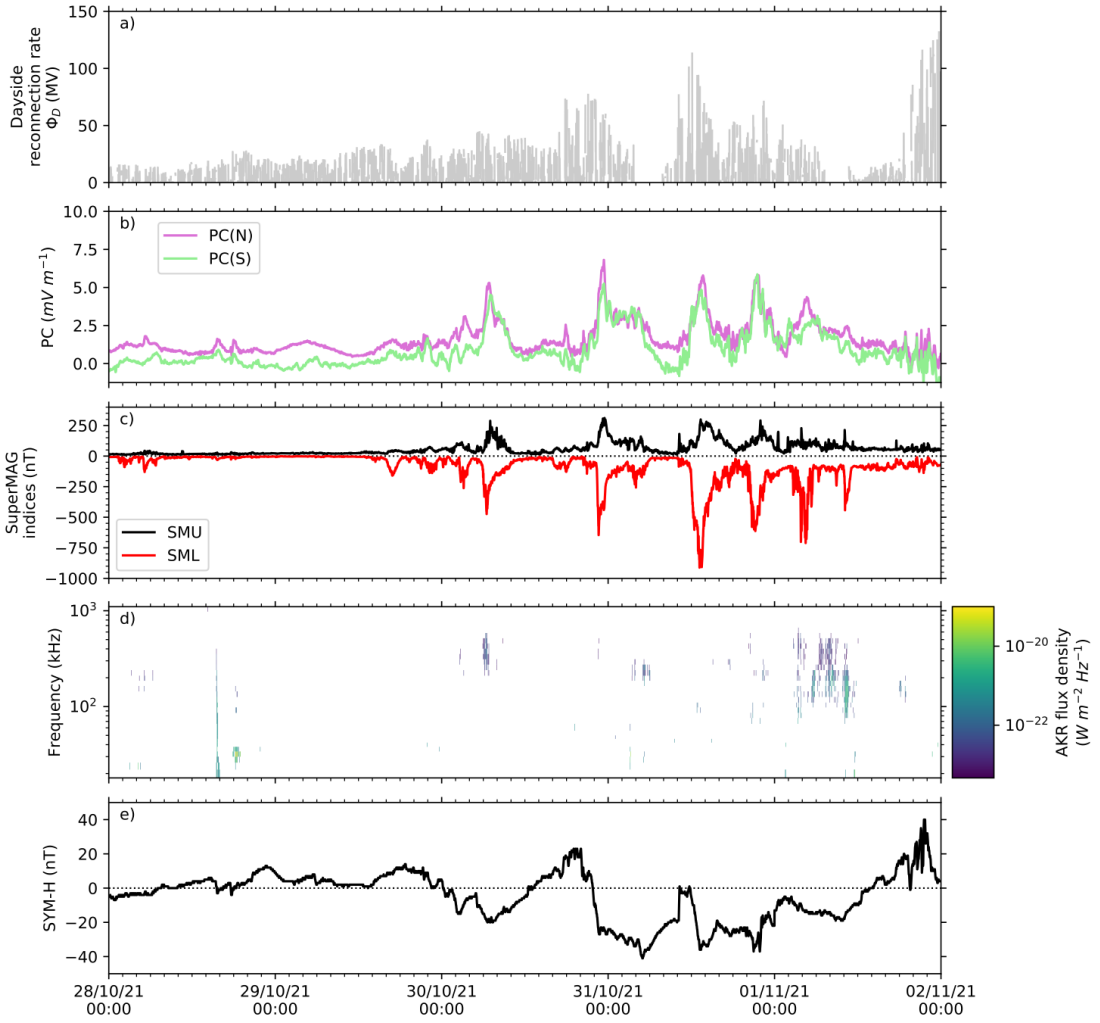

FIGURE 6.2: Magnetospheric response given by a) the dayside reconnection rate, b) PC indices for both hemispheres, c) auroral electrojet (SMU/SML) indices from SuperMAG, d) AKR observations made from L1 and e) the SYM-H index for 28th October to 2nd November 2021.

Figure 6.2a shows the dayside reconnection rate of Milan et al. (2012) a method of representing the energy input from the solar wind at the magnetopause boundary. This is repeated here in equation 6.1, where $L_{eff} = 3.8R_E(4 \times 10^{-5}V_X)^{1/3})$. This represents the non-linear coupling effects that can stimulate a cycle of magnetospheric dynamics and precede other phenomena within the inner magnetosphere. The reconnection voltage increases with the variations in the transverse (Y and Z) components of the IMF, and gradual increase in solar wind speed, towards the end of 30th October 2021. While the largest reconnection rate seen in figure 6.2a is at the very end of 1st November 2021, the peak prior to this, which we believe to be the last associated with the ICME in question here and is the second largest observed in the figure, occurs with the most extreme Southward IMF at midday on 31st October 2021.

$$\Phi_D = L_{eff}(V_x) V_x B_{YZ} \sin^{9/2} \frac{1}{2}\theta \tag{6.1}$$

Towards the beginning of the presented interval, the polar cap indices PC(N,S) are relatively quiet; PC(N) is around the median values presented by Fogg et al. (2022). Throughout the interval shown in Figure 6.2b, both PC(N) and PC(S) follow similar shapes, suggesting balanced flux transport in both hemispheres. At the start of 30th October 2021, around 07:00 UT, the PC indices exceed 4 mVm^{-1}, in a short lived enhancement, prior to the primary P_{SW} enhancement. The PC(N) index peaks at ∼5.0 mVm^{-1} at 06:46 while PC(S) peaks at ∼4.1 mVm^{-1} at 07:03. A subsequent enhancement is seen roughly within the main phase of the SSC, with corresponding oscillatory activity. Following this, more short-lived enhancements in the PC index are observed within the disturbed recovery period of the storm, including another minor negative deviation that could be indicative of further ring current energisation. The enhancements to the PC index that follow the initial pressure pulse, while shorter, reach similar values in PC(S) and slightly smaller (within ∼ 5-20%) values for PC(N). These enhancements evidence periods of rapid flux transport that facilitate the loading of magnetic energy; a prerequisite for the substorm dynamics of Figure 6.2c.

For all of the major SML diversions in the interval, their peak magnitude is at least two times greater than that of the SMU index, indicating a substorm-like response in the magnetosphere. The SMU and SML indices are both quiet at the beginning of the interval; SML reaching no more than -200 nT before 30th October 2021. A significant diversion in SML of -500 nT is seen at the same time as the first major increase of both PC indices on 30th October 2021; around 39 hours after solar flares associated with the 28th October 2021 CME were recorded. This diversion in the SML coincides with a Southward-turning IMF B_Z component, as seen in both Figure 6.1b and Figure 6.2a. Another significant SML peak is seen at ∼22:30 UT, corresponding to the largest values of the dayside reconnection voltage since the arrival of the large pressure pulse as seen in Figure 6.1. This substorm onset accompanies the geomagnetic storm-like response of the SYM-H index, with the peak SML diversion occurring as SYM-H becomes negative.

The following substorm onset at ∼ 13:00 UT, 31st October 2021, exhibits the largest disturbance to the geomagnetic field, with a negative peak of almost -1000 nT preceded (∼ 30 min) by the peak dayside reconnection rate. The PC indices are lower than for the previous onset although peak in both hemispheres at ∼ 5 mVm^{-1}. This onset also corresponds with a second pressure pulse in the solar wind and a second energisation of the ring current as shown by SYM-H. Another substorm onset occurs at ∼ 21:00 UT, with a SML diversion of -600 nT, PC indices of similar values to the previous onset and during increased solar wind speed.

For 1st November 2021, a substorm onset is observed after the dayside reconnection rate decreases from 50 MV. SML values exhibit the second largest diversion of the interval; peaking close to -750 nT. The corresponding peaks in the PC indices exhibit asymmetry; the PC(S) index falls to nearly half of its original value at ~ 2.5 mVm^{-1}, while the PC(N) index falls to ~ 4 mVm^{-1}. While the SML profile around 04:00 UT contains the largest diversion for the 1st November 2021, smaller fluctuations occur until another questionable, smaller onset is seen at 10:00 UT. These high latitude current fluctuations occur while the ring current is recovering from storm-time conditions on average, although the SYM-H behaviour local to 04:00 UT is again decreasing, suggesting a minor introduction of solar wind particles.

When comparing SML values for time periods identified as substorm onset by various observational signatures, Forsyth et al. (2015) found the largest of the median SML diversion was -200 nT, for the event list of Newell and Gjerloev (2011). Coxon et al. (2014) found that typical substorms have an average SML disturbance of -400 nT. Although "supersubstorms" can produce diversions of -2700 nT (Nishimura et al., 2020), this implies that the substorm onsets seen during this interval are large compared to phenomena typically classified as a substorm.

Figures 6.2d and 6.2e also show observations that serve as a proxy for the geomagnetic response, albeit on different scales. The following section 6.2.3 accounts for the AKR observations of Figure 6.2d and attempts to infer dayside magnetospheric dynamics via conjugate auroral observations. The aforementioned SYM-H in Figure 6.2e is described in section 6.2.1.

6.2.3 AKR and Dayside Aurora

Figure 6.2d shows observations of AKR from Wind/WAVES/RAD1 following application of the process described in Waters et al. (2021a). The Wind spacecraft was located at L1 during the entire interval. As AKR source regions are usually found on the nightside and the beaming is highly directed, Wind cannot readily observe AKR from substorm-associated auroral dynamics while it is at L1 (Mutel et al., 2008; Waters et al., 2021a; Fogg et al., 2022). Previous observations have also revealed AKR sources more widely distributed in the dusk and even dayside sectors (Mutel et al., 2008), as well as other mechanisms for dayside sources such as cusp aurora and transpolar arcs (e.g. Alexander and Kaiser, 1977; Pedersen et al., 1992; Hanasz et al., 2000; Mutel et al., 2004). Although some emission retained by the selection here is sparse at typical AKR frequencies (100-700 kHz (Morioka et al., 2007, 2013)), sometimes observed to occur for the time of a single frequency sweep (3 minutes), there are also periods of longer, continuous bursts. The selected emission at $\sim$15:30 UT on 28th October 2021 is associated with the Type III burst; the narrow, tall structure in the spectrogram is likely due to RFI following saturation at the reciever when the initial, most intense

part of the Type III is observed, while the burst that follows around the same time is likely due to electrons from the shock reaching the spacecraft and creating shot noise.

Sustained AKR bursts are seen after 30th October 2021, the most prominent just before 06:00 UT, lasting 2 hours between 250-500 kHz and for a 9 hour period from ∼03:00 UT on 1st November 2021. The latter, most significant observations of AKR are seen on 1st November 2021; emission is observed from 03:00 to 11:00 UT between ∼80-500 kHz and is the most intense in this interval. Bursts of emission between 80-150 kHz are more intense than other AKR observed on this date, and exhibit apparent periodicity of ∼2 hours. Fainter AKR is observed at higher frequencies (150-500 kHz).

Each observed AKR burst coincides with an SML diversion $<$ -250 nT. However, some of the intervals of largest SML diversion see no AKR observations. Notably, substorm onsets at 22:15 UT on 30th October and 13:00 UT on 31st October are not accompanied by significant AKR observations. While short, sporadic AKR observations are made on the 31st October, they are minor considering this is the largest substorm onset observed for the period. Observations on the 1st November are similar, with the more sustained (30-60 min), apparently periodic bursts of AKR following substorm onset.

While sources of AKR production on the dayside magnetosphere do exist, it is difficult to discern these from AKR observations and accompanying geomagnetic indices directly, due to the differing scale of the associated plasma dynamics. While it cannot be assumed that L1 observations represent the entirety of the global AKR spectrum, it is also true that the lack of AKR does not immediately imply its absence due to the aforementioned viewing constraints. As well as dayside sources of AKR, illumination of Wind/WAVES by AKR sources could be due to the emission cone of duskside source regions under changing magnetospheric conditions such as the latitudinal extent of the aurora. To aid the interpretation of the AKR observations and disentangle the viewing and magnetospheric driving effects, I employ UV auroral observations from the DMSP/SSUSI instrument (Paxton et al., 1992; Carter et al., 2018).

The SSUSI instrument consists of a scanning spectrometer that observes the aurora in select wavelengths, capturing electron precipitation through their interaction with the ionosphere. As a DMSP spacecraft passes over the pole, taking ∼20 minutes, observations of segments perpendicular to the footpath of the satellite are made. For this analysis, SSUSI observations of auroral radiance and the corresponding position in the oval are binned over 15 seconds and averaged to give values representing a relatively small local area. I use data from the DMSP F18 spacecraft and the LBHS channel (N2 emission, 140-150 nm). To discern the AKR origin from UV aurora, SSUSI observations of the dayside oval from each polar pass are subset into 4 hour wide magnetic local time (MLT) sectors. Given the slight variation in spacecraft trajectory for each orbit and subsequent spatial sampling, each MLT sector for each orbit has a differing number of data included, also varying between orbits. The sampling of

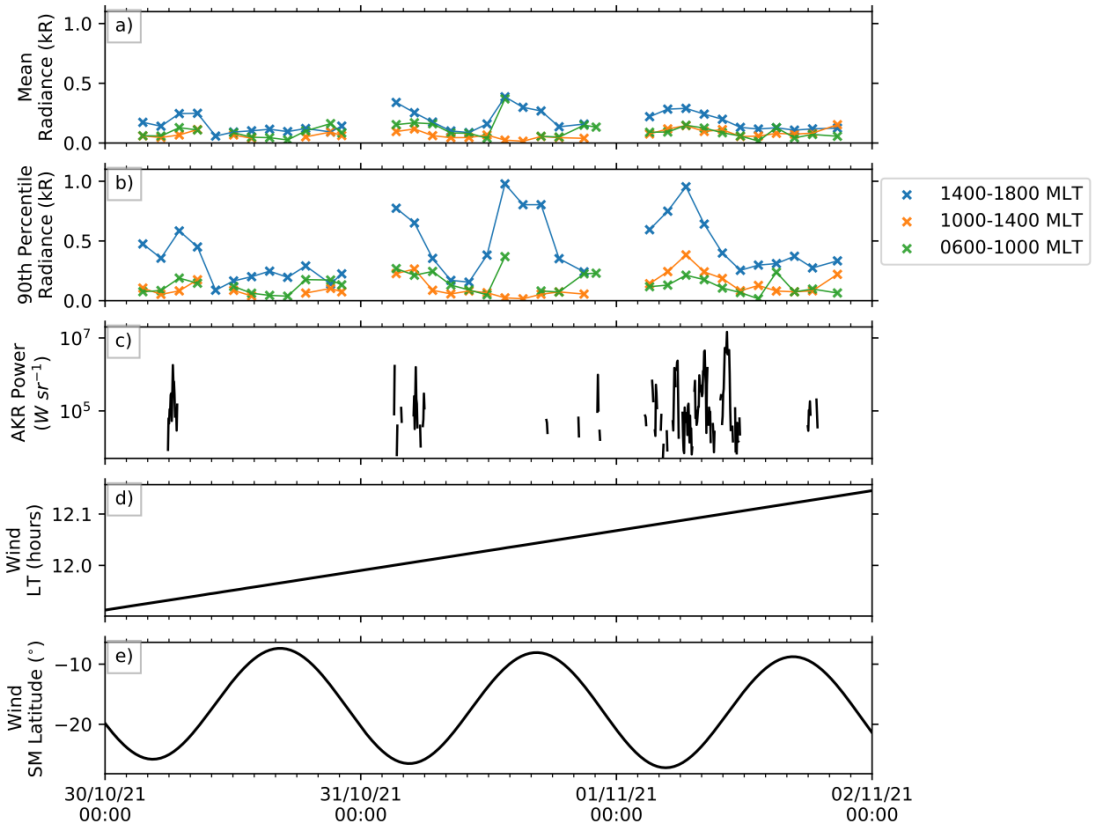

FIGURE 6.3: a) Mean and b) 90th percentile of electron auroral radiances for 4 hour wide MLT sectors on the dayside, with each marker representing selected DMSP/SSUSI observations. c) Fractional emitted AKR power from Wind/WAVES, integrated between 30-650 kHz. d) LT and e) latitude of Wind in the solar magnetic coordinate system.

SSUSI dictates that comparisons between the AKR and auroral emission cannot be quantified certainly on timescales less than approximately 40 minutes, so data in each sector are averaged. The time representing these averages is the median observation time of the orbital pass.

Figure 6.3 shows the SSUSI observations of UV auroral radiance in kR, reduced over each orbit of the DMSP F18 spacecraft for this period and subset in MLT sectors 06:00-10:00, 10:00-14:00 and 14:00-18:00 hours. Panels a and b show the mean averaged and 90th percentile values of the auroral radiances for each MLT sector. Also shown is the AKR power (c), integrated between 30-650 kHz, and the LT (d) and latitude (e) of the Wind spacecraft in the geocentric solar ecliptic and solar magnetic (SM) coordinate systems, respectively. The latter show the slowly varying LT of Wind as it orbits L1, and the SM latitude varies as the magnetic dipole tilts with the diurnal rotation.

The afternoon sector (14:00-18:00 MLT) exhibits the brightest mean auroral radiance (Figure 6.3a) of the dayside for these observations, reaching the maximum of 0.39 kR at around 13:00 UT on 31st October 2021, the same time as the largest substorm onset here. Although peaks in auroral radiance with similar magnitude occur in the

afternoon sector at other times in this 3 day period, the orbital pass centred closest to 13:00 UT also observes aurora in the morning sector that is uncommonly bright for these observations at 0.37 kR. Figure 6.3b shows the 90th percentile from each MLT sector, representing extreme occurrences and likely the presence of bright, discrete aurora for values much higher than the mean. This is true for the afternoon sector where peak 90th percentile values are between 2-3 times that of the mean. Extreme values in other MLT sectors exhibit similar values to the mean, suggesting either that their aurora is diffuse or that there are not many data observed in those sectors for those orbital passes.

The AKR observations are shown here in terms of the power in $\mathrm{W\,sr^{-1}}$, and are derived directly from the flux density in Figure 6.2d. Observed AKR bursts for this period exhibit a peak power of $\sim 10^6\,\mathrm{W\,sr^{-1}}$. The most powerful AKR burst, with a peak at ~10:15 UT, reaches $> 10^7\,\mathrm{W\,sr^{-1}}$. The average AKR power observed by Wind between 1995-2004, and from LTs between 11:30-12:30, is between 5×10^4 and $6\times10^4\,\mathrm{W\,sr^{-1}}$ (Waters et al., 2022). The median AKR power observed for this period from 12:00 LT is $6.4\times10^4\,\mathrm{W\,sr^{-1}}$. With the exception of the peak in the auroral radiance at 13:00 UT on 31st October 2021, the bright, discrete auroral emissions in the afternoon sector are accompanied by AKR bursts.

As AKR source regions exist on high latitude magnetic field lines, they will tilt with the magnetic axis as Earth rotates. Figures 6.3c and 6.3e show that, generally, AKR is observed from L1 when Wind is furthest from the magnetic equator. This agrees with previous studies of the effect of the observer latitude on AKR viewing (Lamy et al., 2010; Waters et al., 2021a), and is expected given the beaming from the source region (Mutel et al., 2008). This would also explain the lack of observed AKR during the strongest substorm onset of the period at 13:00 on 31st October 2021, with which the bright auroral radiance is associated.

However, with the remote sensing observations here, it is difficult to discern the true nature of the observations; while SSUSI observations exhibit auroral brightenings, the latitude, longitudinal extent and the auroral intensity below regions of strong upward FAC that would generate AKR could combine to influence the measurements. A statistical study of L1 observations and latitudinal effects is needed to properly discern between viewing effects or a lack of AKR bursting on the dayside. However, it is clear that the observed AKR power is related to bright auroral structures between 14:00-18:00 MLT. Previous mapping of AKR sources to discrete auroral structures (Huff et al., 1988; Menietti et al., 2011b; Yearby and Pickett, 2022) and the presence of strong upward FACs required for their existence suggest this is the auroral source of the AKR. These structures are likely to be associated with the ionospheric current system that travels Westward at substorm onset, given the SML profile for this period. These AKR observations are thus the first to be made from L1 in a case study context, and are the first to show dayside AKR sources likely associated with substorm onset.

6.3 Summary

An ICME that erupted from the Sun on 28th October 2021 was accompanied by an X1.0 class solar flare and intense radio emissions, with SEPs producing GLEs measured at Earth. The associated magnetic structures rapidly induced an SSC geomagnetic storm when they reached Earth $\sim$ 2 days later, revealed in the OMNI solar wind observations and the SYM-H geomagnetic index. Using derived measures of both solar wind parameters and ground magnetometer data, namely with the Milan et al. (2012) dayside reconnection rate and the PC and SuperMAG indices respectively, I showed the subsequent transport of plasma across the magnetosphere and the resulting current dynamics, indicating the presence of substorm onset prior to and following the initial dynamic pressure enhancement at 19:00 on 30th October 2021.

Novel observations of AKR by Wind at L1 are presented, that show bursts that exceed the 10 year average from the same LT by 3 orders of magnitude. Bursts are observed when Wind is further from the magnetic equator, suggesting a longitudinal and latitudinal viewing effect. SSUSI auroral observations show discrete aurora in the afternoon sector that correlate with the bursts, and an occasion of diffuse aurora in the morning sector during AKR. This makes direct inference of a dayside AKR source uncertain but likely corresponds to the discrete aurora for this period, which also correlates with nightside substorm activity. While L1 observations are useful when comprehensive conjugate observations are available, more work is needed to supplement usual proxies of magnetospheric disturbance with remote Wind/WAVES radio measurements of AKR from L1.

Chapter 7

Summary and Future Work

7.1 Research Summary

This thesis has involved the development of an unprecedented dataset of remote, continuous AKR observations with Wind/Waves that spans, where viewing is optimal, from November 1994 to 2004 at a consistent 3 minute resolution. Further observations from when Wind is at L1 are also available from 2004 onwards. Using a novel technique that allows for a full calibration of the emission, whereby the normalised intensity across a single linear radio antenna in a specific geometry is used to characterise the variability, other radio emissions (such as the background spectrum and ubiquitous solar radio bursts) are removed from the database with quick application of a simple pipeline (see chapter 4). Data produced via this selection has been used in this thesis on both a case study and statistical basis to study AKR.

As the Wind/Waves observations are near-continuous it is possible to apply the selection to the raw data relatively quickly (a single day of observations takes $\sim$ 3 minutes to process on an average laptop) to any date. If others in the space physics community were interested in the use of this data product, to compare the timing of AKR with other magnetospheric processes for example, they can do so via the MASER (Measuring Analyzing & Simulating Emissions in Radio frequencies) (Cecconi et al., 2020) online data repository where the first ten years of Wind data (1995-2004 inclusive) are available at the time of writing (Waters et al., 2021b). In the future, this repository will be kept updated with any Wind/Waves observations to which the selection is applied and is in the published literature, and the programs used for data processing are being compiled in a repository with documentation for future use.

By way of validation of the selection technique, as well as a first multipoint observation over which to apply it, the flyby of Earth by the Cassini spacecraft was the initial case study used for analysis of the data. The differing orbital trajectories of the

Wind and Cassini spacecraft over a 30 day period were considered and used to compare the observations with known AKR viewing constraints. Previously observed periodicities in the emission were found, and while the exact source of this variability was not uncovered, the presence of the periodicity itself and reproduction of viewing constraints with local time and magnetic latitude confirmed the effectiveness of the selection (see also chapter 4).

By applying the selection to a larger breadth of the Wind AKR data, during which the spacecraft explored the full extent of local times in and around the magnetosphere, a first statistical analysis was facilitated. The existing literature of different observational methods of determining substorm onset times was used in conjunction with the AKR observations to explore the radio power response during the timeline of these events. Over a timescale that had not yet been explored in this context, the low frequency component of the AKR was shown to contribute more significantly, both in occurrence and in sense of the total power output of AKR at substorm onset, on average (see chapter 5).

As a proof of concept, the AKR selection was applied on a case study basis during a period of solar activity that was one of the largest of the current rising phase of the solar cycle. Although Wind was situated at L1 on the dayside, AKR was still observed and compared with auroral observations on the polar dayside to show that discrete aurora related to substorm activity followed typical acceleration processes that are seen on the nightside. This case study illustrated the chain of events in the terrestrial system following the arrival of a coronal mass ejection at 1 AU, and showed the potential for the use of Wind data since 2005 to the present day, made from L1 (see chapter 6).

7.2 Future Work

7.2.1 AKR Visibility

The dataset of AKR observations with Wind/Waves developed during this thesis spans 25+ years and has the largest temporal span of such emission to date, albeit from varied viewing positions; given the complex orbit of Wind and the various mission planning objectives throughout its lifetime, it has explored a wide variety of local times and magnetic latitudes at varying radial distances from the Earth. While the average AKR power for the first 10 years of the orbit, during which the most ideal viewing positions for AKR were covered, were examined in Chapter 5, this was only analysed in a qualitative sense. As has been seen in this thesis, the AKR intensity can vary due to intrinsic source variability, due to its coupling with magnetospheric dynamics, as well as the latitude and local time of a remote observer. The breadth of

Wind's observing positions, the latter and remaining years of dayside AKR observations of Wind, and the opportunities for coincident observations from both ground- and space-based instruments throughout the mission lifetime, there is scope to characterise the viewing from all positions quantitatively. While the modelling techniques described below, geomagnetic indices and radio observations could be used to fully quantify the visibility, although this is complex and requires a lot of time. Examining the distribution of AKR power in LT and magnetic latitude over all Wind observations achieves this in a less complete but more efficient sense, and could allow a correction factor to be derived and applied. Simply subsetting the data can be effective to account for viewing has been seen to be effective in chapter 5, and these subsets can be informed by such work.

Spacecraft in the past have had various orbital profiles that allow them to observe AKR and explore aspects of its visibility. The Polar and IMAGE spacecraft, for example, were both equipped with radio instrumentation and have highly-inclined, elliptical orbits which mean that they spend a lot of time far above the poles, within the AKR beams; the Polar spacecraft had a perigee and apogee of 2.2 R_E and 9 R_E in geocentric radial distance. The Geotail spacecraft observes from much further away, sometimes at $\sim$100 R_E, and often near the equatorial plane, placing it ideally to see emission cones of both Northern and Southern AKR sources on the nightside. The Cluster spacecraft are in a highly elliptical orbit like Polar and IMAGE rely on the radial distance (apogee at 22 R_E) and high latitude positions of the orbit to make *in-situ* observations of the auroral acceleration region (Forsyth et al., 2012) as well as radio observations. Mutel et al. (2008) have performed the most exact determination of the AKR source region beaming to date based on observations with Cluster, while Xiao et al. (2007, 2016) have developed a ray-tracing model of the AKR specifically to examine propagation pathways and explain occurrences of AKR from a given spacecraft position. Louis et al. (2019) has used forward modelling to simulate observations based on magnetospheric parameters at source regions of cyclotron maser instability-generated emission at Jupiter. A combination of methods can be used on both a case study and eventually a statistical basis to constrain the source of variability for future observations. Multi-spacecraft observations can also deliver insight and context to these studies; as has been seen in chapter 4 with Wind and Cassini, a multipoint observation provides a rare insight into global AKR visibility and dynamics. The Polar, Geotail and IMAGE spacecraft, as well as others such as STEREO and newer and future missions such as the Parker Solar Probe, Solar Orbiter and JUICE, all have the potential to be used with Wind for this purpose, when an overlap in the operating timeline of the various instruments exists.

7.2.2 Daily, Seasonal and Solar Cycle Variations in AKR Intensity and Spectrum

As mentioned in the previous section 7.2.1, the temporal scale of the Wind AKR dataset is large compared to previous datasets and this allows for comprehensive analysis of the AKR variability over long timescales; specifically it allows for examination of solar cycle ($\sim$ 11 years) and seasonal effects. Once the spacecraft viewing position has been accounted for, which can be done by various means, the continuous time series of AKR observations (at present $\sim$ 20 years from 1995 to the present) will be able to be explored at these timescales. Previously, solar cycle dependencies have only been possible to explore by using AKR observations made by different instruments from successive solar minima and solar maxima (Green, 2004). A continuous time series will allow for a clearer determination of the effect of changes in the solar wind during more active and quieter times at solar maximum and minimum, respectively. Variations in spectral morphology based on seasonal changes such as the dipole tilt will also be able to be explored. Studies that have observed this phenomenon describe it as a result of changes in the plasma density cavity from seasonal solar illumination but other explanations are also presented (Green, 2004; Morioka et al., 2013); these can be tested further with Wind observations.

Diurnal variations have been observed as present in AKR by various authors, including work done for this thesis. The physical significance of this variation is not clear, however; the beaming pattern of given AKR source regions will tilt with the magnetic dipole during a diurnal rotation such that a remote spacecraft may be illuminated at this period by these extremes, but other potential causes in the ionosphere and AKR source region itself, such as the density of the ionospheric plasma, also follow a diurnal modulation due to the same tilt and have been explored as a cause of this periodicity as well (Panchenko et al., 2009; Lamy et al., 2010; Morioka et al., 2013).

The spectral nature of AKR emissions can also be explored, where allowed by aforementioned visibility effects, over these various timescales, which provides a proxy for the extent of the auroral acceleration region as has been seen. The correlation of AKR enhancement with substorms is clear, although the consistency of the relationship between the acceleration region evolution has not been studied over long periods such as those made achievable by Wind. In particular, the higher frequency, low altitude sources of AKR do intensify during substorms, but are also seen to show variability when there is less well-defined substorm activity. The variability of all spectral components of AKR is worth studying, therefore, and many avenues for exploration can be achieved by integrating the radio power over other spectral ranges than performed here, as a first step.

7.2.3 Multipoint Observations of Substorms with MIRACLE Auroral Cameras

MIRACLE (Syrjäsuo et al., 1998) has been used as a way of studying electrodynamics and auroral morphology in general during substorms (e.g. Partamies et al., 2015), and comprises a network of all-sky CCD cameras at auroral latitudes in the Northern hemisphere. By using coincident measurements of the aurora with this network, remote AKR observations with Wind, and lists of substorms such as those utilised in chapter 5, it is possible to perform quantitative analysis of the auroral emission altitude (Whiter et al., 2013; Partamies et al., 2022) and, by again using the AKR observations as a proxy for the extent of the auroral acceleration region, to provide an insight into magnetosphere-ionosphere coupling and its associated timescales.

7.2.4 Machine Learning

Long timescale observations (a decade or more) have been made of auroral radio emissions from Earth, Jupiter and Saturn. The Jovian radio spectrum has been observed from the ground with, for example, the Nançay Decameter Array (Boischot et al., 1980), and radio emissions at Saturn were observed for 13 years by Cassini. Machine learning has been broadly utilised in magnetospheric physics and many other fields as an effective tool to isolate classes based on automatic, artificial recognition of distinctive sets of parameters within data. Long term radio datasets can be ideal for this purpose, once viewing effects and other idiosyncrasies are handled, but require extensive labelling to form catalogs of features in the data. Advancing on labelling data by hand, features can now be selected from dynamic spectrograms to quickly retrieve their frequency-time structure (Louis et al., 2022). Once compiled, these form extremely effective tools to explore radio observations and the components of auroral radio emissions on a statistical basis (Marques et al., 2017; Jácome et al., 2022), and also allow for training of machine learning algorithms.

Semantic segmentation is a class of machine learning that recognises parts of images and, once an algorithm is trained, can be extended to a larger set of data to produce classified data that can be explored statistically. While this has begun to be done with the analogue of the AKR at Saturn (O' Dwyer et al., 2022), it is yet to be applied to AKR observations. This could, for example, allow a database of low-frequency extension of AKR to be produced. In this way the occurrence and characteristics of high altitude AKR sources could be compared to other lists of substorm onsets to further constrain this relationship and explore the possibility of using remote AKR observations themselves as another reliable indicator of substorm dynamics.

References

S. I. Akasofu. The development of the auroral substorm. *Planetary and Space Science*, 12 (4):273–282, 1964. ISSN 00320633. .

Syun Ichi Akasofu. Auroral Substorms: Search for Processes Causing the Expansion Phase in Terms of the Electric Current Approach. *Space Science Reviews*, 212(1-2): 341–381, 2017. ISSN 15729672. . URL http://dx.doi.org/10.1007/s11214-017-0363-7.

Syun-Ichi Akasofu. A Review of Studies of Geomagnetic Storms and Auroral/Magnetospheric Substorms Based on the Electric Current Approach. *Frontiers in Astronomy and Space Sciences*, 7(January):1–20, 2021. .

J K Alexander and M L Kaiser. Terrestrial kilometric radiation, 1. Spatial structure studies. *Journal of Geophysical Research*, 81(34):5948–5956, dec 1976. ISSN 01480227. . URL http://doi.wiley.com/10.1029/JA081i034p05948.

Joseph K. Alexander and Michael L. Kaiser. Terrestrial kilometric radiation, 2. Emission from the magnetospheric cusp and dayside magnetosheath. *Journal of Geophysical Research*, 82(1):98–104, jan 1977. ISSN 01480227. . URL http://doi.wiley.com/10.1029/JA082i001p00098.

Roger R Anderson, Hiroshi Matsumoto, Kozo Hashimoto, Hirotsugu Kojima, Yasumasa Kasaba, Michael L Kaiser, Jean Louis Bougeret, Jean Louis Steinberg, and Gordon Rostoker. Geotail, Polar, and Wind Observations of Auroral Kilometric Radiation. *COSPAR Colloquia Series*, 16(C):205–219, 2005. ISSN 09642749. .

Tohru Araki. A Physical Model of the Geomagnetic Sudden Commencement. Geophysical Monograph Series, pages 183–200. American Geophysical Union, Washington, D. C., jan 1994. ISBN 9781118663943. . URL http://doi.wiley.com/10.1029/GM081p0183http://doi.wiley.com/10.1029/GM081.

Wolfgang Baumjohann and R. Treumann. *Basic Space Plasma Physics - Revised Edition*. 03 2012. ISBN 978-1-84816-894-7. .

A. Boischot, C. Rosolen, M. G. Aubier, G. Daigne, F. Genova, Y. Leblanc, A. Lecacheux, J. de La Noe, and B. Moller-Pedersen. A new high-grain, broadband, steerable array to study Jovian decametric emission. *Icarus*, 43(3):399–407, September 1980. .

Joseph E. Borovsky. Canonical correlation analysis of the combined solar wind and geomagnetic index data sets. *Journal of Geophysical Research: Space Physics*, 119(7): 5364–5381, jul 2014. ISSN 21699380. . URL http://doi.wiley.com/10.1002/2015JA021094http://doi.wiley.com/10.1002/2013JA019607.

Joseph E. Borovsky and Kateryna Yakymenko. Substorm occurrence rates, substorm recurrence times, and solar wind structure. *Journal of Geophysical Research: Space Physics*, 122(3):2973–2998, mar 2017. ISSN 2169-9380. . URL https://onlinelibrary.wiley.com/doi/abs/10.1002/2016JA023625.

J. L. Bougeret, M. L. Kaiser, P. J. Kellogg, R. Manning, K. Goetz, S. J. Monson, N. Monge, L. Friel, C. A. Meetre, C. Perche, L. Sitruk, and S. Hoang. WAVES: The radio and plasma wave investigation on the wind spacecraft. *Space Sci. Rev.*, 71(1-4): 231–263, feb 1995. . URL http://link.springer.com/10.1007/BF00751331.

S. D. Browett, R. C. Fear, A. Grocott, and S. E. Milan. Timescales for the penetration of IMF B y into the Earth's magnetotail. *Journal of Geophysical Research: Space Physics*, 122(1):579–593, jan 2017. ISSN 2169-9380. . URL https://onlinelibrary.wiley.com/doi/abs/10.1002/2016JA023198.

G. E. Brueckner, R. A. Howard, M. J. Koomen, C. M. Korendyke, D. J. Michels, J. D. Moses, D. G. Socker, K. P. Dere, P. L. Lamy, A. Llebaria, M. V. Bout, R. Schwenn, G. M. Simnett, D. K. Bedford, and C. J. Eyles. The Large Angle Spectroscopic Coronagraph (LASCO). *Solar Physics*, 162(1-2):357–402, dec 1995. ISSN 0038-0938. . URL http://link.springer.com/10.1007/BF00733434.

W. Calvert. The auroral plasma cavity. *Geophysical Research Letters*, 8(8):919–921, aug 1981. ISSN 00948276. . URL http://doi.wiley.com/10.1029/GL008i008p00919.

H. V. Cane. Spectra of the non-thermal radio radiation from the galactic polar regions. *Monthly Notices of the Royal Astronomical Society*, 189(3):465–478, dec 1979. ISSN 0035-8711. URL https://ui.adsabs.harvard.edu/abs/1979MNRAS.189..465C/abstracthttps://academic.oup.com/mnras/article-lookup/doi/10.1093/mnras/189.3.465.

J. A. Carter, S. E. Milan, A. R. Fogg, L. J. Paxton, and B. J. Anderson. The Association of High-Latitude Dayside Aurora With NBZ Field-Aligned Currents. *Journal of Geophysical Research: Space Physics*, 123(5):3637–3645, 2018. ISSN 21699402. .

Jennifer A. Carter, Stephen E. Milan, Alexandra R. Fogg, Harneet Sangha, Mark Lester, Larry J. Paxton, and Brian J. Anderson. The Evolution of Long-Duration Cusp Spot

Emission During Lobe Reconnection With Respect to Field-Aligned Currents. *Journal of Geophysical Research: Space Physics*, 125(7), 2020. ISSN 21699402. .

B. Cecconi. Polarization in Low Frequency Radio Astronomy. *arXiv:1901.03599*, pages 1–26, 2019. URL http://arxiv.org/abs/1901.03599.

B. Cecconi and P. Zarka. Direction finding and antenna calibration through analytical inversion of radio measurements performed using a system of two or three electric dipole antennas on a three-axis stabilized spacecraft. *Radio Science*, 40(3):1–20, 2005. ISSN 00486604. .

B. Cecconi, L. Lamy, and P. Zarka. Cassini/rpws/hfr lesia/kronos n3d data collection (version 1.0) [data set]. *PADC*, 2017. .

Baptiste Cecconi, Alan Loh, Pierre Le Sidaner, Renaud Savalle, Xavier Bonnin, Quynh Nhu Nguyen, Sonny Lion, Albert Shih, Stéphane Aicardi, Philippe Zarka, Corentin Louis, Andrée Coffre, Laurent Lamy, Laurent Denis, Jean Mathias Grießmeier, Jeremy Faden, Chris Piker, Nicolas André, Vincent Génot, Stéphane Erard, Joseph N. Mafi, Todd A. King, Jim Sky, and Markus Demleitner. MASER: A science ready toolbox for low frequency radio astronomy. *Data Science Journal*, 19(1): 1–7, 2020. ISSN 16831470. .

C. Robert Clauer and Robert L. McPherron. Mapping the local time-universal time development of magnetospheric substorms using mid-latitude magnetic observations. *Journal of Geophysical Research (1896-1977)*, 79(19):2811–2820, 1974. . URL https://agupubs.onlinelibrary.wiley.com/doi/abs/10.1029/JA079i019p02811.

J. C. Coxon, S. E. Milan, L. B.N. Clausen, B. J. Anderson, and H. Korth. A superposed epoch analysis of the regions 1 and 2 Birkeland currents observed by AMPERE during substorms. *Journal of Geophysical Research: Space Physics*, 119(12):9834–9846, 2014. ISSN 21699402. .

E. A. Davey, M. Lester, S. E. Milan, R. C. Fear, and C. Forsyth. The orientation and current density of the magnetotail current sheet: A statistical study of the effect of geomagnetic conditions. *Journal of Geophysical Research (Space Physics)*, 117(A7): A07217, July 2012. .

T. Neil Davis and Masahisa Sugiura. Auroral electrojet activity index AE and its universal time variations. *Journal of Geophysical Research*, 71(3):785–801, feb 1966. ISSN 01480227. . URL http://doi.wiley.com/10.1029/JZ071i003p00785.

G. A. Dulk, W. C. Erickson, R. Manning, and J.-L. Bougeret. Calibration of low-frequency radio telescopes using the galactic background radiation. *Astronomy & Astrophysics*, 365(2):294–300, 2001.

M. W. Dunlop, J. Y. Yang, Y. Y. Yang, C. Xiong, H. Lühr, Y. V. Bogdanova, C. Shen, N. Olsen, Q. H. Zhang, J. B. Cao, H. S. Fu, W. L. Liu, C. M. Carr, P. Ritter, A. Masson, and R. Haagmans. Simultaneous field-aligned currents at Swarm and Cluster satellites. *Geophysical Research Letters*, 42(10):3683–3691, 2015. ISSN 19448007. .

R. E. Ergun, C. W. Carlson, J. P. McFadden, F S Mozer, G. T. Delory, W Peria, C. C. Chaston, M Temerin, R. Elphic, R. Strangeway, R Pfaff, C A Cattell, D. Klumpar, E Shelley, W Peterson, E. Moebius, and L Kistler. FAST satellite observations of electric field structures in the auroral zone. *Geophysical Research Letters*, 25(12): 2025–2028, jun 1998. ISSN 00948276. . URL http://doi.wiley.com/10.1029/98GL00635.

R. E. Ergun, C. W. Carlson, J. P. McFadden, G. T. Delory, R. J. Strangeway, and P. L. Pritchett. Electron-Cyclotron Maser Driven by Charged-Particle Acceleration from Magnetic Field–aligned Electric Fields. *The Astrophysical Journal*, 538(1):456–466, jul 2000. ISSN 0004-637X. . URL https://iopscience.iop.org/article/10.1086/309094.

R. E. Ergun, Y. J. Su, L. Andersson, C. W. Carlson, J. P. McFadden, F. S. Mozer, D. L. Newman, M. V. Goldman, and R. J. Strangeway. Direct observation of localized parallel electric fields in a space plasma. *Physical Review Letters*, 87(4): 45003–1–45003–4, 2001. ISSN 10797114. .

D. H. Fairfield, T. Mukai, M. Brittnacher, G. D. Reeves, S. Kokubun, G. K. Parks, T. Nagai, H. Matsumoto, K. Hashimoto, D. A. Gurnett, and T. Yamamoto. Earthward flow bursts in the inner magnetotail and their relation to auroral brightenings, AKR intensifications, geosynchronous particle injections and magnetic activity. *Journal of Geophysical Research: Space Physics*, 104(A1):355–370, 1999. ISSN 2156-2202. .

R. C. Fear and S. E. Milan. The IMF dependence of the local time of transpolar arcs: Implications for formation mechanism. *Journal of Geophysical Research: Space Physics*, 117(3), 2012. ISSN 21699402. .

Alexandra Ruth Fogg, C M Jackman, J E Waters, X Bonnin, L Lamy, and B Cecconi. [Accepted] Wind / WAVES observations of Auroral Kilometric Radiation : automated burst detection and Terrestrial Solar Wind - Magnetosphere coupling effects. *Journal of Geophysical Research: Space Physics*, pages 1–28, 2021.

Alexandra Ruth Fogg, C M Jackman, J E Waters, X Bonnin, L Lamy, and B Cecconi. Wind / WAVES observations of Auroral Kilometric Radiation : automated burst detection and Terrestrial Solar Wind - Magnetosphere coupling effects. *Journal of Geophysical Research: Space Physics*, pages 1–28, 2022.

C. Forsyth, A. N. Fazakerley, A. P. Walsh, C. E.J. Watt, K. J. Garza, C. J. Owen, D. Constantinescu, I. Dandouras, K. H. Fornaçon, E. Lucek, G. T. Marklund, S. S.

Sadeghi, Y. Khotyaintsev, A. Masson, and N. Doss. Temporal evolution and electric potential structure of the auroral acceleration region from multispacecraft measurements. *Journal of Geophysical Research: Space Physics*, 117(12):1–18, 2012. ISSN 21699402. .

C. Forsyth, A. N. Fazakerley, I. J. Rae, C. E.J. Watt, K. Murphy, J. A. Wild, T. Karlsson, R. Mutel, C. J. Owen, R. Ergun, A. Masson, M. Berthomier, E. Donovan, H. U. Frey, J. Matzka, C. Stolle, and Y. Zhang. In situ spatiotemporal measurements of the detailed azimuthal substructure of the substorm current wedge. *Journal of Geophysical Research A: Space Physics*, 119(2):927–946, 2014. ISSN 21699402. .

C Forsyth, I J Rae, J C Coxon, M P Freeman, C M Jackman, J Gjerloev, and A N Fazakerley. A new technique for determining Substorm Onsets and Phases from Indices of the Electrojet (SOPHIE). *Journal of Geophysical Research: Space Physics*, 120 (12):10,592–10,606, dec 2015. ISSN 21699380. . URL http://doi.wiley.com/10.1002/2015JA021343.

C. Forsyth, M. Shortt, J. C. Coxon, I. J. Rae, M. P. Freeman, N. M.E. Kalmoni, C. M. Jackman, B. J. Anderson, S. E. Milan, and A. G. Burrell. Seasonal and Temporal Variations of Field-Aligned Currents and Ground Magnetic Deflections During Substorms. *Journal of Geophysical Research: Space Physics*, 123(4):2696–2713, 2018. ISSN 21699402. .

L. A. Frank and K. L. Ackerson. Observations of charged particle precipitation into the auroral zone. *Journal of Geophysical Research*, 76(16):3612–3643, 1971. .

H. U. Frey. Substorm onset observations by IMAGE-FUV. *Journal of Geophysical Research*, 109(A10):A10304, 2004. ISSN 0148-0227. . URL http://doi.wiley.com/10.1029/2004JA010607.

S. A. Fuselier and W. S. Lewis. Properties of near-earth magnetic reconnection from in-situ observations. *Space Science Reviews*, 160(1-4):95–121, 2011. ISSN 00386308. .

Dennis L. Gallagher and Donald A. Gurnett. Auroral Kilometric Radiation: Time-Averaged Source Location. *Journal of Geophysical Research*, 84(A11):6501–6509, 1979. ISSN 01480227. .

J. W. Gjerloev. The SuperMAG data processing technique. *Journal of Geophysical Research: Space Physics*, 117(9):1–19, 2012. ISSN 21699402. .

J. W. Gjerloev, R. A. Hoffman, E. Tanskanen, M. Friel, L. A. Frank, and J. B. Sigwarth. Auroral electrojet configuration during substorm growth phase. *Geophysical Research Letters*, 30(18):1–4, 2003. ISSN 00948276. .

J T Gosling, S. J. Bame, D. J. McComas, and J. L. Phillips. Coronal mass ejections and large geomagnetic storms. *Geophysical Research Letters*, 17(7):901–904, jun 1990. ISSN 00948276. . URL http://doi.wiley.com/10.1029/GL017i007p00901.

James L. Green. Seasonal and solar cycle dynamics of the auroral kilometric radiation source region. *Journal of Geophysical Research*, 109(A5):A05223, 2004. ISSN 0148-0227. . URL http://doi.wiley.com/10.1029/2003JA010311.

James Lauer Green, Donald A. Gurnett, and Stanley D. Shawhan. The angular distribution of auroral kilometric radiation. *Journal of Geophysical Research*, 82(13): 1825–1838, may 1977. ISSN 01480227. . URL http://doi.wiley.com/10.1029/JA082i013p01825.

James Lauer Green, Nicolaos A. Saflekos, Donald A. Gurnett, and Thomas A. Potemra. A correlation between auroral kilometric radiation and field-aligned currents. *Journal of Geophysical Research*, 87(A12):10463, 1982. ISSN 0148-0227. . URL http://doi.wiley.com/10.1029/JA087iA12p10463.

H. Gunell, L. Andersson, J. De Keyser, and I. Mann. Self-consistent electrostatic simulations of reforming double layers in the downward current region of the aurora. *Annales Geophysicae*, 33(10):1331–1342, 2015. ISSN 14320576. .

Donald A. Gurnett. The Earth as a radio source: Terrestrial kilometric radiation. *Journal of Geophysical Research*, 79(28):4227–4238, oct 1974. . URL http://doi.wiley.com/10.1029/JA079i028p04227.

John D Haiducek, Daniel T Welling, Steven K Morley, Natalia Yu Ganushkina, and Xiangning Chu. Using multiple signatures to improve accuracy of substorm identification. *Journal of Geophysical Research: Space Physics*, mar 2020. ISSN 2169-9380. . URL https://onlinelibrary.wiley.com/doi/abs/10.1029/2019JA027559.

J Hanasz, M Y Boudjada, R Schreiber, Z Krawczyk, M Malycha, M M Mogilevsky, H O Rucker, and T V Romantsova. Dynamic spectra of the Stokes parameters for the dayside and nightside auroral kilometric radiation. *Geophysical Research Letters*, 27 (11):1631–1634, jun 2000. ISSN 00948276. . URL http://doi.wiley.com/10.1029/1999GL010770.

J Hanasz, H. de Feraudy, R Schreiber, G Parks, M Brittnacher, M M Mogilevsky, and T V Romantsova. Wideband bursts of auroral kilometric radiation and their association with UV auroral bulges. *Journal of Geophysical Research: Space Physics*, 106 (A3):3859–3871, mar 2001. ISSN 01480227. . URL http://doi.wiley.com/10.1029/2000JA900098.

J. Hanasz, M. Panchenko, H. De Feraudy, R. Schreiber, and M. M. Mogilevsky. Occurrence distributions of the auroral kilometric radiation ordinary and extraordinary wave modes. *Journal of Geophysical Research: Space Physics*, 108(A11), 2003. ISSN 21699402. .

D S Hillan, Iver H Cairns, P A Robinson, and A Mohamed. Prediction of background levels for the Wind WAVES instrument and implications for the galactic background radiation. *Journal of Geophysical Research: Space Physics*, 115(A6):1–11, 2010.

R. L. Huff, W. Calvert, J. D. Craven, L. A. Frank, and D. A. Gurnett. Mapping of auroral kilometric radiation sources to the aurora. *Journal of Geophysical Research*, 93 (A10):11445, oct 1988. ISSN 0148-0227. . URL http://doi.wiley.com/10.1029/JA093iA10p11445.

R. D. Hunsucker and J. K. Hargreaves. *The High-Latitude Ionosphere and its Effects on Radio Propagation*. 2002.

J. A. Hutchinson, D. M. Wright, and S. E. Milan. Geomagnetic storms over the last solar cycle: A superposed epoch analysis. *Journal of Geophysical Research: Space Physics*, 116(9):1–16, 2011. ISSN 21699402. .

W. L. Imhof, M. Walt, R. R. Anderson, D. L. Chenette, J. D. Hawley, J. Mobilia, and S. M. Petrinec. Association of electron precipitation with auroral kilometric radiation. *Journal of Geophysical Research: Space Physics*, 105(A1):277–289, 2000. ISSN 21699402. .

Toshihiko Iyemori. Storm-time magnetospheric currents inferred from mid-latitude geomagnetic field variations. *Journal of geomagnetism and geoelectricity*, 42(11): 1249–1265, 1990. ISSN 0022-1392. . URL http://www.jstage.jst.go.jp/article/jgg1949/42/11/42{_}11{_}1249/{_}article.

H. R. P. Jácome, M. S. Marques, P. Zarka, E. Echer, L. Lamy, and C. K. Louis. Search for Jovian decametric emission induced by Europa on the extensive Nançay Decameter Array catalog. *Astronomy & Astrophysics*, 665:A67, 2022. ISSN 0004-6361. .

L. Juusola, N. Østgaard, E. Tanskanen, N. Partamies, and K. Snekvik. Earthward plasma sheet flows during substorm phases. *Journal of Geophysical Research: Space Physics*, 116(A10):n/a–n/a, oct 2011. ISSN 01480227. . URL http://doi.wiley.com/10.1029/2011JA016852.

M L Kaiser and J K Alexander. Relationship between auroral substorms and the occurrence of terrestrial kilometric radiation. 82(32), 1977a.

M L Kaiser and J K Alexander. Terrestrial Kilometric Radiation III. Average Spectral Properties. 82(22), 1977b.

M. L. Kaiser, J. K. Alexander, A. C. Riddle, J. B. Pearce, and J W Warwick. Direct measurements by Voyagers 1 and 2 of the polarization of terrestrial kilometric radiation. *Geophysical Research Letters*, 5(10):857–860, oct 1978. ISSN 00948276. . URL http://doi.wiley.com/10.1029/GL005i010p00857.

N M E Kalmoni, I J Rae, C E J Watt, K R Murphy, C Forsyth, and C J Owen. Statistical characterization of the growth and spatial scales of the substorm onset arc. *Journal of Geophysical Research*, 120(1):1–14, 2015. ISSN 21699402. URL http://adsabs.harvard.edu/cgi-bin/nph-data{_}query?bibcode=2015JGRA..120.8503K{&}link{_}type=EJOURNAL{%}5Cnpapers3://publication/doi/10.1002/2015JA021470.

Y. Kasaba, H Matsumoto, K Hashimoto, and R. R. Anderson. The angular distribution of auroral kilometric radiation observed by the GEOTAIL spacecraft. *Geophysical Research Letters*, 24(20):2483–2486, oct 1997. ISSN 00948276. . URL http://doi.wiley.com/10.1029/97GL02599.

Andreas Keiling. The Dynamics of the Alfvénic Oval. *Journal of Atmospheric and Solar-Terrestrial Physics*, 219, 2021. ISSN 13646826. .

L. Kepko, R. L. McPherron, O. Amm, S. Apatenkov, W. Baumjohann, J. Birn, M. Lester, R. Nakamura, T. I. Pulkkinen, and V. Sergeev. Substorm Current Wedge Revisited. *Space Science Reviews*, 190(1-4):1–46, 2015. ISSN 15729672. . URL http://dx.doi.org/10.1007/s11214-014-0124-9.

E. K.J. Kilpua, A. Balogh, R. von Steiger, and Y. D. Liu. Geoeffective Properties of Solar Transients and Stream Interaction Regions. *Space Science Reviews*, 212(3-4):1271–1314, 2017. ISSN 15729672. . URL http://dx.doi.org/10.1007/s11214-017-0411-3.

T. Kimura, L. Lamy, C. Tao, S. V. Badman, S. Kasahara, B. Cecconi, P. Zarka, A. Morioka, Y. Miyoshi, D. Maruno, Y. Kasaba, and M. Fujimoto. Long-term modulations of Saturn's auroral radio emissions by the solar wind and seasonal variations controlled by the solar ultraviolet flux. *Journal of Geophysical Research: Space Physics*, 118(11):7019–7035, 2013. ISSN 21699402. .

Margaret G. Kivelson and Christopher T. Russell. *Introduction to Space Physics*. 1995.

V. Krupar, M. Maksimovic, E. P. Kontar, A. Zaslavsky, O. Santolik, J. Soucek, O. Kruparova, J. P. Eastwood, and A. Szabo. Interplanetary Type III Bursts and Electron Density Fluctuations in the Solar Wind. *The Astrophysical Journal*, 857(2):82, 2018. ISSN 0004-637X. . URL http://dx.doi.org/10.3847/1538-4357/aab60f.

A. Kullen and T. Karlsson. On the relation between solar wind, pseudobreakups, and substorms. *Journal of Geophysical Research: Space Physics*, 109(A12):1–20, 2004. ISSN 21699402. .

L. Lamy, P. Zarka, B. Cecconi, S. Hess, and R. Prangé. Modeling of Saturn kilometric radiation arcs and equatorial shadow zone. *Journal of Geophysical Research: Space Physics*, 113(10):1–10, 2008a. ISSN 21699402. .

L. Lamy, P. Zarka, B. Cecconi, R. Prangé, W. S. Kurth, and D. A. Gurnett. Saturn kilometric radiation: Average and statistical properties. *Journal of Geophysical Research: Space Physics*, 113(A7):n/a–n/a, jul 2008b. . URL http://doi.wiley.com/10.1029/2007JA012900.

L. Lamy, P. Zarka, B. Cecconi, and R. Prangé. Auroral kilometric radiation diurnal, semidiurnal, and shorter-term modulations disentangled by Cassini. *Journal of Geophysical Research: Space Physics*, 115(A9):n/a–n/a, sep 2010. ISSN 01480227. . URL http://doi.wiley.com/10.1029/2010JA015434.

D. Le Quéau and A. Roux. Quasi-monochromatic wave-particle interactions in magnetospheric plasmas. *Solar Physics*, 111(1):59–80, mar 1987. ISSN 0038-0938. . URL http://link.springer.com/10.1007/BF00145441.

L. C. Lee, J. R. Kan, and C. S. Wu. Generation of auroral kilometric radiation and the structure of auroral acceleration region. *Planetary and Space Science*, 28(7):703–711, 1980. ISSN 00320633. .

K. Liou. Magnetic dipolarization with substorm expansion onset. *Journal of Geophysical Research*, 107(A7):1131, 2002. ISSN 0148-0227. . URL http://doi.wiley.com/10.1029/2001JA000179.

K Liou, C.-I. Meng, A T Y Lui, P T Newell, and R. R. Anderson. Auroral kilometric radiation at substorm onset. *Journal of Geophysical Research: Space Physics*, 105(A11): 25325–25331, nov 2000. ISSN 01480227. . URL http://doi.wiley.com/10.1029/2000JA000038.

C. K. Louis, S. L.G. Hess, B. Cecconi, P. Zarka, L. Lamy, S. Aicardi, and A. Loh. ExPRES: An Exoplanetary and Planetary Radio Emissions Simulator. *Astronomy and Astrophysics*, 627:1–11, 2019. ISSN 14320746. .

C. K. Louis, C. M. Jackman, S. W. Mangham, K. D. Smith, E. P. O'Dwyer, A. Empey, B. Cecconi, P. Zarka, and S. Maloney. The "SPectrogram Analysis and Cataloguing Environment" (SPACE) Labelling Tool. pages 1–9, 2022. URL https://arxiv.org/abs/2207.12454v1.

A. T.Y. Lui. Cross-tail current evolution during substorm dipolarization. *Annales Geophysicae*, 31(6):1131–1142, 2013. ISSN 09927689. .

R. Manning and J. Fainberg. A New Method of Measuring Radio Source Parameters of a Partially Polarized Distributed Source from Spacecraft Observations. *Space Sci. Instrum.*, 5:161–181, 1980.

M. S. Marques, P. Zarka, E. Echer, V. B. Ryabov, M. V. Alves, L. Denis, and A. Coffre. Statistical analysis of 26 yr of observations of decametric radio emissions from Jupiter. *Astronomy and Astrophysics*, 604, 2017. ISSN 14320746. .

R. L. McPherron, C. T. Russell, and M. P. Aubry. Satellite studies of magnetospheric substorms on August 15, 1968: 9. Phenomenological model for substorms. *Journal of Geophysical Research*, 78(16):3131–3149, 1973. .

Robert L. McPherron. Growth phase of magnetospheric substorms. *Journal of Geophysical Research*, 75(28):5592–5599, oct 1970. ISSN 01480227. . URL http://doi.wiley.com/10.1029/JA075i028p05592.

Robert L. McPherron and Xiangning Chu. The Midlatitude Positive Bay Index and the Statistics of Substorm Occurrence. *Journal of Geophysical Research: Space Physics*, 123 (4):2831–2850, apr 2018. ISSN 21699402. . URL http://doi.wiley.com/10.1002/2017JA024766.

S. B. Mende, H. U. Frey, V. Angelopoulos, and Y. Nishimura. Substorm triggering by poleward boundary intensification and related equatorward propagation. *Journal of Geophysical Research: Space Physics*, 116(4):1–17, 2011. ISSN 21699402. .

J. D. Menietti, R. L. Mutel, I. W. Christopher, K. A. Hutchinson, and J. B. Sigwarth. Simultaneous radio and optical observations of auroral structures: Implications for AKR beaming. *Journal of Geophysical Research: Space Physics*, 116(12):1–9, 2011a. ISSN 21699402. .

J. D. Menietti, R. L. Mutel, I. W. Christopher, K. A. Hutchinson, and J. B. Sigwarth. Simultaneous radio and optical observations of auroral structures: Implications for AKR beaming. *Journal of Geophysical Research: Space Physics*, 116(12):1–9, 2011b. ISSN 21699402. .

N. Meyer-Vernet, K. Issautier, and M. Moncuquet. Quasi-thermal noise spectroscopy: The art and the practice. *Journal of Geophysical Research: Space Physics*, 122(8): 7925–7945, 2017. ISSN 21699402. .

Nicole Meyer-Vernet and Claude Perche. Tool kit for antennae and thermal noise near the plasma frequency. *Journal of Geophysical Research*, 94(A3):2405, 1989. ISSN 0148-0227. . URL http://doi.wiley.com/10.1029/JA094iA03p02405.

Nicole Meyer-Vernet, Sang Hoang, Karine Issautier, Milan Maksimovic, Robert Manning, Michel Moncuquet, and Robert G. Stone. Measuring plasma parameters with thermal noise spectroscopy. *Washington DC American Geophysical Union Geophysical Monograph Series*, 103:205, jan 1998. .

S. E. Milan, G. Provan, and B. Hubert. Magnetic flux transport in the Dungey cycle: A survey of dayside and nightside reconnection rates. *Journal of Geophysical Research: Space Physics*, 112(1):1–13, 2007. ISSN 21699402. .

S. E. Milan, P. D. Boakes, and B. Hubert. Response of the expanding/contracting polar cap to weak and strong solar wind driving: Implications for substorm onset. *Journal of Geophysical Research: Space Physics*, 113(9):1–11, 2008. ISSN 21699402. .

S. E. Milan, A. Grocott, C. Forsyth, S. M. Imber, P. D. Boakes, and B. Hubert. A superposed epoch analysis of auroral evolution during substorm growth, onset and recovery: open magnetic flux control of substorm intensity. *Annales Geophysicae*, 27 (2):659–668, 2009. ISSN 14320576. .

S. E. Milan, J. S. Gosling, and B. Hubert. Relationship between interplanetary parameters and the magnetopause reconnection rate quantified from observations of the expanding polar cap. *Journal of Geophysical Research: Space Physics*, 117(A3): n/a–n/a, mar 2012. ISSN 01480227. . URL http://doi.wiley.com/10.1029/2011JA017082.

A. Morioka, Y. Miyoshi, F. Tsuchiya, H. Misawa, T. Sakanoi, K. Yumoto, R. R. Anderson, J. D. Menietti, and E. F. Donovan. Dual structure of auroral acceleration regions at substorm onsets as derived from auroral kilometric radiation spectra. *Journal of Geophysical Research: Space Physics*, 112(6):1–13, 2007. ISSN 21699402. .

A. Morioka, Y. Miyoshi, Y. Miyashita, Y. Kasaba, H. Misawa, F. Tsuchiya, R. Kataoka, A. Kadokura, T. Mukai, K. Yumoto, D. J. Menietti, G. Parks, K. Liou, F. Honary, and E. Donovan. Two-step evolution of auroral acceleration at substorm onset. *Journal of Geophysical Research: Space Physics*, 115(A11):n/a–n/a, nov 2010. ISSN 01480227. . URL http://doi.wiley.com/10.1029/2010JA015361.

A. Morioka, Y. Miyoshi, F. Tsuchiya, H. Misawa, Y. Kasaba, T. Asozu, S. Okano, A. Kadokura, N. Sato, H. Miyaoka, K. Yumoto, G. K. Parks, F. Honary, J. G. Trotignon, P. M.E. Décréau, and B. W. Reinisch. On the simultaneity of substorm onset between two hemispheres. *Journal of Geophysical Research: Space Physics*, 116(4), 2011. ISSN 21699402. .

A. Morioka, Y. Miyoshi, N. Kitamura, H. Misawa, F. Tsuchiya, J. D. Menietti, and F. Honary. Fundamental characteristics of field-aligned auroral acceleration derived from AKR spectra. *Journal of Geophysical Research: Space Physics*, 117(2):1–15, 2012. ISSN 21699402. .

Akira Morioka, Yoshizumi Miyoshi, Satoshi Kurita, Yasumasa Kasaba, Vassilis Angelopoulos, Hiroaki Misawa, Hirotsugu Kojima, and James P. McFadden. Universal time control of AKR: Earth is a spin-modulated variable radio source. *Journal of Geophysical Research: Space Physics*, 118(3):1123–1131, 2013. ISSN 21699402. .

F. Mottez. Alfven wave acceleration of particles in the aurora. *Plasma Physics and Controlled Fusion*, 57(1), 2014. ISSN 13616587. .

R. L. Mutel, D. A. Gumett, I. W. Christopher, J. S. Pickett, and M. Schlax. Locations of auroral kilometric radiation bursts inferred from multispacecraft wideband Cluster VLBI observations. 1: Description of technique and initial results. *Journal of Geophysical Research: Space Physics*, 108(A11):1–13, 2003. ISSN 21699402. .

R. L. Mutel, D. A. Gurnett, and I. W. Christopher. Spatial and temporal properties of AKR burst emission derived from Cluster WBD VLBI studies. *Annales Geophysicae*, 22(7):2625–2632, 2004. ISSN 09927689. .

Robert L. Mutel, Ivar W. Christopher, and J. S. Pickett. Cluster multispacecraft determination of AKR angular beaming. *Geophysical Research Letters*, 35(7):1–6, 2008. ISSN 00948276. .

P. T. Newell and J. W. Gjerloev. Evaluation of SuperMAG auroral electrojet indices as indicators of substorms and auroral power. *Journal of Geophysical Research: Space Physics*, 116(A12):n/a–n/a, dec 2011. ISSN 01480227. . URL http://doi.wiley.com/10.1029/2011JA016779.

Y. Nishimura, L. Lyons, S. Zou, V. Angelopoulos, and S. Mende. Substorm triggering by new plasma intrusion: THEMIS all-sky imager observations. *Journal of Geophysical Research: Space Physics*, 115(A7):1–14, jul 2010. ISSN 01480227. . URL http://doi.wiley.com/10.1029/2009JA015166.

Y. Nishimura, L. R. Lyons, C. Gabrielse, N. Sivadas, E. F. Donovan, R. H. Varney, V. Angelopoulos, J. M. Weygand, M. G. Conde, and S. R. Zhang. Extreme Magnetosphere-Ionosphere-Thermosphere Responses to the 5 April 2010 Supersubstorm. *Journal of Geophysical Research: Space Physics*, 125(4):1–15, 2020. ISSN 21699402. . URL https://doi.org/10.1029/2019JA027654.

J. C. Novaco and L. W. Brown. Nonthermal galactic emission below 10 megahertz. *The Astrophysical Journal*, 221(A6):114, apr 1978. ISSN 0004-637X. . URL http://adsabs.harvard.edu/doi/10.1086/156009.

E. O' Dwyer, C. M. Jackman, K. Domijan, and L. Lamy. Machine Learning for the Classification of Low Frequency Extensions of Saturn Kilometric Radiation. *Journal of Geophysical Research: Space Physics*, 2022. (in prep).

M. Panchenko. Direction finding of AKR sources with three orthogonal antennas. *Radio Science*, 38(6):n/a–n/a, dec 2003. ISSN 00486604. . URL http://doi.wiley.com/10.1029/2003RS002929.

M. Panchenko, M. L. Khodachenko, A. G. Kislyakov, H. O. Rucker, J. Hanasz, M. L. Kaiser, S. D. Bale, L. Lamy, B. Cecconi, P. Zarka, and K. Goetz. Daily variations of auroral kilometric radiation observed by STEREO. *Geophysical Research Letters*, 36(6): 2–5, 2009. ISSN 00948276.

A. Papaioannou, A. Kouloumvakos, A. Mishev, R. Vainio, I. Usoskin, K. Herbst, A. P. Rouillard, A. Anastasiadis, J. Gieseler, R. Wimmer-Schweingruber, and P. Kühl. The First Ground Level Enhancement of Solar Cycle 25 on 28 October 2021. *Astronomy and Astrophysics*, 71(September 2017):1–9, feb 2022. URL http://arxiv.org/abs/2202.07927.

N. E. Papitashvili and J. H. King. Omni 1-min data [data set]. *NASA Space Physics Data Facility*, 2020. .

N. Partamies, L. Juusola, D. Whiter, and K. Kauristie. Substorm evolution of auroral structures. *Journal of Geophysical Research: Space Physics*, 120(7):5958–5972, jul 2015. ISSN 21699380. . URL http://doi.wiley.com/10.1002/2015JA021217.

Noora Partamies, Daniel Whiter, Kirsti Kauristie, and Stefano Massetti. Magnetic local time (MLT) dependence of auroral peak emission height and morphology. *Annales Geophysicae*, 40(5):605–618, oct 2022. ISSN 1432-0576. . URL https://angeo.copernicus.org/articles/40/605/2022/.

Larry J. Paxton, Ching-I. Meng, Glen H. Fountain, Bernard S. Ogorzalek, Edward H. Darlington, Stephen A. Gary, John O. Goldsten, David Y. Kusnierkiewicz, Susan C. Lee, Lloyd A. Linstrom, Jeffrey J. Maynard, Keith Peacock, David F. Persons, and Brian E. Smith. Special Sensor Ultraviolet Spectrographic Imager: An Instrument Description. *Instrumentation for Planetary and Terrestrial Atmospheric Remote Sensing*, 1745(June 1992):2–15, 1992. .

B. M. Pedersen, R. Pottelette, L. Eliasson, J. S. Murphree, R. D. Elphinstone, A. Bahnsen, and M. Jespersen. Auroral kilometric radiation from transpolar arcs. *Journal of Geophysical Research*, 97(A7):10567, 1992. ISSN 0148-0227. . URL http://doi.wiley.com/10.1029/92JA00410.

Joseph N. Pelton and Firooz Allahdadi. *Handbook of Cosmic Hazards and Planetary Defense*. Springer International Publishing, Cham, 2015. ISBN 978-3-319-03951-0. . URL http://link.springer.com/10.1007/978-3-319-03952-7.

T. I. Pulkkinen, H. E. J. Koskinen, and R. J. Pellinen. Mapping of auroral arcs during substorm growth phase. *Journal of Geophysical Research*, 96(A12):21087, 1991. ISSN 0148-0227. .

Marc Pulupa, Stuart D. Bale, Samuel T. Badman, John W. Bonnell, Anthony W. Case, Thierry Dudok de Wit, Keith Goetz, Peter R. Harvey, Alexander M. Hegedus, Justin C. Kasper, Kelly E. Korreck, Vladimir Krasnoselskikh, Davin Larson, Alain Lecacheux, Roberto Livi, Robert J. MacDowall, Milan Maksimovic, David M. Malaspina, Juan Carlos Martínez Oliveros, Nicole Meyer-Vernet, Michel Moncuquet, Michael Stevens, and Phyllis Whittlesey. Statistics and Polarization of Type III Radio Bursts Observed in the Inner Heliosphere. *The Astrophysical Journal Supplement Series*, 246(2):49, 2019. ISSN 1538-4365. . URL http://arxiv.org/abs/1912.03371{%}0A.

M. J. Reiner, J. Fainberg, M. L. Kaiser, and J. L. Bougeret. Circular polarization observed in interplanetary type III radio storms. *Solar Physics*, 241(2):351–370, 2007. ISSN 00380938. .

S. Sadeghi and M. R. Emami. Multi-spacecraft studies of the auroral acceleration region: From cluster to nanosatellites. *Advances in Space Research*, 59(5):1173–1188, 2017. ISSN 18791948. . URL http://dx.doi.org/10.1016/j.asr.2016.11.037.

S. Sadeghi and M. R. Emami. Electric potential structures of auroral acceleration region border from multi-spacecraft Cluster data. *Advances in Space Research*, 61(8): 2050–2056, 2018. ISSN 18791948. . URL https://doi.org/10.1016/j.asr.2018.01.024.

Soheil Sadeghi and M. Reza Emami. Large-scale altitude distribution profile of auroral parallel electric potentials: A statistical analysis of Cluster data. *Advances in Space Research*, 64(2):378–384, 2019. ISSN 18791948. . URL https://doi.org/10.1016/j.asr.2019.03.043.

H. Sangha, S. E. Milan, J. A. Carter, A. R. Fogg, B. J. Anderson, H. Korth, and L. J. Paxton. Bifurcated Region 2 Field-Aligned Currents Associated With Substorms. *Journal of Geophysical Research: Space Physics*, 125(1), 2020. ISSN 21699402. .

R. Schreiber, M. Panchenko, J. Hanasz, R. Mutel, and I. Christopher. Beaming of intense AKR seen from the Interball-2 spacecraft. *Journal of Geophysical Research: Space Physics*, 122(1):249–257, 2017. ISSN 21699402. .

V. A. Sergeev, L. I. Vagina, R. D. Elphinstone, J. S. Murphree, D. J. Hearn, L. L. Cogger, and M. L. Johnson. Comparison of UV optical signatures with the substorm current wedge as predicted by an inversion algorithm. *Journal of Geophysical Research: Space Physics*, 101(A2):2615–2627, 1996. ISSN 0148-0227. .

J.-H. Shue, P. Song, C. T. Russell, J. T. Steinberg, J. K. Chao, G. Zastenker, O. L. Vaisberg, S. Kokubun, H. J. Singer, T. R. Detman, and H. Kawano. Magnetopause location under extreme solar wind conditions. *Journal of Geophysical Research: Space Physics*, 103(A8):17691–17700, 1998. ISSN 2169-9402. .

Yan Song and Robert L. Lysak. Displacement current and the generation of parallel electric fields. *Physical Review Letters*, 96(14):1–4, 2006. ISSN 00319007. .

Peter Stauning. The Polar Cap index: A critical review of methods and a new approach. *Journal of Geophysical Research: Space Physics*, 118(8):5021–5038, 2013. ISSN 21699402. .

M. Syrjäsuo, T. I. Pulkkinen, P. Janhunen, A. Viljanen, R. J. Pellinen, K. Kauristie, H. J. Opgenoorth, S. Wallman, P. Eglitis, P. Karlsson, O. Amm, E. Nielsen, and C. Thomas. Observations of Substorm Electrodynamics Using the MIRACLE Network. In S. Kokubun and Y. Kamide, editors, *Substorms-4*, volume 238 of *Astrophysics and Space Science Library*, page 111, January 1998. .

J. R. Taylor, M. Lester, and T. K. Yeoman. A superposed epoch analysis of geomagnetic storms. *Annales Geophysicae*, 12(7):612–624, jun 1994. ISSN 1432-0576. . URL https://angeo.copernicus.org/articles/12/612/1994/.

Rudolf A. Treumann. The electron-cyclotron maser for astrophysical application. *Astronomy and Astrophysics Review*, 13(4):229–315, 2006. ISSN 09354956. .

O. A. Troshichev and V. G. Andrezen. The relationship between interplanetary quantities and magnetic activity in the southern polar cap. *Planetary and Space Science*, 33(4):415–419, 1985. ISSN 00320633. .

G. R. Voots, D. A. Gurnett, and S. I. Akasofu. Auroral kilometric radiation as an indicator of auroral magnetic disturbances. *Journal of Geophysical Research*, 82(16): 2259–2266, jun 1977. ISSN 01480227. . URL http://doi.wiley.com/10.1029/JA082i016p02259.

Edward W Hones Jr. Magnetic Reconnection in the Earth's Magnetotail. *Australian Journal of Physics*, 38(6):981, 1985. ISSN 0004-9506. . URL http://www.publish.csiro.au/?paper=PH850981.

M. T. Walach and A. Grocott. SuperDARN Observations During Geomagnetic Storms, Geomagnetically Active Times, and Enhanced Solar Wind Driving. *Journal of Geophysical Research: Space Physics*, 124(7):5828–5847, 2019. ISSN 21699402. .

J. E. Waters, C. M. Jackman, L. Lamy, B. Cecconi, D. K. Whiter, X. Bonnin, K. Issautier, and A. R. Fogg. Empirical Selection of Auroral Kilometric Radiation During a Multipoint Remote Observation With Wind and Cassini. *Journal of Geophysical Research: Space Physics*, 126(10), oct 2021a. ISSN 2169-9380. . URL https://onlinelibrary.wiley.com/doi/10.1029/2021JA029425.

J E Waters, C M Jackman, D K Whiter, C Forsyth, A R Fogg, and L Lamy. A Perspective on Substorm Dynamics Using 10 Years of Auroral Kilometric Radiation Observations From Wind Journal of Geophysical Research : Space Physics. 2022. .

J.E. Waters, B. Cecconi, C.M. Jackman, D.K. Whiter, X. Bonnin, and L. Lamy. Wind/waves flux density collection calibrated for auroral kilometric radiation (version 1.0) [data set]. *PADC*, 2021b. .

D. R. Weimer, J. D. Craven, L. A. Frank, W. B. Hanson, N. C. Maynard, R. A. Hoffman, and J. A. Slavin. Satellite measurements through the center of a substorm surge. *Journal of Geophysical Research: Space Physics*, 99(12):23639–23649, 1994. ISSN 21699402. .

D. K. Whiter, B. Gustavsson, N. Partamies, and L. Sangalli. A new automatic method for estimating the peak auroral emission height from all-sky camera images. *Geoscientific Instrumentation, Methods and Data Systems*, 2(1):131–144, 2013. ISSN 21930864. .

World Data Center for Geomagnetism Kyoto, M. Nose, T. Iyemori, M. Sugiura, and T. Kamei. Geomagnetic AE index, 2015. URL https://doi.org/10.17593/15031-54800.

C. S. Wu and L. C. Lee. A theory of the terrestrial kilometric radiation. *The Astrophysical Journal*, 230:621, 1979. ISSN 0004-637X. . URL http://adsabs.harvard.edu/doi/10.1086/157120.

C.S. Wu. Kinetic cyclotron and synchrotron maser instabilities: Radio emission processes by direct amplification of radiation. *Space Science Reviews*, 41(3-4):215–298, aug 1985. ISSN 0038-6308. . URL http://link.springer.com/10.1007/BF00190653.

D. J. Wu, J. K. Chao, and R. P. Lepping. Interaction between an interplanetary magnetic cloud and the Earth's magnetosphere: Motions of the bow shock. *Journal of Geophysical Research: Space Physics*, 105(A6):12627–12638, jun 2000. ISSN 01480227. . URL http://doi.wiley.com/10.1029/1999JA000265.

Fuliang Xiao, Lunjin Chen, Huinan Zheng, and Shui Wang. A parametric ray tracing study of superluminous auroral kilometric radiation wave modes. *Journal of Geophysical Research: Space Physics*, 112(10):1–10, 2007. ISSN 21699402. .

Fuliang Xiao, Qinghua Zhou, Zhenpeng Su, Zhaoguo He, Chang Yang, Si Liu, Yihua He, and Zhonglei Gao. Explaining occurrences of auroral kilometric radiation in Van Allen radiation belts. *Geophysical Research Letters*, 43(23):11,971–11,978, 2016. ISSN 19448007. .

K. H. Yearby and J. S. Pickett. A Review of Cluster Wideband Data Multi-Spacecraft Observations of Auroral Kilometric Radiation. *Journal of Geophysical Research: Space Physics*, 127(2), feb 2022. ISSN 2169-9380. . URL https://onlinelibrary.wiley.com/doi/10.1029/2021JA029499.

P. Zarka, B. Cecconi, and W. S. Kurth. Jupiter's low-frequency radio spectrum from Cassini/Radio and Plasma Wave Science (RPWS) absolute flux density measurements. *Journal of Geophysical Research: Space Physics*, 109(A9):1–18, 2004.

A. Zaslavsky, N. Meyer-Vernet, S. Hoang, M. Maksimovic, and S. D. Bale. On the antenna calibration of space radio instruments using the galactic background: General formulas and application to STEREO/WAVES. *Radio Science*, 46(2):1–7, 2011. ISSN 00486604. .

Wanli Zhao, Si Liu, Sai Zhang, Qinghua Zhou, Chang Yang, Yihua He, Zhonglei Gao, and Fuliang Xiao. Global Occurrences of Auroral Kilometric Radiation Related to Suprathermal Electrons in Radiation Belts. *Geophysical Research Letters*, 2:7230–7236, 2019. ISSN 19448007. .

Thomas H. Zurbuchen and Ian G. Richardson. In-situ solar wind and magnetic field signatures of interplanetary coronal mass ejections. *Space Science Reviews*, 123(1-3): 31–43, 2006. ISSN 00386308. .